# ABSTRACT


| | |
|---|---|
| Title of Dissertation: | MOLECULAR SIMULATION AND SPECTROSCOPY OF A STRONG MULTIPOLAR FLUID |
| | Samuel R. Cohen<br>Doctor of Philosophy, 2021 |
| Dissertation directed by: | Professor John T. Fourkas, Department of Chemistry and Biochemistry |



Acetonitrile ($CH_3CN$) is a small, aprotic molecule. The apparent simplicity of this species belies great complexity in its organization and dynamics in the liquid state. Additionally, at silica surfaces, liquid acetonitrile takes on a lipid-bilayer-like structure that has great practical importance in batteries, chromatography, and heterogeneous catalysis. In this thesis, I use molecular simulations and neutron scattering to explore the structure and dynamics of liquid acetonitrile in the bulk and at silica interfaces.

First, using angularly resolved radial distribution functions, I identify a microscopic structure in bulk acetonitrile in which most liquid molecules form antiparallel and/or head-to-tail dimers. In contrast to the traditional view of acetonitrile, antiparallel dimers are shown to be octupole-paired, as opposed to dipole-paired. Further analysis reveals that head-to-tail dimers are the dominant motif and live longer

than antiparallel dimers. I also use angularly resolved radial distribution functions to show that this propensity to form head-to-dimers has signatures in the observed crystalline polymorphs, and I connect my results using molecular simulation to neutron-scattering data that I also collected.

Second, I present findings on the structure and transport properties of acetonitrile at the liquid/silica interface. I use molecular simulations to show that the bilayer is exceptionally robust with large changes in temperature. The effects of Poiseuille hydrodynamic flow on the surface bilayer suggest where the flow boundary may lie, because there is a departure in the vicinity of the walls from the standard parabolic fit describing Poiseuille flow. These results will help guide ion-separation and ion-current experiments using acetonitrile as a solvent.

In a separate set of chapters, I present a data analysis protocol for the characterization of absorptive linearities and nonlinearities measured using 2-beam action spectroscopy. This nonlinear-optical technique, along with the protocol described in this thesis, enables the simultaneous determination of the effective order(s) of absorption. This method is important in the study of many nonlinear-optical phenomena, including multiphoton absorption polymerization.

# MOLECULAR SIMULATION AND SPECTROSCOPY OF A STRONG MULTIPOLAR FLUID

by

Samuel R. Cohen

Dissertation submitted to the Faculty of the Graduate School of the
University of Maryland, College Park, in partial fulfillment
of the requirements for the degree of
Doctor of Philosophy
2021

Advisory Committee:
Professor John T. Fourkas, Chair
Professor Millard H. Alexander
Dr. Benoit Coasne
Professor Amy S. Mullin
Professor John D. Weeks
Professor Jeffery B. Klauda

# Dedication

To Audrey, *shirinam*

# Acknowledgements

It is ironic that I ended up primarily doing simulations for my thesis because I struggled mightily at the start of graduate school with the choice of doing experiments or theory. Now, I realize that small-molecule liquids represent enormously interesting and useful candidates for both molecular simulations and scattering experiments, as I aim to show in my thesis.

I thank my advisors, Prof. John Fourkas and Dr. Benoit Coasne, for the opportunity to work on molecular simulations and neutron scattering, especially during my experience as a Chateaubriand Fellow in Grenoble, France. My time abroad was difficult, but I appreciate my advisors' deep knowledge of how to correlate spectroscopic results with simulations in a useful way. When the results of my initial project did not turn out as expected, several times, we found an interesting way forward each time, until my project gradually took a new shape. I feel like training a graduate student is like taming a wild animal to do something useful. The student must undergo a major change, akin to a phase transition, so that he or she may become a true scientist. I thank both of my bosses for challenging me to grow into becoming a true scientist: in particular, Benoit for sharing his expertise in molecular simulation and for inviting me to Grenoble, and John for his insight in teasing out the novelty of my findings and for his yeoman's work in helping me to finish my thesis.

Many other people contributed to the work described in my thesis, and their collaboration has greatly enhanced my research. When I was abroad, I worked with Dr. Marie Plazanet, whom I thank for her help with neutron experiments during the long hours and late nights in Grenoble and Oxford and the subsequent analysis of the data.

I also thank Dr. John Bender, Sandra Gutierrez Razo, Dr. Nikos Liaros, and Dr. Amanda Souna for their help at the University of Maryland on experiments that relate to some of the work described here. I thank Dan Jovinelli for being a sounding board on nonlinear optical spectroscopy.

It is a pleasure to thank Profs. Millard Alexander, Jeffery Klauda, Amy Mullin, and John Weeks for their time serving on my thesis committee – and Prof. Zhihong Nie for his time serving on my candidacy committee. I appreciate that my PhD quartet has patiently tolerated my repeated rescheduling of my defense. I also thank Profs. Alexander, Mullin, Nie, and Weeks for teaching me in courses that I enjoyed, and I especially thank Prof. Weeks for being so generous with his time and advice. I am disappointed not to defend my thesis in person to thank him and all of the other members of my committee.

Now comes my favorite part. Without many supportive friends and family members, I would not have made it through the crucible of graduate school.

Among my friends, I thank, in particular, Onur Kara for his constant encouragement and our many spirited discussions about life and science over the years. We were once naïve "Hilbert space cadets" taking quantum mechanics together. Onur, you constantly amaze me with your clever ways of looking at things sideways and afresh. You have a kind heart, too. You're my brother. I thank Dr. Teddy Baker for sharing with me his enthusiasm for physics and esoteric math. Teddy, I can't wait to read about the Riemann-Baker "Conjecture." Deign to remember me when you're famous. I thank Dr. Aravind Chandrasekaran for his camaraderie and his sensible and kind nature that I should try harder to emulate. Aravind, you're the most grounded

person I know, and you're also a great scientist. Onur, Teddy, and Aravind – you've all helped me to become a better scientist and person.

I thank my former Wisconsin bosses – Prof. Jörg Woehl, Prof. Jeff Wesson, Prof. Neil Mandel, and Ann Kolbach-Mandel – for their continued mentorship. I like rhapsodizing about science with you guys.

I thank my former teachers, Profs. Marc Pelen (deceased) and Roy Rosenstein, for their genuine kindness and encouragement. Roy, *magister ludi*, you've helped me to find my niche at last. I learned so much from you as a teenager and now *nel mezzo del cammin*. Marc (can I now call him that?) was my guru. I miss him.

I thank Dr. Cécile Goujet-Zalc and Prof. Daniel Goujet for their kindness during my stay in France and for showing me that it is truly possible to achieve work-life balance. You're like my second parents. I also thank Sepi and Jay Degges for being like my second Goujets.

Thank you to my doctors, who I will not name out of discretion, but who were nonetheless instrumental in making sure I stayed healthy enough to finish my program.

Finally, I thank my family – Mom, Dad, Alex, Madeleine, and especially my wife, Audrey – for their enduring love and support. My parents have patiently helped me through my many travails. "There are never enough I love you's." Alex, my brother, my twin, thank you for always looking out for me. My sister cheered me up when I was at my nadir. Madeleine, your PhD awaits. Audrey, my beloved, getting to know you has been the highlight of my life. If the world went away, and there was no more science, no more anything, but there was still the two of us, then that would be enough.

# Table of Contents

# List of Tables

# List of Figures

**Figure 4.1** (A) Schematic depiction of two-beam action spectroscopy. Two temporally interleaved pulse trains with average powers $\bar{P}_1$ and $\bar{P}_2$ are incident on a sample, generating an observable via linear and/or nonlinear absorption. (B) Sets of values of $\bar{P}_1$ and $\bar{P}_2$ that lead to the same value of the observable are determined, and $\bar{P}_2$ is plotted as a function of $\bar{P}_1$ to determine the order(s) of absorption. The dashed lines denote $\bar{P}_{\text{diag}}$. $\theta$ is the angle that a line from the origin to a data point makes with the $x$ axis.

**Figure 4.2** Plots of the logarithmic plot exponent $n$ as a function of the 2-BA exponent $m$ for six different ($j$,$k$): (A) sets for $j$ = 1; (B) sets for $j$ = 2; (C) the set for $j$ = 3. The symbols indicate the points at which $n = m$, which occurs when only a single absorption process is present.

**Figure 4.3** Difference between Eq. (4.5) and Eq. (4.1) with $m$ determined along the diagonal for a combination of linear and quadratic components as a function of the amplitude of the linear component, $a$. The panels show results for $a$ values in the ranges (A) 0.1 to 0.9, (B) -0.1 to -0.9, and (C) 1.1 to 1.9.

**Figure 4.4** The difference between Eq. (4.5) and Eq. (4.1) with $m$ determined along the diagonal for (1,3) as a function of the amplitude of the linear component, $a$. The panels show results for $a$ values ranging from (A) 0.1 to 0.9; (B) -0.1 to -0.9; and (C) 1.1 to 1.5.

**Figure 4.5** The difference between Eq. (4.5) and Eq. (4.1) with $m$ determined along the diagonal for (1,4) as a function of the amplitude of the linear component, $a$. The panels show results for $a$ values ranging from (A) 0.1 to 0.9; (B) -0.1 to -0.9; and (C) 1.1 to 1.25.

**Figure 4.6** The difference between Eq. (4.5) and Eq. (4.1) with $m$ determined along the diagonal for (2,3) as a function of the amplitude of the quadratic component, $a$. The panels show results for $a$ values ranging from (A) 0.1 to 0.9; (B) -0.1 to -0.9; and (C) 1.1 to 1.25.

**Figure 4.7** The difference between Eq. (4.5) and Eq. (4.1) with $m$ determined along the diagonal for (2,4) as a function of the amplitude of the quadratic component, $a$. The panels show results for $a$ values ranging from (A) 0.1 to 0.9; (B) -0.1 to -0.9; and (C) 1.1 to 1.25.

**Figure 4.8** The difference between Eq. (4.5) and Eq. (4.1) with $m$ determined along the diagonal for (3,4) as a function of the amplitude of the cubic component, $a$. The panels show results for $a$ values ranging from (A) 0.1 to 0.9; (B) -0.1 to -0.9; and (C) 1.1 to 1.25.

**Figure 4.9** Difference between Eq. (4.5) and Eq. (4.1) for $m$ = 2.5 for each of the different ($j$,$k$) examined.

**Figure 4.10** Plots of Eq. (4.6) using different ($j$,$k$) for data generated using (1,2) and $m$ = 2.1. The data points are color-coded on the basis of their angles $\theta$ relative to the $x$ axis in a 2-BA plot (see the legend). $\varphi$ is the angle a line from the origin to a data point makes with the $x$ axis.

**Figure 4.11** Plots of Eq. (4.6) using different ($j$,$k$) for data generated using (1,3) and $m$ = 2.1. The data points are color-coded on the basis of their angles $\theta$ relative to the $x$ axis in a 2-BA plot (see the legend).

**Figure 4.12** Plots of Eq. (4.6) using different ($j$,$k$) for data generated using (2,3) and $m$ = 2.1. The data points are color-coded on the basis of their angles $\theta$ relative to the $x$ axis in a 2-BA plot (see the legend).

**Figure 4.13** Plots of Eq. (4.6) using different ($j$,$k$) for data generated using (1,4) and $m$ = 2.1. The data points are color-coded on the basis of their angles $\theta$ relative to the $x$ axis in a 2-BA plot (see the legend).

**Figure 4.14** Plots of Eq. (4.6) using different ($j$,$k$) for data generated using (2,4) and $m$ = 2.1. The data points are color-coded on the basis of their angles $\theta$ relative to the $x$ axis in a 2-BA plot (see the legend).

**Figure 4.15** Plots of Eq. (4.6) using different ($j$,$k$) for data generated using (3,4) and $m$ = 2.1. The data points are color-coded on the basis of their angles $\theta$ relative to the $x$ axis in a 2-BA plot (see the legend).

**Figure 4.16** Angle that plots of Eq. (4.6) make with the $x$ axis ($\varphi$) as a function of the 2-BA plot angle $\theta$ for $m$ = 2.1 and different ($j$,$k$) using the data in (A) Figure 4.10, (B) Figure 4.11, and (C) Figure 4.12.

**Figure 4.17** Angle that plots of Eq. (4.6) make with the $x$ axis ($\varphi$) as a function of the 2-BA plot angle $\theta$ for $m$ = 2.1 and different ($j$,$k$) using the data in (A) Figure 4.13, (B) Figure 4.14, and (C) Figure 4.15.

**Figure 5.1** (A) An acetonitrile molecule, showing the label and partial charge for each atom type. Representative molecular configuration at $T$ = 298 K for (B) bulk liquid acetonitrile; the red frame indicates the molecular simulation box used in the calculations.

**Figure 5.2** Static structure factor $S(q)$ for bulk ACN at 298 K as obtained from molecular simulations (black) and neutron-diffraction experiments[9,10] (red), where $q$ is the magnitude of the scattering wave vector. The three sets of data are for different isotopologues, with deuterium/hydrogen and/or $^{14}N/^{15}N$ isotopic substitutions. The $S(q)$ for the three different isotopologues are offset vertically for clarity.

**Figure 5.3** Simulated radial distribution function $g(r)$ between different acetonitrile atom types and for the molecular center of mass (COM) in the bulk liquid at 298 K. In both panels, some of the functions are offset vertically for clarity.

**Figure 5.4** The center-of mass $g(r,\theta)$ and $g(r)$ for acetonitrile, along with representative configurations from the indicated regions.

**Figure 5.5** Comparison of $g_{CT\text{-}CT}(r,\cos\theta)$ calculated (A) from a molecular dynamics simulation (this work) using the force field of Nikitin and Lyubartsev[68] and (B) by the reverse Monte Carlo method[29] using the OPLS-AA[90] force field as a constraint. In each case the corresponding $g(r)$ is shown for comparison. The data in panel (B) for both $g_{CT\text{-}CT}(r)$ and the unnormalized $g_{CT\text{-}CT}(r,\cos\theta)$ were provided by one of the authors (S. Pothoczki) of the reverse Monte Carlo study. In (A) the bin size is 0.1 Å in $r$ and 0.05 in $\cos\theta$. In (B) the bin size is 0.1 Å in $r$ and 0.10 in $\cos\theta$. The difference in bin sizes in $\theta$ is responsible for the different $z$ scaling of the two heat maps.

**Figure 5.6** Angularly resolved radial distribution functions calculated with respect to the center-of-mass separation. Panel (A) shows $g(r,\theta)$ and panel (B) shows $g(r,\cos\theta)$. Note that in (B) the $\cos\theta$ axis goes from 1 to -1 for ease of comparison. The corresponding $g(r)$ is shown next to each heat map. These two plots indicate that the two different representations highlight different features of the orientational distribution. The bin size in $r$ is 0.1 Å in each plot. The bin size in $\theta$ is 4° and the bin size in $\cos\theta$ is 0.05.

**Figure 5.7** Integral of normalized $g(r,\theta)$ and $g(r,\cos\theta)$ with respect to $\theta$ and with respect to $\cos\theta$, respectively, at a center of mass-center of mass distance of $r$ = 3.85 Å. The integrals extend from 180° to $\cos^{-1}(\cos\theta)$ and -1 to $\cos\theta$, respectively. The close correspondence between the two plots indicates that the heat maps in Fig. 5.5 display the same data, despite their different appearances.

**Figure 5.8** Radial distribution functions and angularly resolved radial distribution functions for acetonitrile with respect to the methyl-methyl distance, the methyl-cyano distance, and the cyano-cyano distance for different molecules, with the angle $\theta$ defined as described in the text, along with representative configurations from the indicated regions.

**Figure 5.9** Histograms comparing the probability distributions for neighbors that are (A) antiparallel and (B) head-to-tail for different sets of criteria. In both cases, the qualitative characteristics of the distributions are not highly sensitive to the selection criteria.

**Figure 5.10** Analysis of head-to-tail dimers, with the angle $\alpha$ defined by the unit vector along the principal molecular axis of a molecule 1 with the unit vector between the methyl group of the molecule 1 and the cyano group of a molecule 2. The directions of

the unit vectors are illustrated schematically in the figure. The probabilities $P(r)$ and $P'(\alpha)$ are defined as described in the text.

**Figure 5.11** Radial distribution functions and angularly resolved radial distribution functions for crystalline acetonitrile with respect to the methyl-cyano distance for the $\alpha$ polymorph (top left) and the $\beta$ polymorph (top right) as well as with respect to the cyano-cyano distance for the $\alpha$ polymorph (bottom left) and for the $\beta$ polymorph (bottom right).

**Figure 5.12** Radial distribution functions and angularly resolved radial distribution functions for crystalline acetonitrile with respect to the center-of-mass distance for the $\alpha$ polymorph (top left) and the $\beta$ polymorph (top right) as well as with respect to the cyano-cyano distance for the $\alpha$ polymorph (bottom left) and for the $\beta$ polymorph (top right).

**Figure 5.13** Probability that an acetonitrile molecule is associated with antiparallel (AP) or head-to-tail (HT) neighbors, as defined in the text.

**Figure 5.14** Mean-squared displacement as a function of time for each atomic site. The line indicates the Fickian limit, in which the MSD is given by $6Dt$.

**Figure 5.15** Acetonitrile velocity autocorrelation functions for (A) HC, (B) CT, (C) YC, (D) YN, and (E) the center of mass.

**Figure 5.16** (A) Low-frequency region of the simulated generalized density of states for ACN, along with an overlay of the experimental, height-normalized inelastic neutron spectra for ACN and ACN-$d_3$. (B) Full spectra of the simulated vibrational density of states for ACN calculated with respect to the molecule center of mass (COM, top spectrum) and for each atomic site on the molecule. The densities of states are offset vertically for clarity.

**Figure 5.17** Mean first passage times for molecules in pairs, calculated following the methodology of Impey *et al.*[101] The solid lines correspond to antiparallel pairs and the dashed lines correspond to head-to-tail pairs. The curves are color-coded by the tolerance time $\tau^*$; note that results are only shown for head-to-tail pairs out to $\tau^* = 1$ ps.

**Figure 5.18** Spectrum for the aluminum that was used as the cell for the inelastic neutron-scattering experiments. The intensity of the spectra for ACN and ACN-$d_3$ is affected by imperfect subtraction of the features in the aluminum data between 150 and 300 $cm^{-1}$.

**Figure 5.19** $S(q,\omega)$ as a function of energy transfer $\omega$ for ACN obtained from (A) molecular dynamics simulations and (B) quasielastic neutron scattering. The legends indicate the different values of $q$ that were used. The quasielastic neutron scattering experiments were performed on LET (at ISIS, UK) with an incident energy $E_{we} = 2.83$ meV.

**Figure 5.20** (A) The QENS data from Figure 5.19(B) were analyzed with a sum of two Lorentzian contributions whose full-widths at half maximum (FWHMs) are shown on panels (A) and (B). (A) FWHM of the translational contribution, with the values for $D_s$(ACN) and $D_s$(ACN-$d_3$) as in Table 5.1. The data for ACN-$d_3$ exhibit de Gennes narrowing at $q \sim 1.6$ Å$^{-1}$, which is at the maximum of the structure factor $S(q)$ (also shown for comparison). The fit is to the data for ACN. (B) The larger contribution is characteristic of a fast transition fitted with a jump-diffusion model, and is assigned to the coupling between translation and the rotation of the methyl groups.

**Figure 6.1** (A) Representative molecular configuration at $T$ = 298 K for the liquid/vapor interface. (B) Top view of the hydroxylated silica substrate used in this work, showing the label and partial charge for the silanol atom types. Representative molecular configurations at $T$ = 298 K for (C) the liquid/silica interface and (D) a slit-pore. For each representative configuration, the red frames indicate the molecular simulation box used in the calculations.

**Figure 6.2** Data from simulations in the isothermal/isobaric ensemble used to calculate the saturating vapor pressure. The linear fit is constrained to go through the origin. The error bars represent the 95% confidence levels.

**Figure 6.3** (A) Normal pressure, (B) tangential pressure, and (C) surface tension for the gas/liquid interface with $L_z$ = 108 Å.

**Figure 6.4** Radial distribution functions and angularly resolved radial distribution functions for acetonitrile with respect to the methyl-methyl distance, with the angle $\theta$ defined as described in Chapter 5. The difference map between the angularly resolved radial distribution functions at the interface and the bulk is also given, along with representative configurations from the indicated regions.

**Figure 6.5** Methyl-carbon density $\rho(z)$ of ACN as a function of distance from the interface, normalized to the corresponding bulk density $\rho^B(T)$ for each temperature.

**Figure 6.6** Nitrogen density $\rho(z)$ of ACN as a function of distance from the interface for each temperature.

**Figure 6.7** Center-of-mass density $\rho(z)$ of ACN as a function of distance from the interface, normalized to the corresponding bulk density $\rho^B(T)$ for each temperature.

**Figure 6.8** Center-of-mass density $\rho(z)$ of ACN as a function of distance from the interface for each temperature.

**Figure 6.9** Average orientation of ACN for each temperature as a function of the center-of-mass distance from the surface normal $\hat{\mathbf{z}}$. A $\cos\theta$ value of 0 indicates that the cyano groups tend to point toward the silica.

# List of Abbreviations

| | |
|---|---|
| 2-BIT | 2-beam initiation threshold |
| 2-BA | Two-beam action (also referred to as 2-beam action) |
| 2-BCAmP | 2-beam constant-amplitude photocurrent |
| ACN | Acetonitrile |
| AP | Antiparallel |
| COM | Center of mass |
| CW | Continuous-wave |
| CN | Cyano |
| DOS | Density of states |
| ESA | Excited-state absorption |
| GDOS | Generalized density of states |
| GCMC | Grand Canonical Monte Carlo |
| HT | Head-to-tail |
| LAMP | Large-Array Manipulation Program |
| LJ | Lennard-Jones |
| MD | Molecular dynamics |
| Me | Methyl |
| ML | Mode-locked |
| MPA | Multiphoton absorption |
| MSD | Mean-squared displacement |
| NEMD | Nonequilibrium molecular dynamics |
| NLA | Nonlinear absorption |

| | |
|---|---|
| NPT | Isothermal/isobaric |
| NVE | Microcanonical |
| NVT | Canonical |
| OKE | Optical Kerr effect |
| PE | Photocurrent excitation |
| QENS | Quasielastic neutron scattering |
| RISM | Reference interaction-site model |

# Chapter 1: Introduction

## 1.1 *Background*

### 1.1.1. Small-Molecule Liquids

Most laboratory chemistry occurs in solution, and liquid water is the universal medium for all known life. Despite the importance of liquids, this state of matter is still poorly understood. Textbooks on physical chemistry[1-3] cover subjects such as solution chemistry and the thermodynamics of mixtures, but rarely introduce liquids as a fundamental topic. Most textbooks do not mention, with the possible exception of water, the structure or other essential features known to exist in all liquids. This void in the didactic treatment of liquids might reflect the state of research; such a view of liquids is summarized in the 1958 edition of the textbook by Landau and Lifshitz on statistical physics:[4]

> Unlike solids and gases, liquids do not allow a general calculation of their thermodynamic quantities or even their temperature dependence. The reason for this is the presence of strong interactions between the molecules of the liquid without having at the same time the smallness of vibrations which makes the thermal motion of solids so simple. The high intensity of the molecular interaction makes it important to know, when calculating thermodynamic quantities, the actual law of interaction, which varies for different liquids. The only thing which can be done in general form is the study of the properties of liquids near absolute zero.

From the point of view of physical chemistry, one of the beguiling aspects of liquids is that they are strongly interacting, disordered, many-body systems, as the above quote indicates. The comparison to gases and solids is instructive. In contrast to gases,

intermolecular interactions are prominent in liquids, and collisions between molecules in a liquid are not so sharp or well-defined. In contrast to solids, liquids exhibit complicated dynamics: they flow, and collisions are common. These features, which make liquids interesting, also make liquids difficult to understand. It is telling, however, that the statement by Landau and Lifshitz cannot be found in more recent editions of their textbook [e.g., Ref. 5]. The subsequent advent of neutron scattering experiments, nonlinear optical spectroscopies, and molecular simulation, along with parallel developments in theory, have all improved the understanding of liquids.

One area of intense research in liquids is the molecular organization, intermolecular interactions, and dynamics that occur in liquids confined in single-digit nanopores[6] or, in a simpler realization, at a liquid/solid interface. By combining molecular simulation and experiment, we can develop a better understanding of these systems. In addition to being fundamentally interesting to study, these systems are of great practical importance in separations, catalysis, nanofluidics, waste remediation, and energy storage, among other applications.

Here we study liquid acetonitrile, an interesting model system. Acetonitrile ($CH_3CN$) is a common organic solvent that also is important as a representative strong dipolar fluid and the simplest alkyl cyanide. A single acetonitrile molecule (Figure 1.1) has a large dipole moment of 3.92 D.[7] The molecule is composed of dipolar ($-C\equiv N$) and weakly dipolar ($-CH_3$) moieties. The molecule has high symmetry and a linear core. Its relatively simple molecular structure belies great complexity in the liquid state. For many decades, acetonitrile has been known experimentally[8-11] to form antiparallel dimers in the bulk liquid (i.e., in the pure liquid without any interfaces). The traditional

view is that neighboring molecules have a tendency to form so-called dipole-pairs with respect to the antiparallel alignment of neighboring cyano groups. Molecular simulations have shown the additional presence of head-to-tail dimers[12] that presumably form due to electrostatic attractions. Together, these results suggest a complicated intermolecular structure.

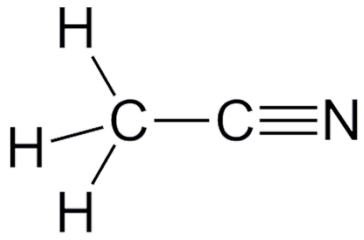


**Figure 1.1** Structure of the acetonitrile molecule.

Molecular simulation, in which classical (Newtonian) physics is used to simulate the behavior of a system of interacting particles, gives an atomic, time-resolved picture of the organization of a liquid. This picture can help us to glean new information about the structure and dynamics of liquid acetonitrile. Even the liquid structure for a molecule that is as well-studied and simple as acetonitrile is not fully known, due in part to the irretrievable loss of angular information associated with diffraction experiments on liquids. How a dense liquid fills three-dimensional space is not a simple problem; in mathematical physics, such packing problems date back centuries to Kepler, and remain unsolved.[13] Because representing the structure of a molecular liquid is not trivial, there remain important questions about how the structure of liquid acetonitrile affects its dynamics. In Chapter 5, I describe a study of bulk liquid acetonitrile that combines both molecular simulation and neutron scattering.

The behavior of liquid acetonitrile at interfaces is considerably different than in the bulk liquid. Hard interfaces have so far been studied because they are relatively

simple. At hydroxylated silica interfaces, acetonitrile is known to adopt an interdigitated, bilayer-like organization that resembles supported biological structures such as phospholipid bilayers.[14] Near the silica, the cyano groups accept hydrogen bonds from the surface silanol (−SiOH) groups to form a sublayer with the acetonitrile molecules aligning perpendicularly to the surface. A second sublayer of acetonitrile molecules has its methyl groups directed toward the methyl groups of the first sublayer. Such tail-to-tail interactions are not common in the bulk liquid. This second sublayer has a broader orientational distribution than the first, and the two sublayers are interdigitated with respect to one another.

There have been many experiments that agree with this bilayer picture. The first study on this topic was an NMR study on liquid acetonitrile confined in nanoporous sol-gel glasses, which found that tighter confinement corresponds to slower overall dynamics.[15] These data were interpreted using a two-state model that associated a surface population with fast spin-lattice relaxational dynamics, and a bulk-like population with a slower spin-lattice relaxation time corresponding to that of the bulk liquid.[15] In agreement with the NMR study, experiments using optical Kerr effect (OKE) spectroscopy on acetonitrile confined in sol-gels found that collective orientational times also depend on the pore size.[16-18] The confined data were fit to the sum of three exponentials, with a short decay time associated with the reorientation of the bulk-like component, a long decay time associated with the reorientation of the surface component, and an intermediate decay time associated with the exchange of molecules between the two populations.[16,17] Arrhenius plots for the NMR and OKE surface relaxation times give a larger value of the static orientational correlation

parameter $g_2$ for the confined liquid than for the bulk liquid, suggesting that there is significantly increased parallel ordering in the pore surfaces.[16] Modifying the surface chemistry gives further evidence in support of the bilayer structure. In rendering the pore surfaces hydrophobic through silanization, the OKE decays become biexponential,[16] in agreement with other OKE studies of confined liquids without specific surface interactions.[18] These data suggest that the exchangeable population consists of molecules that are interdigitated among the nonexchangeable population. The latter population tends to be more ordered along the surface normal and accepts hydrogen bonds from the silanol groups of the silica.

These experimental findings have been verified extensively by molecular simulations.[19-23] Simulations of acetonitrile at the liquid/silica interface reveal an interdigitated surface structure.[21,22] The structure resembles a supported lipid bilayer rather than being driven by dipole-pairing. There is no sign of this structuring in the bulk liquid, and signs of the structure at flat surfaces propagate for at least four layers (~20 Å) into the bulk-like liquid.[21,22] A similar structure has been observed in simulations of acetonitrile confined in cylindrical pores[19,20] and slit-geometries.[23] These simulations confirm the existence of two populations: a nonexchangeable, surface population and an exchangeable, bulk-like population.[20] Molecular simulations can also help answer experimentally-motivated questions about the stability of the bilayer with respect to temperature and the transport properties of confined acetonitrile.

In Chapter 6, I discuss my results of molecular simulations showing the persistence of the bilayer with temperature. This finding suggests that temperature can be used as a variable for ion-selective separations involving acetonitrile. I also present

our preliminary results to study Poiseuille hydrodynamic flow in molecular simulations of confined acetonitrile. I discuss the implications for future ion current experiments on these systems before concluding with proposals for future research.

### 1.1.2. Nonlinear Optical Spectroscopy

Nonlinear optics refers to the nonlinear dependence of the polarization density on the electric field of light. Some nonlinear optical techniques can give valuable insights into liquid dynamics, but the nonlinear optical methods presented in Chapters 3 and 4 involve multiphoton absorption (MPA). MPA is a nonlinear-optical effect that has been studied extensively over the years. MPA occurs when an atomic or molecular system is excited by the simultaneous absorption of two or more photons. Characterizing MPA is especially important for many nonlinear systems, including those materials that are used in fluorescence imaging[24-26] and micro- and nanofabrication,[27] among other technologies. Many experimental techniques have been developed to characterize such nonlinear processes by determining their order and magnitude.[28] Most research has focused on characterizing two-photon absorption, as it is not only the conceptually simplest case of MPA, but also is a suitable means to excite many organic materials that absorb in the ultraviolet region of the electromagnetic spectrum. Nonlinear absorption can, however, involve more than two photons,[29-31] and when there are excited-state absorption processes, the order can be considered to be effective rather than truly instantaneous.[32]

There are both direct and indirect methods for determining the effective order(s) of absorption in a material.[28] Direct methods measure the intensity of light that is

absorbed by the material. Because these methods require high laser irradiance to induce a measurable nonlinear signal, they can cause additional phenomena to occur that complicate the analysis. In contrast, indirect methods use a secondary observable that depends on the MPA cross section. In Chapters 3 and 4, I discuss the development of two-beam action spectroscopies, a class of indirect methods that rely on using two interleaved, ultrafast pulse trains to generate an observable in the irradiated material by linear and/or nonlinear absorption. I focus primarily on the development of a data analysis protocol for these spectroscopies that makes it possible to determine two different contributions that can contribute to the observable.

## 1.2 *Outline*

The work described in this thesis has two parts. The first is data analysis for two-beam action (2-BA) spectroscopies, which are a class of optical techniques for determining the order(s) of absorption, as described above. The second is an analysis of liquid acetonitrile in the bulk, at interfaces, and in slit-pore geometries to develop insights into the structure and dynamics of this liquid for applications such as separations and nanofluidics.

The outline of this thesis is as follows:

- Chapter 2: The principles of molecular simulation and neutron scattering used in this thesis are described. Basic statistical mechanics and the extraction of the density of states from inelastic neutron scattering data are discussed.
- Chapter 3: 2-beam constant-amplitude photocurrent spectroscopy is used to study linear and nonlinear absorption by a GaAsP photodiode. A framework is

presented for using non-integral 2-BA exponents to determine the relative contributions of two absorption mechanisms of different order. The dependence of the ratio of the quadratic and linear contributions on the average excitation power is used to verify that these are the dominant orders of absorption in the photodiode with 800 nm excitation.

- Chapter 4: Here we develop a theoretical comparison between conventional methods that determine the order(s) of absorption using logarithmic plots and 2-BA-based techniques. We also explore how 2-BA plots arising from two orders of absorption deviate from a plot with a single, non-integer exponent. We demonstrate that these deviations can usually be used to identify the two orders of absorption and their relative contributions to the signal on the basis of measurements made at a single value of the observable.
- Chapter 5: We examine the interplay between organization and dynamics in bulk liquid acetonitrile. Using angularly resolved radial distribution functions, $g(r,\theta)$, derived from molecular simulations, we identify a microscopic structure in which most liquid molecules are associated with one or more neighboring molecules in octupole-paired, antiparallel and/or offset, head-to-tail configurations. An analysis of these structural motifs reveals that head-to-tail dimers are more prevalent and live longer than antiparallel dimers. Finally, using both neutron scattering techniques and molecular simulations, we study the dynamics in liquid acetonitrile over time scales ranging from subpicosecond (the vibrational density of states) to picosecond (rotational/translational

motions and the generalized density of states) to tens of picoseconds (self-diffusivity in the Fickian regime).

- Chapter 6: The temperature dependence of the acetonitrile bilayer at a flat silica interface is investigated using molecular simulations. The bilayer is shown to be stable across a wide range of temperatures. Results from nonequilibrium molecular dynamics simulations of confined acetonitrile are also presented, showing the departure from Poiseuille hydrodynamics flow for the molecules at the interface.
- Chapter 7: Conclusions and future work.

## 1.3 *References*


1. McQuarrie, D. A.; Simon, J. D. *Physical Chemistry: A Molecular Approach*; University Science Books: Sausalito, 1997.
2. Atkins, P.; de Paula, J.; Keeler, J. *Atkins' Physical Chemistry*, 11th ed.; Oxford University Press: Oxford, 2018.
3. Silbey, R. J.; Alberty, R. A.; Bawendi, M. G. *Physical Chemistry*, 4th ed.; Wiley: New York, 2005.
4. Landau, L. D.; Lifshitz, E. M. *Course of Theoretical Physics 5: Statistical Physics*, transl. by E. Peierls and R. F. Peierls; Pergamon Press: Oxford, 1958.
5. Landau, L. D.; Lifshitz, E. M. *Course of Theoretical Physics 5: Statistical Physics*, 3rd ed., transl. by J. B. Sykes and M. J. Kearsley; Elsevier: Oxford, 1980.

6. Faucher, S.; Aluru, N.; Bazant, M. Z.; Blankschtein, D.; Brozena, A. H.; Cumings, J.; de Souza, J. P.; Elimelech, M.; Epsztein, R.; Fourkas, J. T.; Rajan, A. G.; Kulik, H. J.; Levy, A.; Majumdar, A.; Martin, C.; McEldrew, M.; Misra, R. P.; Noy, A.; Pham, T. A.; Reed, M.; Schwegler, E.; Siwy, Z.; Wang, Y.; Strano, M. Critical Knowledge Gaps in Mass Transport through Single-Digit Nanopores: A Review and Perspective. *J. Phys. Chem. C* **2019**, *123*, 21309−21326.
7. Steiner, P. A.; Gordy, W. Precision Measurement of Dipole Moments and Other Spectral Constants of Normal and Deuterated Methyl Fluoride and Methyl Cyanide. *J. Mol. Spectrosc.* **1966**, *21*, 291−301.
8. Saum, A. M. Intermolecular Association in Organic Nitriles; the CN Dipole-pair Bond. *J. Polym. Sci.* **1960**, *42*, 57−66.
9. Saitô, H.; Tanaka, Y.; Nagata, S.; Nukada, K. $^{13}C$ Nuclear Magnetic Resonance Studies on Molecular Association. I. Self-Association of Dipolar Molecules. *Can. J. Chem.* **1973**, *51*, 2118−2123.
10. Kratochwill, A.; Weidner, J. U.; Zimmermann, H., Röntgenstrukturuntersuchung des flüssigen Acetonitrils. *Ber. Bunsenges. Phys. Chem.* **1973,** *77*, 408−425.
11. Kratochwill, A. $^{13}C$-$^{1}H$ Intermolecular Relaxation Rate and Molecular Pair Distribution Function in Liquid Acetonitrile. *Ber. Bunsenges. Phys. Chem.* **1978**, *82*, 783−789.
12. Jorgensen, W. L.; Briggs, J. M. Monte Carlo Simulations of Liquid Acetonitrile with a Three-Site Model. *Mol. Phys.* **1988**, *63*, 547−558.

13. Torquato, S. Perspective: Basic Understanding of Condensed Phases of Matter via Packing Models. *J. Chem. Phys.* **2018**, *149*, 020901.

14. Berne, B. J.; Fourkas, J. T.; Walker, R. A.; Weeks, J. D. Nitriles at Silica Interfaces Resemble Supported Lipid Bilayers. *Acc. Chem. Res.* **2016**, *49*, 1605–1613.

15. Zhang, J.; Jonas, J. NMR Study of the Geometric Confinement Effects on the Anisotropic Rotational Diffusion of Acetonitrile-$d_3$. *J. Phys. Chem.* **1993**, *97*, 8812–8815.

16. Loughnane, B. J.; Farrer, R. A.; Scodinu, A.; Fourkas, J. T. Dynamics of a Wetting Liquid in Nanopores: An Optical Kerr Effect Study of the Dynamics of Acetonitrile Confined in Sol-Gel Glasses. *J. Chem. Phys.* **1999**, *111*, 5116–5123.

17. Loughnane, B. J.; Farrer, R. A.; Fourkas, J. T. Evidence for the Direct Observation of Molecular Exchange of a Liquid at the Liquid/Solid Interface. *J. Phys. Chem. B* **1998**, *102*, 5409–5412.

18. Farrer, R. A.; Fourkas, J. T. Orientational Dynamics of Liquids Confined in Nanoporous Sol-Gel Glasses Studied by Optical Kerr Effect Spectroscopy. *Acc. Chem. Res.* **2003**, *36*, 605–612.

19. Morales, C. M.; Thompson, W. H. Simulations of Infrared Spectra of Nanoconfined Liquids: Acetonitrile Confined in Nanoscale, Hydrophilic Silica Pores. *J. Phys. Chem. A* **2009**, *113*, 1922–1933.

20. Cheng., L.; Morrone, J. A.; Berne, B. J. Structure and Dynamics of Acetonitrile Confined in a Silica Nanopore. *J. Phys. Chem. C* **2012**, *116*, 9582–9593.
21. Hu, Z.; Weeks, J. D. Acetonitrile at Silica Surfaces and at Its Liquid-Vapor Interface: Structural Correlations and Collective Dynamics. *J. Phys. Chem. C* **2010**, *114*, 10202–10211.
22. Ding, F.; Hu, Z.; Zhong, Q.; Manfred, K.; Gattass, R. R.; Brindza, M. R.; Fourkas, J. T.; Walker, R. A.; Weeks, J. D. Interfacial Organization of Acetonitrile: Simulation and Experiment. *J. Phys. Chem. C* **2010**, *114*, 17651–17659.
23. Mountain, R. D. Molecular Dynamics Simulation of Water–Acetonitrile Mixtures in a Silica Slit. *J. Phys. Chem. C* **2013**, *117*, 3923–3939.
24. Denk, W.; Strickler, J. H.; Webb, W. W. Two-Photon Laser Scanning Fluorescence Microscopy. *Science* **1990**, *248*, 73–76.
25. Hell, S. W. Far-Field Optical Nanoscopy. *Science* **2007**, *316*, 1153–1158.
26. Durr, N. J.; Larson, T.; Smith, D. K.; Korgel, B. A.; Sokolov, K.; Ben-Yakar, A. Two-Photon Luminescence Imaging of Cancer Cells Using Molecularly Targeted Gold Nanorods. *Nano. Lett.* **2007**, *7*, 941–945.
27. Baldacchini, T. *Three-Dimensional Microfabrication Using Two-Photon Polymerization*; William Andrew: Oxford, 2016.
28. Liaros, N.; Fourkas, J. T. The Characterization of Absorptive Nonlinearities. *Laser Photonics Rev.* **2017**, *11*, 1700106.

29. Farrer, R. A.; Butterfield, F. L.; Chen, V. W.; Fourkas, J. T. Highly Efficient Multiphoton-Absorption-Induced Luminescence from Gold Nanoparticles. *Nano. Lett.* **2005**, *5*, 1139–1142.

30. Yoshino, F.; Polyakov, S.; Liu, M.; Stegeman, G. Observation of Three-Photon Enhance Four-Photon Absorption. *Phys. Rev. Lett.* **2003**, *91*, 063902.

31. Zheng, Q.; Zhu, H.; Chen, S.-C.; Tang, C.; Ma, E.; Chen, X. Frequency-Upconverted Stimulated Emission by Simultaneous Five-Photon Absorption. *Nat. Photonics* **2013**, *7*, 234–239.

32. Couris, S.; Koudoumas, A. A.; Ruth, A. A.; Leach, S. Concentration and Wavelength Dependence of the Effective Third-Order Susceptibility and Optical Limiting of $C_{60}$ in Toluene Solution. *J. Phys. B* 1**995**, *28*, 4537–4554.

# Chapter 2: Methods

## 2.1 *Molecular Simulation*

Molecular simulation is an invaluable tool for understanding the behavior of liquids and other many-body systems for which the analytic equations of motion cannot be solved exactly. This technique is used to describe the structural, thermodynamic, and dynamic behavior of a nanoscale system from the motions of its microscopic constituents. This section discusses the principles of the molecular simulations used in this thesis in the context of the classical, equilibrium statistical mechanics underpinning the technique.

In molecular simulations, a computer experiment is performed to follow explicitly the trajectories of a system that involves many degrees of freedom. The molecular models and interparticle interactions used in the simulation are designed to mimic the behavior of a real assembly of molecules. The validity of this technique rests on simulating the average properties of a large number $N$ of particles, which in simple cases ranges from a few hundred to a few thousand particles. These particles map out a $6N$-dimensional phase space that describes the dynamics of the particles in terms of their coordinates and momenta. Although these conjugate variables can be used to set up the equations of motion for the system, the goal of statistical mechanics and its realization in molecular simulations is to avoid doing so. In statistical mechanics, the central quantity of interest is the partition function, which connects the microscopic properties of the system at equilibrium to its thermodynamic functions. The partition function is used to normalize the probability that a system occupies a particular

microstate. Thermodynamic variables such as entropy and the free energy can then be expressed in terms of either the partition function or its derivatives. Different expressions for the partition function are given later in this section.

Even though statistical mechanics simplifies the many-body problem, few problems in this field are exactly solvable. To circumvent this problem, early atomistic models of liquids consisted of manipulating the packing of ball bearings representing atoms.[2] The advent of electronic computers allowed for the rapid development of computer simulation and concomitant advances in the study of liquids.

All molecular simulations must start with a configuration and suitable interaction potential or force field. The configuration consists of the coordinates of the molecules or atoms in a box that is typically on the order of a few nanometers in each dimension. Many common force fields are derived within the Born-Oppenheimer approximation, where the Hamiltonian of an atomic system can be expressed as a function of the nuclear variables. In molecular simulations of liquids, we can ignore quantum effects, because the thermal de Broglie wavelength for most liquids is much smaller than the interatomic separation. The classical Hamiltonian $\mathcal{H}$ for a system of $N$ atoms is then a sum of the kinetic and potential energies, and can be described via the set of coordinates $\boldsymbol{r_i}$ and momenta $\boldsymbol{p_i}$ of each atom $i$. In other words,

$$\mathcal{H}(\boldsymbol{r}, \boldsymbol{p}) = \mathcal{K}(\boldsymbol{p}) + \mathcal{V}(\boldsymbol{r}) \,, \tag{2.1}$$

where we have used a condensed notation such that

$$\boldsymbol{r} = (\boldsymbol{r}_1, \boldsymbol{r}_2, \dots, \boldsymbol{r}_N) \tag{2.2}$$

and

$$\boldsymbol{p} = (\boldsymbol{p}_1, \boldsymbol{p}_2, \dots, \boldsymbol{p}_N) \,. \tag{2.3}$$

The kinetic energy $\mathcal{K}$ then has the form

$$\mathcal{K}(\boldsymbol{p}) = \sum_{i=1}^{N} \boldsymbol{p}_i^2/2m_i \ , \tag{2.4}$$

where $m_i$ is the mass of the $i$th atom. The potential energy $\mathcal{V}$ contains all of the information about the interparticle interactions.

The potential can be decomposed into terms that depend on the atomic coordinates:[3]

$$\mathcal{V}(\boldsymbol{r}) = \sum_i v_1(\boldsymbol{r}_i) + \sum_i \sum_{j>i} v_2(\boldsymbol{r}_i, \boldsymbol{r}_j) + \sum_i \sum_{j>i} \sum_{k>j} v_3(\boldsymbol{r}_i, \boldsymbol{r}_j, \boldsymbol{r}_k) + \cdots . \tag{2.5}$$

The first term represents the effect of an external field and/or walls on the system, and the remaining terms represent interparticle interactions for pairs, triplets, and so on. Force fields are parameterized such that two-body interactions make up for the lack of three-body (triplet) interactions, which are rarely incorporated explicitly into molecular simulations. A notable exception is the use in polarizable force fields of mutually interacting sites to treat induction effects. Although many-body interactions that cannot be treated via a pairwise-additive force field are known to be important,[4] an effective pairwise approach is easily implemented, and captures many essential features of a liquid. Explicit many-body interactions are computationally more expensive to incorporate, and so were not used here.

The pair potential $v_2(\boldsymbol{r}_i, \boldsymbol{r}_j)$ consists of a steep, short-range repulsive wall that is attributed to non-bonded overlap between neighboring electron clouds (Pauli exclusion principle) and a slowly-varying, long-range tail due to attractions between instantaneous multipoles (London dispersion forces). A common, effective pair potential used in molecular simulations that qualitatively reproduces these features is the Lennard-Jones 12-6 potential, given by

$$v^{LJ}(r) = 4\varepsilon[(\sigma/r)^{12} - (\sigma/r)^{6}]\,, \tag{2.6}$$

where the parameters $\varepsilon$ and $\sigma$ are the well depth and site radius, respectively (Figure 2.1). The first term in Eq. (2.6) is approximate, and characterizes the short-range repulsion, whereas the second term, which can be derived using perturbation theory, characterizes the long-range attraction. In practice, the total Lennard-Jones interaction potential for a system is truncated at a cutoff distance $r_c$ due to the short-range nature of these interactions. Thus, Eq. (2.6) becomes

$$E_{LJ} = \sum_{i=1}^{N}\sum_{j>i}^{N} 4\varepsilon_{ij}\left[\left(\sigma_{ij}/r_{ij}\right)^{12} - \left(\sigma_{ij}/r_{ij}\right)^{6}\right] \quad (r \leq r_c)\,, \tag{2.7}$$

where the double sum counts over all pairs. The parameters between unlike sites are determined using mixing rules; a popular choice is the Lorentz-Berthelot rules, which use the geometric mean for the well depth and the algebraic mean for the site radius, i.e., $\varepsilon_{ij} = (\varepsilon_{ii}\varepsilon_{jj})^2$, $\sigma_{ij} = (\sigma_{ii} + \sigma_{jj})/2$.

Molecular simulations typically use a cutoff of at least $2.5\sigma$ for the Lennard-Jones interactions because the potential decreases as $1/r^6$ at large distances. The choice of cutoff distance affects computational efficiency, and extending the cutoff may require adjusting many other parameters of existing force fields, which is clearly not a desirable option. However, the attractive nature of the long-range interactions means that truncating them can have non-negligible effects on thermodynamic quantities such as the pressure. Truncating the dispersion interactions in this way is valid for a bulk liquid, which is homogenous and isotropic beyond the cutoff, but the method can produce errors in simulations of interfacial systems.[5] In all simulations reported in this thesis, the Lennard-Jones interactions for acetonitrile are truncated at a

distance of 14 Å, which is consistent with the original parameterization of the force field.[6]

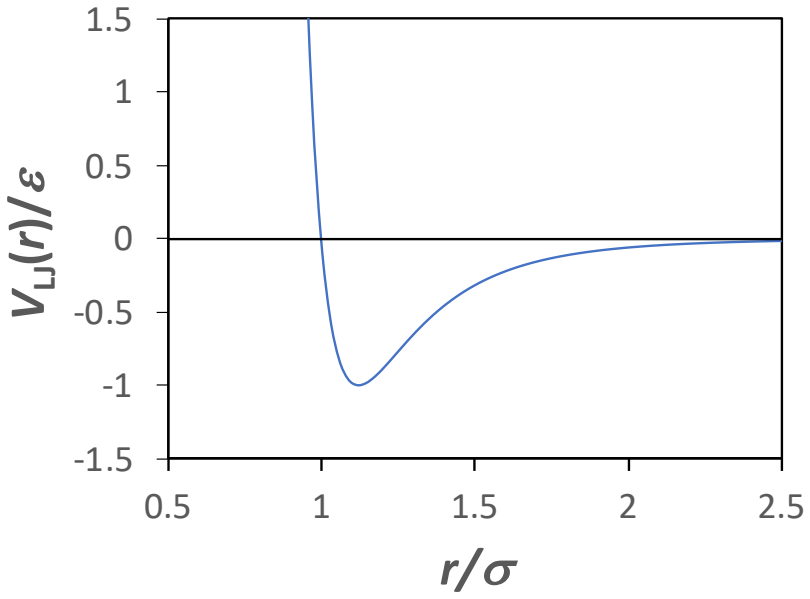


**Figure 2.1** Lennard-Jones potential $v_{Lj}(r)$ with well depth $\varepsilon$ and site radius $\sigma$.

For charged and multipolar species, the potential in Eq. (2.1) also includes Coulombic terms, which can be either attractive or repulsive. The electrostatic interaction between two sites is described by the Coulomb potential $E_{el}$:

$$E_{el} = \frac{q_i q_j}{4\pi\varepsilon_0 r_{ij}}, \tag{2.8}$$

where $q_i$ and $q_j$ are the charges on sites $i$ and $j$, and $\varepsilon_o$ is the permittivity of free space. The long-range nature of the Coulomb potential, which for charge-charge interactions falls off with $1/r$, is a problem in molecular simulations using periodic boundary conditions because the range of the potential is greater than half the box length. One solution would be to increase the size of the box to hundreds of nanometers, and

therefore increase the number of particles by several orders of magnitude, thereby decreasing the effective range of the potential. Clearly, this solution is not practical. A truncation of the potential at a fixed distance is also not a good idea, because the resulting sphere might be charged at any given time. One way of circumventing this problem is to use a lattice method, such as the Ewald sum,[7] originally developed to calculate the electrostatic energy of ionic crystals, to take into account the interaction of a particle with all of its periodic images.

The procedure for implementing the Ewald sum can be summarized as follows. To take into account periodic boundary conditions, Eq. (2.8) becomes[3]

$$E_{el} = \frac{1}{2}\sum_{i=1}^{N} q_i \left( \frac{1}{4\pi\varepsilon_0} \sum_{\boldsymbol{n}} \sum_{j=1}^{N} \frac{q_j}{|\boldsymbol{r}_{ij}+\boldsymbol{n}L|} \right), \tag{2.9}$$

where the sum over $\boldsymbol{n}$ is a vector of three integers, e.g., $\boldsymbol{n}$ = [0, 1, -1]. For a cubic box of length $L$, $\boldsymbol{n}L$ is the center of each box in the lattice. Note that the self-interaction, $i = j$ for $\boldsymbol{n} = [0,0,0]$, is excluded. In practice, the real-space summation given in Eq. (2.9) is computationally infeasible; the sum is not only conditionally convergent, but also converges slowly. Ewald summation recasts Eq. (2.9) by splitting the Coulomb interaction into two parts: a short-range contribution that is calculated in real space and a long-range contribution that is calculated in Fourier (reciprocal) space. Each point charge is surrounded by a Gaussian charge distribution $\rho_G(\boldsymbol{r}) = -q_i \left(\frac{\alpha}{\pi}\right)^{\frac{3}{2}} \exp(-\alpha \boldsymbol{r}^2)$ with width $\sqrt{2/\alpha}$ and equal magnitude but opposite sign relative to the point charge. The effective charge for each charge site then is given by

$$\rho_i(\boldsymbol{r}) = [q_i \delta(\boldsymbol{r} - \boldsymbol{r}_i) + \rho_G(\boldsymbol{r})]^S - [\rho_G(\boldsymbol{r})]^L, \tag{2.10}$$

where $\delta(\boldsymbol{r}-\boldsymbol{r_i})$ is the Dirac delta function. The superscripts $S$ and $L$ in Eq. (2.10) represent the short- and long-range contributions, respectively. Poisson's equation can then be solved to give the electrostatic potential as

$$E_{el} = \frac{1}{4\pi\varepsilon_0}\sum_{i=1}^{N}\sum_{j>i}^{N}\frac{q_i q_j}{r_{ij}}\mathrm{erfc}\left(\sqrt{\alpha}r_{ij}\right) + \frac{1}{2L^3\varepsilon_0}\sum_{0<k<k_c}\sum_{i=1}^{N}\sum_{j=1}^{N}\frac{q_i q_j}{r_{ij}}\exp\left(i\boldsymbol{k}\cdot(\boldsymbol{r}_i-\boldsymbol{r}_j)\right)exp\left(-\frac{k^2}{4\alpha}\right) - \frac{\alpha}{4\pi^{3/2}\varepsilon_0}\sum_{i=1}^{N}q_i^2 \quad \left(r_{ij} < r_c\right), \tag{2.11}$$

where $\mathrm{erfc}(x) = \left(2/\pi^{1/2}\right)\int_x^\infty \exp(-t^2)\,dt$ is the complementary error function, and $\boldsymbol{k}$ is the reciprocal wave vector chosen such that $\exp(-i\boldsymbol{k}\cdot\boldsymbol{n}L) = 1$. The cutoff wave vector $k_c$ is set to $k_c = \frac{2\pi}{Ln_c}$, where $n_c$ is a positive integer. The Ewald sum introduces errors because of the real- and reciprocal-space cutoffs. The errors are, respectively:

$$\delta E_R \sim \sum_{i=1}^{N} q_i^2 \sqrt{\frac{r_c}{2L^3}}\frac{\exp\left(-(\alpha r_c)^2\right)}{(\alpha r_c)^2} \tag{2.12}$$

$$\delta E_F \sim \sum_{i=1}^{N} q_i^2 \sqrt{\frac{n_c}{2L^2}}\frac{\exp\left(-(\pi n_c/\alpha L)^2\right)}{(\pi n_c/\alpha L)^2}\,. \tag{2.13}$$

These two cutoffs have the same accuracy (a tolerance of $1.0 \times 10^{-5}$ is used for the simulations reported in this thesis).

In molecular systems, terms representing chemical bonds also contribute to the interatomic potential energy in Eq. (2.1). Accordingly, the intramolecular energy

$E_{bonded}$ is the sum of bond stretching $E_{stretch}$, bond angle bending $E_{bend}$, and torsional rotation $E_{dihedral}$:

$$E_{bonded} = E_{stretch} + E_{bend} + E_{dihedral} \ . \tag{2.14}$$

Harmonic contributions are often used for the first two terms in Eq. (2.14), such that

$$E_{stretch} = \frac{1}{2} k_l (l - l_0)^2 \tag{2.15}$$

and

$$E_{bend} = \frac{1}{2} k_\theta (\theta - \theta_0)^2 \ , \tag{2.16}$$

where $l$ is the bond length, $l_0$ is the equilibrium bond length, $\theta$ is the bond angle, $\theta_0$ is the equilibrium angle, and $k_l$ and $k_\theta$ are the force constants for stretches and bends, respectively. The interaction sites are often centered on the experimental positions of the nuclei, which gives a basic representation of molecular shape, although fictitious sites can also be incorporated into the model to improve the electrostatic distribution.

There are two major classes of molecular simulations, Monte Carlo and molecular dynamics. Both methods are based on the above equations. In Monte Carlo simulations, a sequence of configurations is generated by random displacements of the particles. The acceptance probability of a trial configuration is determined according to a specific probability distribution, and averages of quantities are obtained over the set of configurations. In molecular dynamics simulations, we typically assume a classical dynamical model for the particles, and the trajectories are obtained by numerically integrating Newton's equations of motion. This latter technique gives information about the time evolution of the system. Here, we discuss only molecular dynamics simulations, which are used far more extensively in this thesis.

Conventional molecular dynamics simulations involve numerically approximating solutions to the classical (Newtonian) equations of motion for a many-body system. The equations of motion for the time-evolution of the system can be constructed from the potential energy $\mathcal{V}$ in Eq. (2.1) by calculating the forces $\boldsymbol{f}_i$ acting on all of the atoms:

$$m_i \ddot{\boldsymbol{r}}_i = \boldsymbol{f}_i \,, \tag{2.17}$$

where

$$\boldsymbol{f}_i = -\nabla \mathcal{V} \tag{2.18}$$

is the force on each atom.

In a conventional molecular dynamics simulation, the system is assigned a set of initial coordinates and a set of velocities drawn from a Maxwell-Boltzmann distribution for the given temperature. The temperature $T$ is determined from the ensemble average of the kinetic energy:[3]

$$\frac{3}{2} N k_B T = \langle \tfrac{1}{2} \textstyle\sum_i^N m_i \boldsymbol{v}_i^2 \rangle \,, \tag{2.19}$$

where $k_B$ is the Boltzmann constant. The pressure can then be determined from the virial theorem:[3]

$$P = \rho k_B T + \tfrac{1}{3V} \langle \textstyle\sum_{i=1}^N \sum_{j>i}^N \boldsymbol{f}_{ij} \cdot \boldsymbol{r}_{ij} \rangle \,, \tag{2.20}$$

where $\rho = N/V$ is the number density at volume $V$. The factor of 3 in both Eqs. (2.19) and (2.20) indicates that the system under study is three-dimensional. Molecular dynamics simulations are typically performed in the *NPT* or *NVT* ensemble, because most experiments are performed at constant temperature and/or pressure. To perform such simulations, a thermostat and/or barostat must be used. In this thesis, the Nosé-Hoover thermostat and barostat are used exclusively. An external degree of freedom is

introduced to correct the equation of motion (Eq. (2.17)) with a heat bath (in the case of the Nosé-Hoover thermostat) or a pressure bath (in the case of the barostat). The effective mass of the bath can be related to the relaxation constant for the thermostat or barostat. A large value for the effective mass, and hence for the relaxation constant, leads to weak coupling with the molecular system. The artificial degree of freedom effectively stretches the timescale of the extended system, so that it is usually necessary to equilibrate at the temperature and/or pressure of interest before doing the analysis in the *NVE* ensemble.

Typically, 1-fs time steps are used to integrate the equations of motion (Eq. (2.17)) because this step is ~10× shorter than the timescale of the fastest dynamic process, which is typically molecular vibrations involving hydrogen atoms. Configurations should be saved on the shortest timescale possible for which the correlation is below some predetermined threshold; this correlation can be determined from the autocorrelation $A_Q(\tau)$ for the quantity $Q_t = Q(t)$ of interest:

$$A_Q(\tau) = \frac{\langle Q_t Q_{t+\tau}\rangle - \langle Q_t\rangle^2}{\langle Q_t^2\rangle - \langle Q_t\rangle^2} . \tag{2.21}$$

This function should approach 0 as $\tau \to \infty$, with $A_Q(\tau) \to \exp(-\tau/\Theta)$ for an autocorrelation time $\Theta$. We can also define an integrated autocorrelation time:

$$\tau_A \equiv \int_0^\infty A_Q(\tau) d\tau . \tag{2.22}$$

For a purely exponential autocorrelation function, $\tau_A = \Theta$. For a simulation of length $t_{tot} \gg \tau_A$, the variance of the average value $\bar{Q}$ of the observable can be written as:

$$\sigma_{\bar{Q}}^2 \approx \frac{2\sigma_Q^2}{t_{tot}^2}\left[\int_0^{t_{tot}} \tau_A dt\right], \tag{2.23}$$

which simplifies to

$$\sigma_{\bar{Q}}^2 \approx \frac{2\sigma_Q^2}{t_{tot}/\tau_A} \ . \tag{2.24}$$

Rewriting Eq. (2.24) as

$$\sigma_{\bar{Q}}^2 \approx \frac{\sigma_Q^2}{n_A} \ , \tag{2.25}$$

where $n_A = t_{tot}/2\tau_A$, we find that the error in any observable in a molecular simulation is inversely proportional to the number of independent samples. Moreover, we find that the configurations that we use to compute the average value of the observable are independent only if they are evenly spaced by at least $2\tau_A$ units in time.

Regardless of the starting conditions, sufficient time must be allowed for the system to equilibrate before its analysis via a so-called production run. Equilibrium properties are then obtained as time averages of the observable over the trajectory. According to the ergodic hypothesis,[3] a time average $\langle A \rangle_{time}$,

$$\langle A \rangle_{time} = \frac{1}{\tau_{obs}} \sum_{\tau=1}^{\tau_{obs}} A\big(\Gamma(t)\big) \ , \tag{2.26}$$

corresponds to an ensemble average $\langle A \rangle_{ens}$,

$$\langle A \rangle_{ens} = \sum_{\Gamma} A(\Gamma)\, \rho_{ens}(\Gamma) \ , \tag{2.27}$$

where $\tau_{obs}$ indicates the timescale of the measurement, $\Gamma$ indicates a particular point in phase space as introduced previously, and $\rho_{ens}$ indicates the probability density.[3] The latter can be written as

$$\rho_{ens}(\Gamma) = w_{ens}(\Gamma)/Q \ , \tag{2.28}$$

where $w_{ens}(\Gamma)$ is a weighting function, and $Q$ is the partition function defined previously. To apply the ergodic hypothesis, we must assume that the probability density for the ensemble does not change with the time-evolution of the system. For

most molecular simulations, this assumption is valid, and we assume ergodicity rather than rigorously prove it.

For the simulations described in this thesis, we are concerned primarily with three ensembles: *NVE* (microcanonical), *NVT* (canonical), and *NPT* (isothermal/isobaric). The quasi-classical partition function for $N$ particles in the microcanonical ensemble is[3]

$$Q_{NVE} = \frac{1}{N!}\frac{1}{h^{3N}}\int d\boldsymbol{r}\, d\boldsymbol{p}\delta[\mathcal{H}(\boldsymbol{r},\boldsymbol{p}) - E]\,, \tag{2.28}$$

where $h$ is Planck's constant, the $N!$ in the denominator reflects the indistinguishability of the particles, and the integral denotes integration over all $6N$ coordinates. The delta function is used to select states with the desired energy $E$. For the canonical ensemble, the partition function is[3]

$$Q_{NVT} = \frac{1}{N!}\frac{1}{h^{3N}}\int d\boldsymbol{r}\, d\boldsymbol{p}\exp[-\mathcal{H}(\boldsymbol{r},\boldsymbol{p})/k_BT]\,. \tag{2.29}$$

In this ensemble, the energy can fluctuate and take on any value. Note that Eq. (2.29) is simply the Laplace transform of the partition function for the microcanonical ensemble given by Eq. (2.28). The exponential term is known as the Boltzmann distribution, which gives the probability of the system in a state with a specified energy and temperature. In the isothermal/isobaric ensemble, generating state points must allow for changes in both volume and energy, and the partition function can also be expressed as a function of the microcanonical partition function[8]

$$Q_{NPT} = \int Q_{NVE}dEdV\exp[-(\mathcal{H}(\boldsymbol{r},\boldsymbol{p}) + PV)/k_BT]\,. \tag{2.30}$$

The microcanonical ensemble, which represents isolated systems, can therefore be regarded as conceptually perhaps the simplest ensemble.

Ensembles fix three macroscopic variables to specify the equilibrium thermodynamic state of the system. The equivalence of ensembles for finite systems, such as those systems that are studied in molecular simulation, can be shown as follows.[3] Consider an ensemble for which the partition function and corresponding thermodynamic potential are $Q_F$ and $\Psi_F$, respectively. In this ensemble, the extensive thermodynamic variable $F$ is constant. The partition function for an ensemble in which the conjugate, intensive variable $f$ is constant is given by

$$Q_f = \int dF' \exp(-F'f) Q_{F'} , \tag{2.31}$$

and the corresponding thermodynamic potential is

$$\Psi_f = \Psi_F + Ff \tag{2.32}$$

by a Legendre transformation. The ensemble averages calculated in each ensemble are related to one another by

$$\langle A \rangle_f = \exp(\Psi_2) \int dF' \exp(-\Psi_{F'} - F'f) \langle A \rangle_{F'} . \tag{2.33}$$

In the thermodynamic limit, $\langle A \rangle_f = \langle A \rangle_F$. For a finite number of particles, we can study the behavior of the integral in Eq. (2.33) by expanding it about $\langle F \rangle_f$ in a Taylor series:

$$\langle A \rangle_f = \langle A \rangle_{F=\langle F \rangle_f} + \frac{1}{2} \left( \frac{\partial^2}{\partial F^2} \langle A \rangle_F \right)_{F=\langle F \rangle_f} \langle \delta F^2 \rangle_f + \cdots , \tag{2.34}$$

letting $F' = \langle F \rangle_f + \delta F'$. The fluctuation term $\langle \delta F^2 \rangle$ can be expressed as

$$\langle \delta F^2 \rangle_f = \frac{\partial^2 \Psi_f}{\partial f^2} = -\frac{\partial \langle F \rangle_f}{\partial f} = -\partial F / \partial f . \tag{2.35}$$

Returning to Eq. (2.34), we can truncate it after the second term and re-arrange it as

$$\langle A \rangle_F = \langle A \rangle_f - \frac{1}{2} \langle \delta F^2 \rangle_f \frac{\partial^2}{\partial F^2} \langle A \rangle_f , \tag{2.36}$$

which can be simplified to

$$\langle A\rangle_F = \langle A\rangle_f + \frac{1}{2}\frac{\partial}{\partial f}\left(\frac{\partial f}{\partial F}\right)\frac{\partial}{\partial f}\langle A\rangle_f \ . \tag{2.37}$$

Thus, the correction term in Eq. (2.34) decreases as $\mathcal{O}(N^{-1})$ because $F$ is extensive, and $f$ is intensive. The equivalence of ensembles means that we can calculate thermodynamic properties of a liquid as averages in any ensemble (see, e.g., Eqs. (2.19) and (2.20)). The fluctuations given by Eq. (2.34) are small but measurable in molecular simulations, and correspond to thermodynamic derivatives such as the heat capacity, which is, for example, easily calculated in the canonical ensemble.

Structural and dynamical quantities can also be calculated from molecular simulations.[3] An example of the former is the pair, or radial, distribution function $g(r)$, which gives the probability of finding a pair of atoms at a distance $r$, relative to the probability for a random distribution at the same density. The radial distribution function can be calculated as an ensemble average over pairs of atoms:

$$g(r) = \frac{V}{N^2}\langle \sum_i \sum_{j\neq i} \delta(\boldsymbol{r} - \boldsymbol{r}_{ij})\rangle \ . \tag{2.38}$$

The radial distribution function is important for several reasons. First, this function can be related, via statistical mechanics, to thermodynamic observables such as the energy and the second virial coefficient. Second, this function can be related, through a three-dimensional Fourier transform, to the static structure factor $S(Q)$ that is obtained via diffraction experiments:

$$S(Q) = 1 + 4\pi\rho \int_0^\infty r^2 \frac{\sin kr}{kr} g(r) dr \ , \tag{2.39}$$

where $Q$ is the momentum transfer, and $\rho$ is bulk density. This relation suggests that the radial distribution function can be used to model the structure of liquids. The radial distribution function is, in fact, the simplest and most direct way of modeling liquid

structure in real space, and as a result, calculations of $g(r)$ are used extensively in this thesis.

The results of molecular dynamics simulations can also be compared directly with experiment in the case of certain dynamical quantities. Spectroscopic information, in particular, can be regarded in many cases as the Fourier transform of an appropriate time-correlation function. The time integrals of these functions can also be related via Green-Kubo formulae[9] to transport coefficients such as the self-diffusivity. In this thesis, some spectroscopic results, particularly those from neutron scattering, are thus presented alongside data from molecular simulations.

## 2.2 *Neutron Scattering*

Molecular dynamics simulations and neutron-scattering experiments probe essentially the same length- and time-scales of a liquid. The scales depend on the trajectory length and the complexity of the force field in the case of molecular dynamics, and the spectrometer and the neutron source in the case of neutron scattering. The wavelike nature of neutrons means that the so-called "cold" and "thermal" neutrons ($E \sim 1$ to 60 meV) used in our experiments have wavelengths on the order of the interatomic spacings. The terahertz frequencies of the neutrons are close to the frequencies of the interatomic motions (e.g., librations), such that resolving collective dynamics is possible. Neutron scattering can therefore be used as a sensitive vibrational spectroscopy that is complementary to optical spectroscopy. Unlike Raman and infrared techniques, however, there are no selection rules for neutron scattering. In this

section, we give a brief overview of the principles of inelastic and quasielastic neutron scattering, in the context of studying liquid dynamics.

A scattering event is described by the momentum transfer $\boldsymbol{Q}$ that occurs:

$$\hbar\boldsymbol{Q} = \hbar\boldsymbol{k}_i - \hbar\boldsymbol{k}_f \tag{2.40}$$

and by the energy transfer $E$:

$$E = \frac{\hbar^2 k_i^2}{2m} - \frac{\hbar^2 k_f^2}{2m}, \tag{2.41}$$

where $\boldsymbol{k}_i$ and $\boldsymbol{k}_f$ are the wave vectors of the incident and scattered neutron, respectively, $\hbar$ is the reduced Planck's constant, and $m$ is the mass of the particle. The events measured in such an experiment are measured as a count rate per flux. The raw intensity can be related to a double differential cross-section, which is written as a function of $\boldsymbol{Q}$ and the frequency $\omega$ as

$$\frac{d^2\sigma}{d\Omega d\omega} = Nb^2 \left(\frac{k_f}{k_i}\right) \frac{1}{2\pi} S(\boldsymbol{Q}, \omega), \tag{2.42}$$

where $d\Omega$ is the element of the solid angle subtended by the scattering event, and $b$ is the scattering length.[10] The cross-section $\sigma$ is a measure of the probability that the scattering event occurs. The scattering function or dynamic structure factor $S(\boldsymbol{Q}, \omega)$ contains all information about the microscopic dynamics of a system for a process in which lowest-order perturbation theory, the so-called Born approximation, holds.[9] The static structure factor given in Eq. (2.39) is related to $S(\boldsymbol{Q}, \omega)$ by

$$\int_{-\infty}^{\infty} S(\boldsymbol{Q}, \omega)\, d\omega = S(Q). \tag{2.43}$$

The physical meaning of $S(\boldsymbol{Q}, \omega)$ becomes apparent by taking the following Fourier transform:

$$S(\boldsymbol{Q}, \omega) = \frac{1}{2\pi} \int_{-\infty}^{\infty} F(\boldsymbol{Q}, t) \exp(i\omega t)\, dt, \tag{2.44}$$

where $F(\boldsymbol{Q}, t)$ is the intermediate scattering function given by

$$F(\boldsymbol{Q}, t) = \frac{1}{N}\langle \rho_{\boldsymbol{Q}}(t)\rho_{-\boldsymbol{Q}}(0)\rangle \, . \tag{2.45}$$

The correlation function of the Fourier components of the density given by Eq. (2.45) can also be related to the spatial Fourier transform of the van Hove function, i.e.,

$$F(\boldsymbol{Q}, t) = \int G(\boldsymbol{r}, t) \exp(-i\boldsymbol{Q} \cdot \boldsymbol{r}) \, d\boldsymbol{r} \, , \tag{2.46}$$

where the van Hove function $G(\boldsymbol{r}, t)$ for a uniform liquid is defined as[10]

$$G(\boldsymbol{r}, t) = \frac{1}{N}\langle \sum_{i=1}^{N} \sum_{j=1}^{N} \int \delta\big[\boldsymbol{r} - \boldsymbol{r}_j(t) + \boldsymbol{r}_i(0)\big]\rangle \, , \tag{2.47}$$

Eq. (2.47) can be written as

$$G(\boldsymbol{r}, t) = \frac{1}{N}\langle \int \sum_{i=1}^{N} \sum_{j=1}^{N} \delta\big[\boldsymbol{r}' + \boldsymbol{r} - \boldsymbol{r}_j(t)\big]\delta[\boldsymbol{r}' - \boldsymbol{r}_i(0)] d\boldsymbol{r}'\rangle \, , \tag{2.48}$$

which is equal to

$$G(\boldsymbol{r}, t) = \frac{1}{N}\langle \int \rho(\boldsymbol{r}' + \boldsymbol{r}, t)\rho(\boldsymbol{r}', 0) d\boldsymbol{r}'\rangle \tag{2.49}$$

or, more compactly,

$$G(\boldsymbol{r}, t) = \frac{1}{\rho}\langle \rho(\boldsymbol{r}, t)\rho(\boldsymbol{0}, 0)\rangle \, . \tag{2.50}$$

Thus, the van Hove function is analogous to a time-dependent version of the $g(r)$ discussed in the previous section. The scattering problem is reduced, essentially, to a problem in statistical mechanics, and functions such as $S(Q)$, $\boldsymbol{S}(\boldsymbol{Q}, w)$, $F(\boldsymbol{Q}, t)$, and $G(\boldsymbol{r}, t)$ can be calculated via molecular simulation. Measuring the cross-section as a function of $\boldsymbol{Q}$ and $\omega$ allows for the experimental determination, in principle, of the time-dependent pair correlation function $G(\boldsymbol{r}, t)$. In practice, however, it is difficult to measure the van Hove function experimentally using inelastic neutron or X-ray scattering, because to carry out the double Fourier transform requires measurements

with good statistics, over large ranges of $\boldsymbol{Q}$ and $\omega$. Such measurements have only recently become possible.[11]

To gain insight into the dynamic structure factor $S(\boldsymbol{Q}, \omega)$, it is useful to separate the van Hove function $G(\boldsymbol{r}, t)$ into two additive components, a "distinct" contribution that correlates at different times the positions of different nuclei, and a "self" contribution that correlates the positions of the same nucleus at different times. The double differential cross-section in Eq. (2.42) can then be separated as follows:

$$\frac{d^2\sigma}{d\Omega d\omega} = \left(\frac{d^2\sigma}{d\Omega d\omega}\right)_{coh} + \left(\frac{d^2\sigma}{d\Omega d\omega}\right)_{inc}, \tag{2.51}$$

where the subscripts "coh" and "inc" refer, respectively, to coherent and incoherent processes. In coherent scattering, the neutron measures the decay of the inter-nuclei correlations as a function of time and space. In other words, coherent scattering is sensitive to collective phenomena, and all permutations of $i$ and $j$ are used in the calculation of the van Hove function in Eqs. (2.47) and (2.48), corresponding to the "distinct" part of $G(\boldsymbol{r}, t)$. In contrast, in incoherent scattering, there are no interference effects, and the neutron probes the decay of the density of a single nucleus as a function of time and space. In other words, incoherent scattering is insensitive to the relative distances between different nuclei because $i = j$, which corresponds to the "self" part of $G(\boldsymbol{r}, t)$.

To find the explicit forms of the coherent and incoherent parts of the double differential cross-section, we must use the fact that $S(\boldsymbol{Q}, \omega)$ contains a double sum over all scatterers:

$$S(\boldsymbol{Q}, \omega) = \sum_{i,j=1}^{N} \left(b_i b_j^*\right) S_{i,j}(\boldsymbol{Q}, \omega) . \tag{2.52}$$

For the coherent ($i \neq j$) and incoherent ($i = j$) terms, Eq. (2.52) becomes

$$S(\boldsymbol{Q},\omega) = \sum_{i\neq j}^{N} \overline{b_i b_j^*}\, S_{i,j}(\boldsymbol{Q},\omega) + \sum_{i=1}^{N} \overline{b_i^2}\, S_{i,i}(\boldsymbol{Q},\omega)\ , \qquad (2.53)$$

which can be re-written in the following form:

$$S(\boldsymbol{Q},\omega) = \sum_{i\neq j}^{N} \overline{b_i b_j^*}\, S_{i,j}(\boldsymbol{Q},\omega) + \sum_{i=1}^{N} \left(\overline{b_i^2} - (\bar{b}_i)^2\right) S_{i,i}(\boldsymbol{Q},\omega)\ . \qquad (2.54)$$

This separation occurs when there are at least two different nuclei in a sample, each nucleus with a different value of the neutron scattering length $b$, and the nuclei are randomly distributed. Cross-sections for different nuclei inherently have components of both coherent and incoherent scattering. Although the coherent scattering cross-section dominates for most elements, $^1$H is an important exception, as this atom has an incoherent neutron scattering cross-section that is approximately 20 times larger than those of most nuclei, and so is a strong incoherent scatterer.

Because coherent scattering gives information about the correlations that exist between all scatterers, there is, in principle, more information associated with coherent scattering. It is easier to extract information from incoherent scattering, however, because in coherent inelastic scattering it is not possible to calculate the density of states by a simple calculation of the eigenvectors of the normal modes.[12] In the incoherent approximation, in which all scattering is assumed to be incoherent, we insert the second term from Eq. (2.54) into Eq. (2.42) to give

$$\left(\frac{d^2\sigma}{d\Omega d\omega}\right)_{inc} = \frac{k_f}{k_i}\sum_{\kappa}\left(\overline{b_\kappa^2} - \left(\bar{b}_\kappa\right)^2\right) \mathrm{S}_\kappa(\boldsymbol{Q},\omega)\ . \qquad (2.55)$$

We want to extract the density of states from this information. To do so, we need to obtain an explicit form for the dynamic structure factor $S(\boldsymbol{Q},\omega)$, which is defined as[12]

$$\mathrm{S}_\kappa(\boldsymbol{Q},\omega) =$$

$$\frac{1}{2\pi\hbar}\sum_{j\in\{j_\kappa\}}\int_{-\infty}^{\infty}\langle \exp\left(-i\boldsymbol{Q}\cdot\boldsymbol{r}_j(0)\right)\exp\left(i\boldsymbol{Q}\cdot\boldsymbol{r}_j(t)\right)\rangle \exp(-i\omega t)\, dt\ . \qquad (2.56)$$

From the Bloch identity,[12] we have

$$\langle \exp\left(-i\boldsymbol{Q}\cdot\boldsymbol{u}_j(0)\right)\exp\left(-\boldsymbol{Q}\cdot\boldsymbol{u}_j(t)\right)\rangle =$$

$$\exp\left(-2W_j(\boldsymbol{Q})\right)\exp\langle\left(\boldsymbol{Q}\cdot\boldsymbol{u}_j(0)\right)\left(\boldsymbol{Q}\cdot\boldsymbol{u}_j(t)\right)\rangle\,, \qquad (2.57)$$

where $\boldsymbol{u}_i(t)$ is the displacement from the nucleus as a function of time, and $W(\boldsymbol{Q})$ is the Debye-Waller factor that also appears in X-ray crystallography. The first term in the expansion of $\langle\left(\boldsymbol{Q}\cdot\boldsymbol{u}_j(0)\right)\left(\boldsymbol{Q}\cdot\boldsymbol{u}_j(t)\right)\rangle$ gives the incoherent elastic scattering. The next term in this expansion is

$$\langle\left(\boldsymbol{Q}\cdot\boldsymbol{u}_j(0)\right)\left(\boldsymbol{Q}\cdot\boldsymbol{u}_j(t)\right)\rangle =$$

$$\frac{\hbar}{2}\sum_i\left\{\left[\frac{A_i(\boldsymbol{Q};j)}{\omega_i}(n(\omega_i)+1)\exp(i\omega_i t)\right]+\left[\frac{A_i(\boldsymbol{Q};j)}{\omega_i}n(\omega_i)\exp(-i\omega_i t)\right]\right\} \qquad (2.58)$$

with

$$A_i(\boldsymbol{Q};j)=\frac{(\boldsymbol{Q}\cdot\boldsymbol{e}_i(j))\cdot(\boldsymbol{Q}\cdot\boldsymbol{e}_i(j))^*}{m_j}=\frac{|\boldsymbol{Q}\cdot\boldsymbol{e}_i(j)|^2}{m_j}\,, \qquad (2.59)$$

where $\boldsymbol{e}_i(j)$ is the displacement in the vibrational mode $i$, and $n(\omega)$ is the Bose occupation factor. These equations, along with Eq. (2.57), allow us to re-write Eq. (2.56) as

$$S_\kappa(\boldsymbol{Q},\omega) =$$

$$\sum_{j\in\{j_\kappa\}}\frac{e^{-2W_j(\mathbf{Q})}}{2}\sum_i\frac{|\mathbf{Q}.\mathbf{e}_i(j)|^2}{m_\kappa\omega_i}\{(n(\omega_i)+1)\delta(\omega-\omega_i)]+[n(\omega_i)(\delta(\omega-\omega_i)\}\,. \qquad (2.60)$$

Thus, Eq. (2.55) becomes

$$\left(\frac{d^2\sigma}{d\Omega d\omega}\right)_{inc}=\frac{k_f}{k_i}\sum_\kappa\frac{\sigma_{inc}(\kappa)}{8\pi m_\kappa}\sum_{j\in\{j_\kappa\}}e^{-2W_j(\vec{q})}\sum_i\frac{|\mathbf{Q}.\mathbf{e}_i(j)|^2}{\omega_i}[(n(\omega)+1)\delta(\omega-\omega_i)]\qquad,$$

(2.61)

where $\sigma_{inc}(\kappa)=4\pi\sum_\kappa\left(\overline{b_\kappa^2}-\left(\bar{b}_\kappa\right)^2\right)$, and is the neutron incoherent scattering cross section for nuclei of type $\kappa$. Eq. (2.61) is the starting point for the analysis of our results

in Ch. 5 (see Eq. (5.4)). This equation enables us to obtain the density of states, which contains important spectroscopic information. Clearly, a scattering experiment is a long way from the single-phonon density of states. As will be demonstrated in this thesis, it is significantly easier to use molecular simulation to calculate the density of states, but the latter method relies on the quality of the force field, and multiphonon scattering is not trivial to incorporate.

An inelastic neutron-scattering experiment also gives quasielastic information, which can be compared to molecular simulation as well as to other types of spectroscopy. "Quasielastic" refers to the part of the inelastic-scattering spectrum (i.e., $S(\boldsymbol{Q},\omega)$ vs. $\omega$) in which there is symmetric broadening about the elastic line. The scattering function $S(\boldsymbol{Q},\omega)$ therefore is determined by of the convolution of one or more Lorentzians with the resolution function of the spectrometer. This observation is the starting point for the analysis of our results in Ch. 5 (see Eq. (5.8)).

The energy transfer corresponding to quasielastic scattering corresponds to stochastic processes such as the diffusion of a molecule in a liquid due to reorientational or translational motions. Unlike periodic motions such as librations and vibrations that contribute to the conventional inelastic spectrum, diffusion is not quantized, so the energy transfer can be small. Quasielastic neutron scattering is complementary to spectroscopic techniques such as dynamic light scattering. Unlike light scattering, however, the value of the momentum transfer $\boldsymbol{Q}$ in quasielastic neutron scattering is large, whereas in light scattering, the relatively low $\boldsymbol{Q}$ limits the analysis of fluctuations to the hydrodynamic regime.[13]

## 2.3 *References*


1. Baxter, R. J. *Exactly Solved Models in Statistical Mechanics*; Academic Press: London, 1982.
2. Finney, J. L. Bernal's Road to Random Packing and the Structure of Liquids. *Philos. Mag.* **2013**, *93*, 3940−3969.
3. Allen, M. P.; Tildesley, D. J. *Computer Simulation of Liquids*, 2nd ed.; Oxford University Press: Oxford, 2017.
4. DiStasio, Jr., R. A.; von Lilienfeld, O. A.; Tkatchenko, A. Collective Many-Body van der Waals Interactions in Molecular Systems. *Proc. Natl. Acad. Sci. U.S.A.* **2012**, *109*, 14791−14795.
5. Shirts, M. R.; Mobley, D. L.; Chodera, J. D.; Pande, V. S. Accurate and Efficient Corrections for Missing Dispersion Interactions in Molecular Simulations. *J. Phys. Chem. B* **2007**, *111*, 13052−13063.
6. Nikitin, A. M.; Lyubartsev, A. P. New Six-Site Acetonitrile Model for Simulations of Liquid Acetonitrile and Its Aqueous Mixtures. *J. Comput. Chem.* **2007**, *28*, 2020−2026.
7. Toukmaji, A. Y.; Board Jr., J. A. Ewald Summation Techniques in Perspective: A Survey. *Comput. Phys. Commun.* **1996**, *95*, 73−92.
8. McQuarrie, D. A. *Statistical Mechanics*; University Science Books: Mill Valley, 2000.
9. Hansen, J.-P.; McDonald, I. R. *Theory of Simple Liquids: with Applications to Soft Matter*, 4th ed.; Academic Press: London, 2013.

10. Lovesey, S. W. *Theory of Neutron Scattering from Condensed Matter, Vol. 1*; Oxford University Press: Oxford, 1984.
11. Egami, T.; Shinohara, Y. Correlated Atomic Dynamics in Liquid Seen in Real Space and Time. *J. Chem. Phys.* **2020**, *153*, 180902.
12. Schober, H. An Introduction to the Theory of Nuclear Neutron Scattering in Condensed Matter. *J. Neutron Res.* **2014**, *17*, 109−357.
13. Berne, B. J.; Pecora, R. *Dynamic Light Scattering: with Applications to Chemistry, Biology, and Physics*, Dover Publications: Mineola, 2000.

# Chapter 3: Determination of the Contributions of Two Simultaneous Absorption Orders using 2-Beam Action Spectroscopy

Adapted from: Liaros, N.; Cohen, S. R.; Fourkas, J. T. *Opt. Express* **2018**, *26*, 9492-9501.
Research designed by: Nikolaos Liaros and John T. Fourkas
Research conducted by: Nikolaos Liaros and Samuel R. Cohen
My contribution was to develop the analysis software and the linearization protocol.

## 3.1 *Introduction*

Nonlinear absorption plays a key role in many optical applications.[1-21] Although nonlinear absorption was first demonstrated more than 50 years ago,[22] the accurate characterization of this phenomenon remains challenging. For instance, most methods for determining the effective order of a nonlinear absorption process rely on making a logarithmic graph of an observable as a function of the average excitation power.[23] The slope of this type of plot should give the order of the dominant absorption process. However, the accurate determination of this order requires being able to measure the observable over several orders of magnitude of average excitation power. Furthermore, such plots are rarely linear, indicating that processes of two or more orders may contribute to the signal. Even when the plots are linear, the slope is often not integral, again suggesting that multiple processes contribute to the signal.

We recently introduced a technique[24] for the determination of the order of the effective absorptive nonlinearity in multiphoton absorption polymerization.[19-21] In this method, called 2-beam initiation threshold (2-BIT) spectroscopy, two pulse trains that are overlapped in space but are interleaved in time are used to expose a photoresist. The average power of one pulse train required to reach the polymerization threshold is measured as a function of the average power of the other pulse train. The order of the

nonlinear absorption process can be determined by plotting one average power versus the other. 2-BIT was employed to demonstrate that various photoinitiators are excited by either 2-photon or 3-photon absorption with ultrafast pulses tuned in the vicinity of 800 nm.[24]

2-BIT is the first example of a 2-beam action (2-BA) spectroscopy. The 2-BA concept can, in principle, be applied to any linear or nonlinear absorption process that yields a measureable signal. In the case of the photopolymerization threshold, the observable is single-valued. However, for observables that can take on many values, one can instead make 2-BA spectroscopy measurements for any desired value of the observable. Such a measurement reveals the effective number of photons involved in generating the observable at that particular value. This process can be repeated for different values of the observable.

As a representative example of the generalization of 2-BA spectroscopies, here we study the linear and nonlinear generation of photocurrent or photovoltage in a photodiode. The nonlinear optical production of photocurrent in different types of semiconductors has stimulated extensive theoretical and experimental investigations, and has found a vast number of applications.[25,26] This phenomenon has been used, for instance, to autocorrelate ultrafast laser pulses,[16,17,27–31] to explore the electronic properties of organic[32,33] and inorganic[34,35] semiconductors, to control photocurrent generation through coherence,[36-38] to generate electrical power,[39] to map the structure in composite materials,[40] and to "upconvert" mid-infrared light for detection in the near-ultraviolet.[41] Furthermore, the strong multiphoton absorption generally exhibited

by semiconductors has been used for applications such as optical limiting, induction of population inversion, processing of signals, and entanglement of photons.

We characterize the linear and nonlinear generation of photocurrent in a GaAsP photodiode with a 2-BA technique that we call 2-beam constant-amplitude photocurrent (2-BCAmP) spectroscopy. We use this example to demonstrate that 2-BA spectroscopy data offer substantial advantages over logarithmic plots in elucidating the nature of such processes. In particular, we introduce a framework for extracting the contributions of two different orders of absorption from 2-BA spectroscopy data. We also show how the dependence of the contributions of the two different absorption orders on the value of the observable can be used to test for self-consistency.

## 3.2 *Experimental Details*

A schematic of the 2-BCAmP concept is shown in Figure 3.1. The excitation source was a tunable, Ti:sapphire oscillator (Coherent Mira 900-F) that can be operated in either mode-locked (ML) or continuous-wave (CW) mode. The repetition rate of the laser in ML mode was 76 MHz, and the pulse duration was approximately 150 fs. The spatially filtered beam was chopped at 1 KHz and then split in two parts. The power of each beam was adjusted by means of a motorized half-wave plate and a Glan-Taylor polarizer, and the beam powers were measured using a power meter. Each beam was passed through a separate variable beam expander to allow for the adjustment of the beam spot size at the back aperture of the objective. The lengths of the two beam paths were adjusted so that consecutive pulses arrived at the sample with approximately equally spaced timings, giving an effective repetition rate of 152 MHz. The two beams were combined with a polarizing beam cube and made collinear, and then passed

through a quarter-wave plate.

The two beams were sent through the reflected-light illumination port of an inverted microscope and filled the back aperture of a 0.30 NA, 10×, infinity-corrected microscope objective (Zeiss, Plan-NEOFLUAR). The objective focused the beams onto a GaAsP photodiode (Hamamatsu G1117, with the resin coating removed). Average power values cited here were measured at the back aperture of the objective; the loss from the objective was ~30%. The beam diameter at the focal plane was approximately 3.25 μm. To eliminate any contribution from dark current, the photodiode output was sent to a lock-in amplifier (Stanford Research Systems, SR810) that was referenced to the chopping frequency. To maximize the signal-to-noise ratio, data were collected in current mode at low excitation powers and in voltage mode at high excitation powers. The detection mode did not influence the 2-BCAmP exponent.

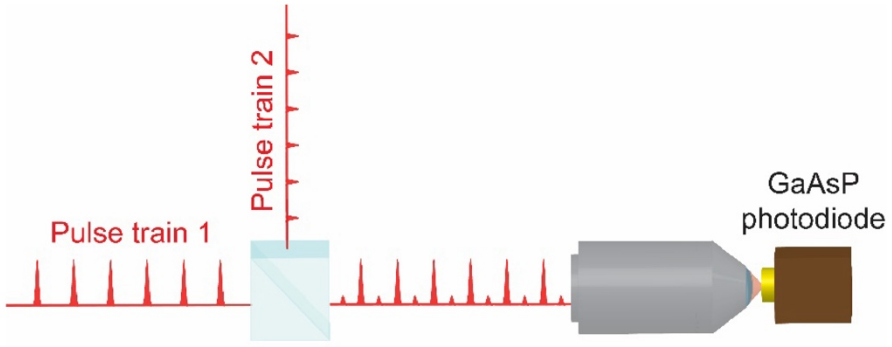


**Figure 3.6** Schematic depiction of a 2-beam constant-amplitude photocurrent experiment. Two trains of pulses whose amplitudes can be adjusted independently are interleaved and focused onto a photodiode. Multiple sets of average powers for the two pulse trains that generate the same photocurrent (or photovoltage) are determined, allowing for the measurement of the effective order of the absorption process in the photodiode.

The GaAsP photodiode was mounted on a motor-driven stage that allowed for sample positioning in the plane transverse to the laser beam. A separate motor drive

controlled the distance between the objective and the photodiode. The movements of the stages were controlled using LabVIEW programs. To control the position of each of the two excitation beams focused on the sample, the reflection of each laser beam from the photodiode surface was observed in real time using a CCD camera and a monitor. For measurements made in ML mode the beams were overlapped on the photodiode, whereas for measurements made in CW mode the beams were focused to neighboring positions but were not overlapped.

## 3.3 *Results and Discussion*

Figure 3.2 shows photocurrent excitation data collected for a GaAsP photodiode at an excitation wavelength of 800 nm. For one set of data, the laser was mode locked and the photodiode was placed at the focal plane of the objective. In this case, the slope of the logarithmic photocurrent excitation (PE) plot is $2.02 \pm 0.03$, which is suggestive of 2-photon absorption. The magnitude of the photovoltage is consistent with that reported previously.[29] For the other set of data the laser was operated in CW mode and the photodiode was moved 2.8 mm out of the focal plane of the objective. In this case the slope of the logarithmic PE plot is $1.07 \pm 0.03$, suggesting that the signal is dominated by linear absorption. Although the red edge of the specified detection range of this photodiode is at 680 nm, there is still a small linear signal even at wavelengths of 800 nm and longer due to the Urbach-tail[42] absorption of the semiconductor. At the highest average excitation powers the plot begins to diverge slightly from the fit line. This divergence is even clearer if the slope of the fit is constrained to unity, as seen in the dashed line in Figure 3.2(a). The average ML powers here range from 0.39 mW to 2.3 mW, corresponding to irradiances of 0.82 to 4.8

GW/cm$^2$.

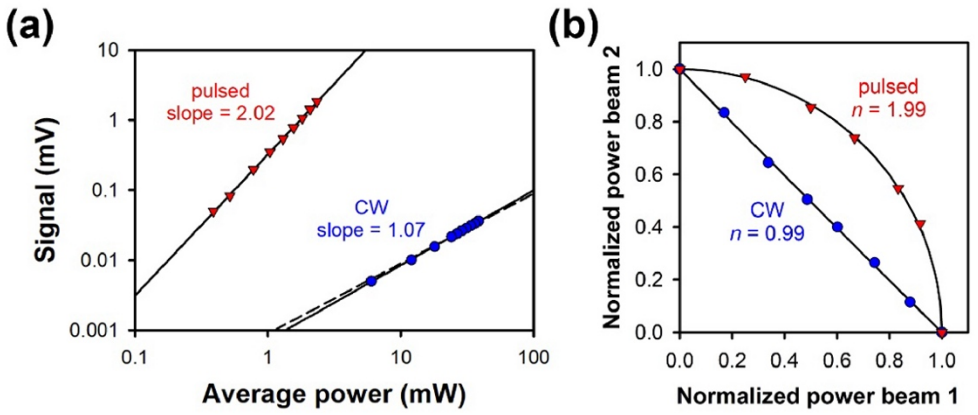


**Figure 3.2** (a) Logarithmic photocurrent excitation plots for a GaAsP photodiode for 800 nm excitation with a ML laser (at the focal plane) and a CW laser (out of the focal plane). The solid lines are free fits and the dashed line is a fit with the slope constrained to 1. (b) 2-BCAmP data collected under the same conditions. The error bars are smaller than the symbols in all cases.

Figure 3.2(b) shows 2-BCAmP plots for ML excitation in the focal plane and CW excitation away from the focal plane, for a specific chosen value of the photocurrent. In both cases the average laser power for each pulse train is normalized by the average power at which that pulse train alone yields the target value of the photocurrent. Using these normalized average powers, the 2-BCAmP plot follows the equation

$$\bar{P}_1^n + \bar{P}_2^n = 1\,, \tag{3.1}$$

where $n$ is the order of the absorption process.[24] For instance, a linear absorption process yields a linear 2-BCAmP plot, a 2-photon absorption process yields a 2-BCAmP plot that is a quarter of a circle, and so on. The data were fit using a nonlinear least squares routine,[43] yielding exponents of 1.99 ± 0.03 for the ML case and 0.99 ± 0.03 for the CW case. Thus, when the observed photocurrent arises through a single

absorption order, the 2-BCAmP results are consistent with the exponent derived from a conventional logarithmic PE plot.

We next consider what happens when more than one absorption order contributes to the photocurrent. In Figure 3.3(a) we show logarithmic PE plots for 800 nm ML excitation with the photodiode at the focal plane of the objective and at two different distances away from the focal plane. As the distance from the focal plane increases, so does the spot size, reducing the peak irradiance and, concomitantly, the contribution of 2-photon absorption. Thus, the slope of the PE plot decreases from a value of about 2 in the focal plane to a value of about 1.5 when the photodiode is 2.8 mm from the focal plane. None of the PE traces is completely linear. The in-plane trace shows signs of saturation at high average excitation powers, and the out-of-plane traces show signs of the slope increasing at higher average excitation powers.

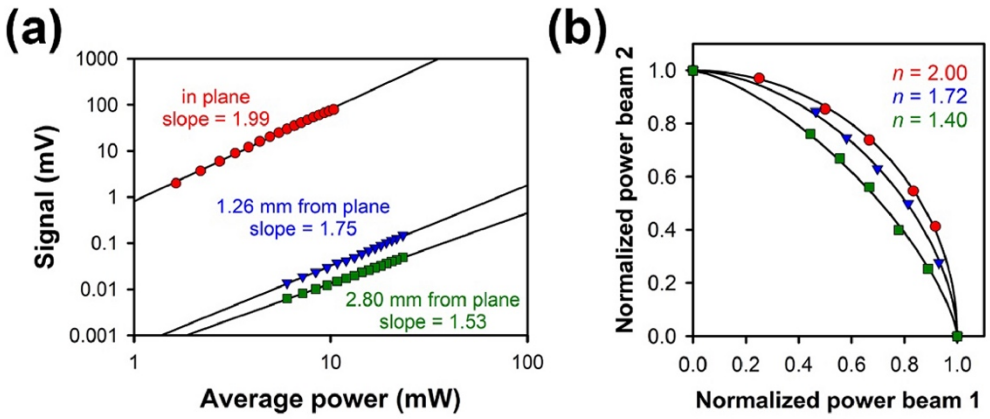


**Figure 3.3** (a) Logarithmic PE plots for ML 800 nm excitation, with the GaAsP photodiode different distances from the focal plane. (b) 2-BCAmP data collected under the same conditions.

Figure 3.3(a) illustrates some of the challenges inherent in using logarithmic PE plots to determine absorptive nonlinearities. Typically, the slopes of such plots are not integers. Furthermore, the accurate determination of the order of an absorption process

generally requires data that span several orders of magnitude of average excitation power, a problem that is related to the accurate fitting of power-law functions.[43] However, logarithmic PE plots are rarely linear over many orders of magnitude of average excitation power.

Logarithmic PE plots that are not linear or that have non-integer slopes can indicate that two or more orders of absorption contribute to the observed signal over the range of average excitation powers used. However, even if the two exponents are known, accurate fitting to such a function is also challenging, and is rarely performed for PE data. Consider the case of two contributions to the absorption that differ by an order of one, such that the signal $S$ as a function of irradiance $I$ is given by

$$S(I) = AI^n + BI^{n+1}\,. \tag{3.2}$$

Here, the coefficients $A$ and $B$ encompass the multiphoton absorption cross section, the quantum yield for photocurrent generation, and pulse shape factors relating to the absorption probability for the respective orders $n$ and $n + 1$.[45] At the irradiance for which 90% of the absorption probability is of order $n$ we have

$$\frac{BI^{n+1}}{AI^n} = \frac{BI}{A} = \frac{1}{9}\,. \tag{3.3}$$

Conversely, at the irradiance for which 90% of the absorption is of order $n + 1$ we have

$$\frac{BI^{n+1}}{AI^n} = \frac{BI}{A} = 9 \tag{3.4}$$

Thus, going from 90% order $n$ to 90% order $n + 1$ requires changing the irradiance, and

therefore the average excitation power, by a factor of 81. Similarly, if the orders of absorption vary by 2, going from 90% order $n$ to 90% order $n + 2$ requires a factor of 9 increase in irradiance. Reliable fitting of two different orders of absorption therefore generally requires data that span at least two orders of magnitude in average excitation power. Even in this scenario, the average excitation powers must lie in the range over which the dominant order of absorption changes. If these conditions are not met, as is the case for the data in Figure 3.3(a), then it is not possible to make an accurate determination of the relative contributions of different absorption orders at any given average excitation power for which the slope is not an integer.

Figure 3.3(b) shows 2-BCAmP data taken at the same three positions as the PE data in Figure 3.3(a), all at the same average excitation power of 15.6 mW for a single pulse train (this convention is used throughout this chapter when reporting powers). As is the case for PE data, the 2-BCAmP data that were not collected at the focal plane have best-fit exponents that are not integers. If the exponents between 1 and 2 arise from a combination of linear and 2-photon absorption, then we have

$$a(\bar{P}_1 + \bar{P}_2) + b(\bar{P}_1^2 + \bar{P}_2^2) = 1 \, . \tag{3.5}$$

We impose the constraint that $a + b = 1$, such that $a$ is the fractional contribution of linear absorption and $b$ is the fractional contribution of 2-photon absorption in the conditions under which the curve was obtained. There is then a unique value of $a$ for a given value of $n$ under these conditions. To determine the value of $a$ for a 2-BCAmP data set, we make the substitution $b = a - 1$ in Eq. (3.5) and rearrange to obtain

$$1 - \bar{P}_1^2 - \bar{P}_2^2 = a(\bar{P}_1 + \bar{P}_2 - \bar{P}_1^2 - \bar{P}_2^2) \, . \tag{3.6}$$

Thus, the slope of a plot of $1 - \bar{P}_1^2 - \bar{P}_2^2$ as a function of $\bar{P}_1 + \bar{P}_2 - \bar{P}_1^2 - \bar{P}_2^2$ will be $a$. An analogous approach can be used to extract the fractional contribution of any pair of orders of absorption from a 2-BA spectroscopy plot.

We show a representative plot of Eq. (3.6), for the 2-BCAmP data obtained 1.26 mm from the focal plane, in Figure 3.4(a). This approach was used in Figure 3.4(b) to determine the fractional contribution of 2-photon absorption at a fixed average power as a function of distance from the focal plane, based on the three 2-BCAmP data sets in Figure 3.3(b). In the case of a combination of linear and 2-photon absorption, the corresponding local slope of a logarithmic plot at a given excitation intensity is one plus the fraction of 2-photon absorption. For the data obtained 2.80 mm from the focal plane, the corresponding local slope calculated in this manner is 1.51, and for the data obtained 1.26 mm from the focal plane the corresponding slope is 1.80. Note that these values differ somewhat from the 2-BCAmP exponents, but the 2-BCAmP data allow the local slope to be calculated directly.

These data show that it is straightforward to use 2-BA spectroscopy to determine the relative contributions of two different known orders of absorption to an observable at a particular value. In contrast, the conventional logarithmic plot method requires measuring the observable over orders of magnitude in its value to determine the contributions of different orders of nonlinearity.

The relative contributions of linear and 2-photon absorption should depend on the average excitation power in a predictable manner, so we next consider 2-BCAmP data obtained with the photodiode 1.28 mm from the focal plane at three different average excitation powers: 15.6 mW, 19.2 mW, and 23.2 mW. As can be seen from the

data in Figure 3.5(a), the measured exponent changes from 1.72 to 1.80 over this range of average excitation powers, with an uncertainty of approximately ± 0.03 in each value. It is not possible to determine this small of a change in slope in a logarithmic PE plot over such a limited range of average excitation powers.

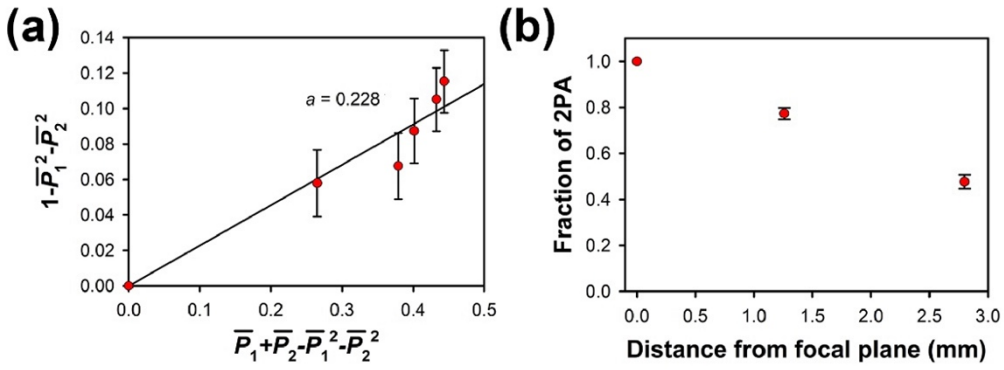


**Figure 3.4** (a) A representative linearized plot used to extract the fractional contribution of linear absorption from a 2-BCAmP data set. The line is a linear least-squares fit constrained to pass through the origin. (b) Fraction of photocurrent arising from 2-photon absorption at a fixed average laser power as a function of the distance of the photodiode from the focal plane.

Although in this case we can safely assume that the photocurrent should arise from linear absorption and 2-photon absorption, the 2-BCAmP data in Figure 3.5(a) can in principle be fit to the sum of a linear absorption process and any higher-order absorption process, giving different values of *a* and *b*. As shown above, if the orders of the two contributing absorption processes differ by one, then the ratio of the contribution of the higher-order process to that of the lower-order process is *BI*/*A*. In the 2-BCAmP fits we instead determine the normalized contributions *a* and *b*. Together, these results imply that *b*/*a* should increase linearly with the average power of the laser if the photocurrent arises from linear and 2-photon absorption. As can be seen in Figure 3.5(b), our results are in good agreement with this prediction. If we instead assume that the signal comes from a combination of linear and 3-photon

absorption, we can extract different values of *a* and *b* from the 2-BCAmP plots. If the signal arises from those two orders of absorption, then *b*/*a* should scale with the square of *I*. As can be seen from blue symbols in Figure 3.5(b), a plot of *b*/*a* as a function of *I* in this case is not a parabola that passes through the origin. Whenever two orders of absorption dominate in the generation of an observable, the ability to perform this type of consistency check makes it possible for 2-BA spectroscopy to be used to determine these orders, even if the orders are not known *a priori*.

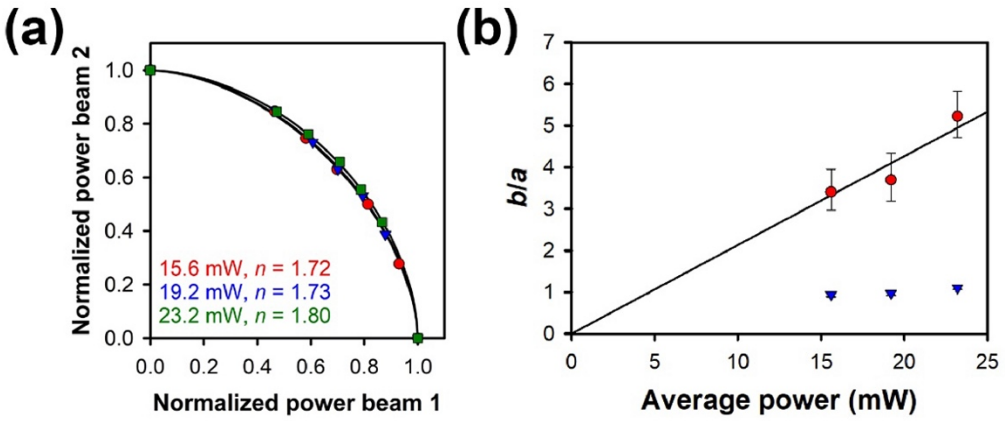


**Figure 3.5** (a) 2-BCAmP data for a GaAsP photodiode 1.28 mm from the focal plane of the objective for mode-locked 800 nm excitation at three different average powers. (b) Ratio of 2- photon to linear absorption as a function of average power from the three 2-BCAmP data sets (red symbols). The solid line is a linear least-squares fit, constrained to pass through the origin. The blue symbols are the values of *b*/*a* for fits to a linear absorption process and a 3-photon absorption process, in which case the ratio should depend on the square of the average power.

As was shown in Figure 3.2, 2-BCAmP measurements can be made not just with ML beams, but also with CW beams. Indeed, Ranka et al. observed a deviation in linearity in a logarithmic PE plot of data for CW irradiation of a GaAsP photodiode.[29] Their focusing was considerably gentler than what we have used here, so the increase in slope that they observed at high power was modest. They attributed this phenomenon to thermal effects rather than to the onset of 2-photon absorption.[29] To investigate this

effect, we performed additional 2-BCAmP measurements with CW beams.

The CW data in Figure 3.2 were obtained far from the focal plane of the objective. Figure 3.6(a) is a logarithmic PE plot for CW irradiation at the focal plane. It is clear from this plot that the nonlinear absorption in the photodiode is so strong that it can readily be driven by tightly focused CW light. The line in Figure 3.6(a) is a fit to a linear term plus a quadratic term, which is consistent with a combination of linear and 2-photon absorption. Because the data encompass only about an order of magnitude in excitation power, the data can also be fit nearly as well to the sum of a linear term and a cubic term.

Figure 3.6(b) shows corresponding 2-BCAmP data for three different values of the excitation power. The exponent for these three plots ranges from 1.31 to 1.56. Values of $b/a$ extracted using Eq. (3.6) by assuming the combination of a linear and a 2-photon absorption process are shown in Figure 3.6(c). This ratio is once again linear in the laser power, confirming the orders of absorption that contribute to the photocurrent. These data are consistent with the nonlinear response at high average excitation powers arising from nonlinear absorption.

We can compare the data in Figure 3.2(a) and Figure 3.6(a) to test whether nonlinear absorption could be of a sufficient magnitude to account for the nonlinearity in Figure 3.6(a). We find that CW excitation appears to be more than 34 times as efficient at generating a quadratic nonlinearity than is ML excitation. Although it is known that a correction must be made for non-square pulse shapes,[45] this factor can account for only about half of the observed difference in efficiencies.

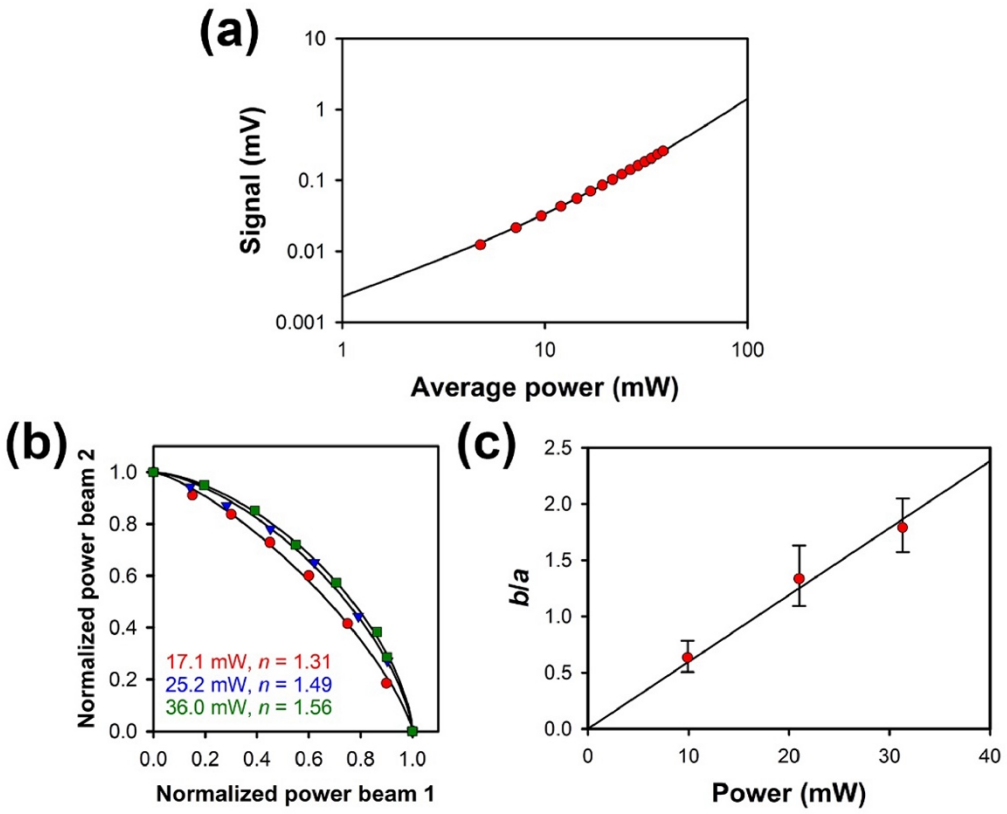


**Figure 3.6** (a) A logarithmic PE plot for a GaAsP photodiode for 800 nm CW excitation at the focal plane of the objective. The solid line is a fit to a linear term and a quadratic term. (b) 2-BCAmP data for different CW laser powers. (c) Ratio of 2-photon to linear absorption as a function of power from the three 2-BCAmP data sets. The solid line in the plot is a linear least- squares fit, constrained to pass through the origin.

The rise in temperature in GaAs under CW laser irradiation is known to be quadratic in power,[46] and we can assume that the same holds for GaAsP. Furthermore, the bandgap of GaAs is known to decrease linearly as a function of temperature.[47] If we assume that the Urbach tail of the GaAsP absorption is a linear (or nearly linear) function of frequency at 800 nm, then we would expect that thermal effects would exhibit a quadratic power dependence in this system. Thus, either 2-photon absorption or thermal effects could be consistent with the observed quadratic contribution at higher CW intensities. However, the small temperature rise expected in the Urbach tail[46] in

conjunction with the weak dependence of the bandgap on temperature[47] suggest that thermal effects should be minimal in this system. This conundrum is a subject of ongoing research.

## 3.4 *Conclusions*

We have characterized linear and nonlinear absorption in a photodiode using 2-beam constant-amplitude photocurrent spectroscopy. This work demonstrates the generalizability of the 2-beam action spectroscopy concept. Here we report, for the first time, 2-BA exponents that, within experimental uncertainty, are not integers. The non-integer exponents were shown to arise from a combination of linear and 2-photon absorption. We presented a framework for extracting the relative contributions of different orders of absorption from 2-BA spectroscopy data. We also used the ratio of the contributions to validate that the absorption does arise from the two expected orders, and that any contribution of thermal effects is negligible.

The 2-BA spectroscopy approach offers significant advantages over traditional logarithmic plots of an observable as a function of average excitation power, particularly when multiple orders of absorption are involved. Rather than requiring data obtained over several orders of magnitude in the average excitation power (and, consequently, even more orders of magnitude in the observable), 2-BA spectroscopies can be used to determine the effective exponent at each chosen value of the observable. A 2-BA plot does involve a combination of different average excitation powers that may span an order of magnitude, but offers the ability to determine a well-defined exponent at each chosen value of the observable, as well as the ability to use these exponents to test models for the absorption processes that contribute to the signal.

The 2-BA spectroscopy approach should be applicable to virtually any observable that arises from linear absorption, nonlinear absorption, or any combination thereof. The ability to determine unambiguously the orders of absorption that contribute to the observable can further provide invaluable mechanistic information that can be used to optimize materials. Although the treatment presented here allows for the determination of two orders of absorption that contribute to an observable, this approach should be able to be extended to a larger number of orders. Such an extension will require obtaining 2-BA spectroscopy data over a greater range of values of the observable.

## 3.5 *References*


1. Tutt, L. W.; Boggess, T. F. A Review of Optical Limiting Mechanisms and Devices Using Organics, Fullerenes, Semiconductors and Other Materials. *Prog. Quantum Electron.* **1993**, *17*, 299-338.
2. Liaros, N.; Aloukos, P.; Kolokithas-Ntoukas, A.; Bakandritsos, A.; Szabo, T.; Zboril, R.; Couris, S. Nonlinear Optical Properties and Broadband Optical Power Limiting Action of Graphene Oxide Colloids. *J. Phys. Chem. C* **2013**, *117*, 6842-6850.
3. Venkatram, N.; Rao, D. N.; Akundi, M. A. Nonlinear Absorption, Scattering and Optical Limiting Studies of CdS Nanoparticles. *Opt. Express* **2005**, *13*, 867-872.
4. Manzoni, C.; Mücke, O. D.; Cirmi, G.; Fang, S.; Moses, J.; Huang, S.-W.; Hong, K.-H.; Cerullo, G.; Kärtner, F. X. Coherent Pulse Synthesis: Towards Sub-Cycle Optical Waveforms. *Laser Photonics Rev.* **2015**, *9*, 129-171.

5. Keller, U. Recent Developments in Compact Ultrafast Lasers. *Nature* **2003**, *424*, 831-838.
6. Brabec, T.; Krausz, F. Intense Few-Cycle Laser Fields: Frontiers of Nonlinear Optics. *Rev. Mod. Phys.* **2000**, *72*, 545-591.
7. Banfi, G.; Degiorgio, V.; Ricard, D. Nonlinear Optical Properties of Semiconductor Nanocrystals. *Adv. Phys.* **1998**, *47*, 447-510.
8. Tanaka, K. Optical Nonlinearity in Photonic Glasses. *J. Mater. Sci. Mater. Electron.* 2005, *16*, 633-643.
9. Denk, W.; Strickler, J. H.; Webb, W. W. Two-Photon Laser Scanning Fluorescence Microscopy. *Science* **1990**, *248*, 73-76.
10. Durr, N. J.; Larson, T.; Smith, D. K.; Korgel, B. A.; Sokolov, K.; Ben-Yakar, A. Two-Photon Luminescence Imaging of Cancer Cells Using Molecularly Targeted Gold Nanorods. *Nano Lett.* **2008**, *7*, 941-945.
11. Bhawalkar, J. D.; Kumar, N. D.; Zhao, C. F.; Prasad, P. N. Two-Photon Photodynamic Therapy. *J. Clin. Laser Med. Surg.* **1997**, *15*, 201-204.
12. Celli, J. P.; Spring, B. Q.; Rizvi, I.; Evans, C. L.; Samkoe, K. S.; Verma, S.; Pogue, B. W.; Hasan, T. Imaging and Photodynamic Therapy: Mechanisms, Monitoring, and Optimization. *Chem. Rev.* **2010**, *110*, 2795-2838.
13. Parthenopoulos, D. A.; Rentzepis, P. M. Three-Dimensional Optical Storage Memory. *Science* **1989**, *245*, 843-845.
14. Olson, C. E.; Previte, M. J.; Fourkas, J. T. Efficient and Robust Multiphoton Data Storage in Molecular Glasses and Highly Crosslinked Polymers. *Nat. Mater.* **2002**, *1*, 225-228.

15. Iliopoulos, K.; Krupka, O.; Gindre, D.; Sallé, M. Reversible Two-Photon Optical Data Storage in Coumarin-Based Copolymers. *J. Am. Chem. Soc.* 2010, *132*, 14343-14345.
16. LaFratta, C. N.; Li, L.; Fourkas, J. T. Rapid, In-Line, Non-Interferometric Auto- and Cross-Correlator for Microscopy. *Opt. Express* **2006**, *14*, 111215.
17. Millard, A. C.; Fittinghoff, D. N.; Squier, J. A.; Müller, M.; Gaeta, A. L. Using GaAsP Photodiodes to Characterize Ultrashort Pulses Under High Numerical Aperture Focusing in Microscopy. *J. Microsc.* **1999**, *193*, 179-181.
18. Maruo, S.; Nakamura, O.; Kawata, S. Three-Dimensional Microfabrication with Two-Photon-Absorbed Photopolymerization. *Opt. Lett.* **1997**, *22*, 132-134.
19. LaFratta, C. N.; Fourkas, J. T.; Baldacchini, T.; Farrer, R. A. Multiphoton Fabrication. *Angew. Chem. Int. Ed. Engl.* **2007**, *46*, 6238-6258.
20. Baldacchini, T. *Three-Dimensional Microfabrication Using Two-Photon Polymerization*; Elsevier, Waltham, MA, 2016.
21. Stampfl, J.; Liska, R.; Ovsianikov, A. *Multiphoton Lithography: Techniques, Materials and Applications*; Wiley-VCH, Weinheim, Germany, 2017.
22. Kaiser, W.; Garrett, C. G. B. Two-Photon Excitation in $CaF_2$:$Eu^{2+}$. *Phys. Rev. Lett.* **1961**, *7*, 229-231.
23. Liaros, N.; Fourkas, J. T. The Characterization of Absorptive Nonlinearities. *Laser Photonics Rev.* **2017**, *11*, 1700106.

24. Tomova, Z.; Liaros, N.; Gutierrez Razo, S. A.; Wolf, S. M.; Fourkas, J. T. In Situ Measurement of the Effective Nonlinear Absorption Order in Multiphoton Photoresists. *Laser Photonics Rev.* **2016**, *10*, 849-854.
25. Hayat, A.; Nevet, A.; Ginzburg, P.; Orenstein, M. Applications of Two-Photon Processes in Semiconductor Photonic Devices: Invited Review. *Semicond. Sci. Technol.* **2011**, *26*, 083001.
26. Nathan, V.; Mitra, S. S.; Guenther, A. H. Review of Multiphoton Absorption in Crystalline Solids. *J. Opt. Soc. Am. B* **1985**, *2*, 294-316.
27. Langlois, P.; Ippen, E. P. Measurement of Pulse Asymmetry by Three-Photon-Absorption Autocorrelation in a GaAsP Photodiode. *Opt. Lett.* **1999**, *24*, 1868-1870.
28. Laughton, F. R.; Marsh, J. H.; Barrow, D. A.; Portnoi, E. L. The Two-Photon Absorption Semiconductor Waveguide Autocorrelator. *IEEE J. Quantum Electron.* **1994**, *30*, 838-845.
29. Ranka, J. K.; Gaeta, A. L.; Baltuska, A.; Pshenichnikov, M. S.; Wiersma, D. A. Autocorrelation Measurement of 6-fs Pulses Based on the Two-Photon-Induced Photocurrent in a GaAsP Photodiode. *Opt. Lett.* **1997**, *22*, 1344-1346.
30. Streltsov, A. M.; Moll, K. D.; Gaeta, A. L.; Kung, P.; Walker, D.; Razeghi, M. Pulse Autocorrelation Measurements Based on Two- and Three-Photon Conductivity in a GaN Photodiode. *Appl. Phys. Lett.* **1999**, *75*, 3778-3780.
31. Krug, T.; Lynch, M.; Bradley, A. L.; Donegan, J. F.; Barry, L. P.; Folliot, H.; Roberts, J. S.; Hill, G. High- Sensitivity Two-Photon Absorption Microcavity Autocorrelator. *IEEE Photonics Technol. Lett.* **2004**, *16*, 1543-1545.

32. Garbugli, M.; Gambetta, A.; Schrader, S.; Virgili, T.; Lanzani, G. Multi-Photon Non-Linear Photocurrent in Organic Photodiodes. *J. Mater. Chem.* **2009**, *19*, 7551-7560.

33. Koeppe, R.; Müller, J. G.; Lupton, J. M.; Feldmann, J.; Scherf, U.; Lemmer, U. One- and Two-Photon Photocurrents from Tunable Organic Microcavity Photodiodes. *Appl. Phys. Lett.* **2003**, *82*, 2601-2603.

34. Walters, G.; Sutherland, B. R.; Hoogland, S.; Shi, D.; Comin, R.; Sellan, D. P.; Bakr, O. M.; Sargent, E. H. Two-Photon Absorption in Organometallic Bromide Perovskites. *ACS Nano* **2015**, *9*, 9340-9346.

35. Zhou, F.; Ji, W. Giant Three-Photon Absorption in Monolayer $MoS_2$ and Its Application in Near-Infrared Photodetection. *Laser Photonics Rev.* **2017**, *11*, 1700021.

36. Atanasov, R.; Haché, A.; Hughes, J. L. P.; van Driel, H. M.; Sipe, J. E. Coherent Control of Photocurrent Generation in Bulk Semiconductors. *Phys. Rev. Lett.* **1996**, *76*, 1703-1706.

37. Dupont, E.; Corkum, P. B.; Liu, H. C.; Buchanan, M.; Wasilewski, Z. R. Phase-Controlled Currents in Semiconductors. *Phys. Rev. Lett.* **1995**, *74*, 3596-3599.

38. Haché, A.; Kostoulas, Y.; Atanasov, R.; Hughes, J. L. P.; Sipe, J. E.; van Driel, H. M. Observation of Coherently Controlled Photocurrent in Unbiased, Bulk GaAs. *Phys. Rev. Lett.* **1997**, *78*, 306-309.

39. Fathpour, S.; Tsia, K. K.; Jalali, B. Two-Photon Photovoltaic Effect in Silicon. *IEEE J. Quantum Electron.* **2007**, *43*, 1211-1217.

40. Parkinson, P.; Lee, Y.-H.; Fu, L.; Breuer, S.; Tan, H. H.; Jagadish, C. Three-Dimensional in Situ Photocurrent Mapping for Nanowire Photovoltaics. *Nano Lett.* **2013**, *13*, 1405-1409.

41. Fishman, D. A.; Cirloganu, C. M.; Webster, S.; Padilha, L. A.; Monroe, M.; Hagan, D. J.; Van Stryland, E. W. Sensitive Mid-Infrared Detection in Wide-Bandgap Semiconductors Using Extreme Non-Degenerate Two-Photon Absorption. *Nat. Photonics* **2011**, *5*, 561-565.

42. Marquardt, D. W. An Algorithm for Least-Squares Estimation of Nonlinear Parameters. *J. Soc. Ind. Appl. Math.* **1963**, *11*, 431-44.

43. Chopra, K. L.; Bahl, S. K. Exponential Tail of the Optical Absorption Edge of Amorphous Semiconductors. *Thin Solid Films* **1972**, *11*, 377-388.

44. Clauset, A.; Shalizi, C. R.; Newman, M. E. J. Power-Law Distributions in Empirical Data. *SIAM Rev.* **2009**, *51*, 661-703.

45. Xu, C.; Webb, W. W. Measurement of Two-Photon Excitation Cross Sections of Molecular Fluorophores with Data from 690 to 1050 nm. *J. Opt. Soc. Am. B* **1996**, *13*, 481-491.

46. Abbott, D.; Davis, B.; Gonzalez, B.; Hernandez, A.; Eshraghian, K. Modelling of Low Power CW Laser Beam Heating Effects on a GaAs Substrate. *Solid-State Electron.* **1998**, *42*, 809-816.

47. Johnson, S. R.; Tiedje, T. Temperature Dependence of the Urbach Edge in GaAs, *J. Appl. Phys.* **1995**, *78*, 5609-5613.

# Chapter 4: Extracting Information on Linear and Nonlinear Absorption from Two-Beam Action Spectroscopy Data

Adapted from: Cohen, S. R.; Fourkas, J. T. *J. Phys. Chem. A* **2019**, *123*, 7314-7322.
Research designed by: John T. Fourkas
Research conducted by: Samuel R. Cohen and John T. Fourkas
I developed some of this protocol.

## 4.1 *Introduction*

Multiphoton absorption (MPA) is one of the most commonly used nonlinear optical phenomena, particularly in ultrafast optics.[1-4] MPA is a powerful spectroscopic tool[5-8] and is also a key enabling technology for applications such as fluorescence microscopy,[9-15] microfabrication,[16-22] and optical data storage.[23-26] As a result, it is desirable to be able to characterize nonlinear absorption (NLA) processes accurately. For instance, it is often advantageous to maximize the MPA cross section of molecules or materials to make the nonlinear absorption process as efficient as possible. Accurate determination of an MPA cross section requires knowledge of the order of the nonlinear absorption as well as the nature of any competing processes, such as excited-state absorption (ESA).[27-29] Typical methods for characterizing MPA cannot reveal the contributions of multiple absorption pathways unambiguously.

NLA processes can be characterized either directly or indirectly. In the former case, the transmission loss of a laser beam is measured.[30-32] Most direct techniques detect weak MPA over a large background signal, so it is difficult to extract detailed information regarding complex photophysical or photochemical processes. Indirect methods rely on the detection of some proxy observable, such as emission or photocurrent, that is generated by MPA.[33-40] The most common method of measuring the order of NLA from either direct or indirect methods is to create a logarithmic plot

of the observable as a function of irradiance. The order of NLA is determined from the slope of such a plot. However, accurate determination of the order of absorption generally requires data that span two or more orders of magnitude in the irradiance.[41] Furthermore, it is common for noninteger slopes to be observed, in which case multiple orders of absorption and/or other processes such as ESA may be present. Unless considerable dynamic range is available, logarithmic plots cannot be used to ascertain unambiguously which processes contribute to the observed signal or what the relative magnitudes of these contributions are.

Another approach for characterizing NLA is the *Z*-scan technique.[42-50] The *Z* scan is a direct method in which loss is measured as a function of the distance of the sample from the laser focus. The order of MPA in a *Z* scan is determined by fitting the shape of the loss curve. Under favorable conditions, it is possible to ascertain the order of a single absorption process from a *Z*-scan measurement,[51,52] but the accurate determination of the influence of multiple processes is again challenging.

A further complication arises when MPA drives an irreversible process, particularly one such as photopolymerization, that has an exposure threshold. Under such circumstances it is usually not possible to make logarithmic plots, and *Z*-scan studies are not feasible. The usual approach to this problem is to make measurements in a medium in which the reactivity of the excited species is unimportant, such as an inert solvent. However, there is no guarantee that the absorption process observed under such circumstances is the same as the one that leads to the irreversible phenomenon in the medium of interest. Alternative approaches that make measurements as a function of laser repetition rate[39] and/or exposure time[40] can also be

used to glean insights into the order of NLA. Such methods still cannot provide an unambiguous description of the NLA process when multiple channels are involved.

We have recently developed a class of techniques that address many of the shortcomings of conventional methods for determining the effective order of NLA.[53-56] These methods, called two-beam action (2-BA) spectroscopies, rely on using two temporally interleaved pulse trains to generate an observable by nonlinear and/or linear absorption. By finding different sets of average powers for the two pulse trains that lead to the same value of an observable, it is possible to determine the effective order of NLA at that specific value of the observable. We have used this technique to probe NLA-induced observables including polymerization,[53,56] emission,[55] and photocurrent.[54]

As we have shown previously,[54] one of the advantages of 2-BA spectroscopies is that when multiple phenomena contribute to the measured exponent, it is possible to determine the order and/or nature of these phenomena. The strategy that we demonstrated for elucidating the different contributions is to make 2-BA measurements at a range of values of the observable and then to test the results against a model. The above approach is applicable only when 2-BA measurements can be made at several values of an observable. There are many situations in which 2-BA measurements can be made over only a limited range of observable values. The extreme example of this situation is photopolymerization,[53] for which there is only one value of the observable (the threshold exposure dose).

Here we explore in more detail the relationship between the analysis of NLA via logarithmic plots and 2-BA spectroscopy when two orders of absorption are

involved. We demonstrate that under these circumstances the standard equation used to fit 2-BA plots is only approximate. We examine six different combinations of orders of absorption and show how the 2-BA plot deviates from an "ideal" 2-BA plot with a single noninteger exponent as the relative contributions of the two orders are varied. Based on these results, we demonstrate how the orders and magnitudes of the two absorption contributions can usually be distinguished even if it is only possible to obtain data at one value of the observable.

## 4.2 *Theory*

The concept of 2-BA spectroscopy is illustrated in Figure 4.1(A). Two temporally interleaved pulse trains are incident upon the sample of interest at irradiances far below the saturation regime, generating an observable signal. If the delay time between two temporally adjacent pulses is long enough for the electronic excitation to relax completely, then the action of each pulse can be considered in isolation. The average power of one of the pulse trains (which we will call beam 1) required to attain a particular value of the observable is first determined. Beam 2 is then adjusted to have a nonzero average power, and the average power of beam 1 that returns the observable to its selected value is determined. This process is repeated until only beam 2 has nonzero average power.

In principle, the average power at which each individual beam gives the desired value of the observable should be identical. In practice, these average powers may vary slightly. As a result, normalized powers are typically used in 2-BA spectroscopies, i.e., the average power of a given beam divided by the average power at which that beam alone yields the desired value of the observable. In this situation, for an $m$-photon

absorption process the 2-BA data will adhere to the relation[53]

$$\bar{P}_1^m + \bar{P}_2^m = 1\,, \tag{4.1}$$

where an overbar indicates a normalized average power. Thus, $m$ can be determined by plotting $\bar{P}_2$ as a function of $\bar{P}_1$ (Figure 4.1(B)). So long as only one order of absorption contributes to the observed signal, $m$ will correspond to the order of that process, as will the slope of a logarithmic plot, $n$.

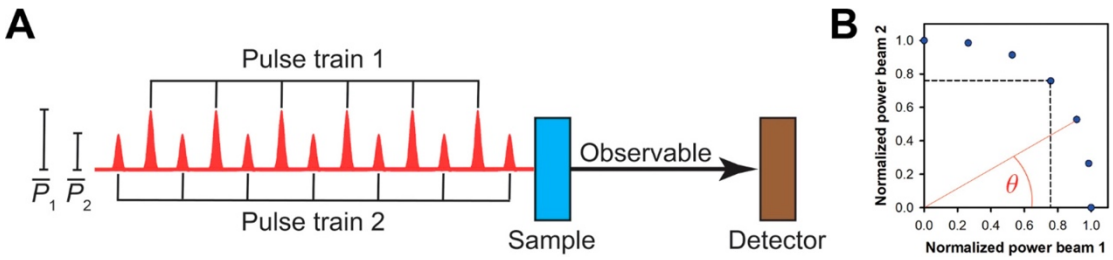


**Figure 4.1** (A) Schematic depiction of two-beam action spectroscopy. Two temporally interleaved pulse trains with average powers $\bar{P}_1$ and $\bar{P}_2$ are incident on a sample, generating an observable via linear and/or nonlinear absorption. (B) Sets of values of $\bar{P}_1$ and $\bar{P}_2$ that lead to the same value of the observable are determined, and $\bar{P}_2$ is plotted as a function of $\bar{P}_1$ to determine the order(s) of absorption. The dashed lines denote $\bar{P}_{\text{diag}}$. $\theta$ is the angle that a line from the origin to a data point makes with the $x$ axis.

Now imagine that two different orders of absorption, $j$ and $k$, where $j < k$, contribute to the observed signal. We will refer to this set of exponents henceforth as ($j$,$k$). In this situation the signal $S$ will be given by

$$S(I) \propto AI^j + BI^k\,, \tag{4.2}$$

where $I$ is the irradiance and $A$ and $B$ are constants that depend on factors such as the absorption cross sections of the different orders, the temporal shape of the laser pulses, and the quantum yield for the observable.[33] It should be noted that $j$- and $k$-photon transitions using the same source wavelengths typically excite different states. In a

traditional measurement, the slope of a logarithmic plot of the signal as a function of irradiance at a given irradiance $I$ will then be given by

$$n = \frac{d\ln(S)}{d\ln(I)} = j + \Delta j \frac{BI^k}{AI^j + BI^k} \ , \tag{4.3}$$

where $\Delta j = k - j$.

It should be noted that a given value of $n$ could arise from any ($j$,$k$). The only way to identify these orders via a logarithmic plot is to collect data over a sufficient range of irradiance. However, the range of irradiance $\Delta I$ required to have the signal arise 90% from order $j$ to 90% from order $k$ is[54]

$$\Delta I = 81^{1/\Delta j}. \tag{4.4}$$

Thus, unless $\Delta j$ is large, it is essential to cover an order of magnitude or more in irradiance to be able to determine the orders of the absorption processes from a logarithmic plot.

In the case of 2-BA spectroscopy, the combination of two different orders of absorption leads to a plot that follows

$$a\left(\bar{P}_1^j + \bar{P}_2^j\right) + b\left(\bar{P}_1^k + \bar{P}_2^k\right) = 1 \ , \tag{4.5}$$

where $a + b = 1$. This expression can be rearranged to give[54]

$$1 - \bar{P}_1^k - \bar{P}_2^k = a\left(\bar{P}_1^j + \bar{P}_2^j - \bar{P}_1^k - \bar{P}_2^k\right) . \tag{4.6}$$

This linearized equation can be used to determine $a$, and therefore $b$, at a single value

of the observable. However, values of $a$ and $b$ can in principle be found for any ($j$,$k$).

We can interpret $a$ as being the fraction of the absorption arising from order $j$, which implies that

$$a = \frac{AI^j}{AI^j + BI^k} . \tag{4.7}$$

By the same token,

$$b = \frac{BI^k}{AI^j + BI^k} . \tag{4.8}$$

The ratio of the observable arising from order k to that arising from order j is therefore

$$\frac{b}{a} = \frac{BI^k}{AI^j} = \frac{B}{A} I^{\Delta j} . \tag{4.9}$$

Thus, if $j$ and $k$ have been chosen correctly, a plot of $b/a$ as a function of $I^{\Delta j}$ will be linear with a slope of $B/A$ and will pass through the origin.[54] However, this approach requires that $a$ be able to be determined over a sufficient range of irradiance values.

## 4.3 *Results and Discussion*

We first consider the diagonal of a 2-BA plot, for which $\bar{P}_1 = \bar{P}_2 = \bar{P}_{diag}$ (Figure 4.1(B)). The simplest manner of determining the 2-BA exponent $m$, which we will call the three-point method, is to measure the values of $\bar{P}_1$ and $\bar{P}_2$ when only one beam is used and then to measure $\bar{P}_{diag}$. It follows from Eq. (4.1) that

$$\bar{P}_{diag}^m = \frac{1}{2} . \tag{4.10}$$

and therefore

$$m = \frac{\ln(1/2)}{\ln(\bar{P}_{diag})}. \tag{4.11}$$

In general, it is preferable to use more than three data points to determine *m*, although if the exponent is known to be an integer then the three-point method should generally be sufficient. This strategy can be considered as a variation of one developed by Wegener and co-workers to measure the effective order of nonlinear absorption in multiphoton absorption polymerization.[39]

When two orders of absorption contribute to the signal, Eq. (4.5) leads to the relation

$$\bar{P}_{diag}^{k} + a\left(\bar{P}_{diag}^{j} - \bar{P}_{diag}^{k}\right) = \frac{1}{2}. \tag{4.12}$$

Combining Eq. (4.10) and Eq. (4.12), we find that

$$a = \frac{\bar{P}_{diag}^{m} - \bar{P}_{diag}^{k}}{\bar{P}_{diag}^{j} - \bar{P}_{diag}^{k}}. \tag{4.13}$$

Similarly,

$$b = \frac{\bar{P}_{diag}^{j} - \bar{P}_{diag}^{m}}{\bar{P}_{diag}^{j} - \bar{P}_{diag}^{k}}. \tag{4.14}$$

Thus, by determining *m* along the diagonal it is possible to find the values of *a* and *b* for a specific (*j*,*k*). By the same token, if *a*, *j*, and *k* are known, then *m* can be found using the relation

$$m = \frac{\ln\left[\bar{P}^{k}_{diag} + a\left(\bar{P}^{j}_{diag} - \bar{P}^{k}_{diag}\right)\right]}{\ln\left(\bar{P}_{diag}\right)} . \tag{4.15}$$

Furthermore, Eqs. (4.3), (4.8), (4.10), and (4.14) can be combined to give an expression that allows the slope *n* of a logarithmic plot to be calculated from the 2-BA exponent *m* measured along the diagonal:

$$n = j + \Delta j \frac{1 - 2^{-(m-j)/m}}{1 - 2^{-\Delta j/m}} . \tag{4.16}$$

In Figure 4.2 we show the dependence of *n* on *m* for the six different (*j*,*k*) examined here. The general behavior that is observed in all cases is that $n < m$ for values below *j* and above *k*, whereas $n > m$ for values between *j* and *k*. When the exponent is either *j* or *k*, then $n = m$. For values above *k*, the dependence of *n* on *m* is roughly linear. Unfortunately, Eq. (4.16) cannot be inverted to find an expression for *m* as a function of *n*. However, as shown below, specific expressions exist for *m* as a function of *n* for any given (*j*,*k*).

Although the above strategy allows for the determination of *a* from the value of *m* measured along the diagonal, this method offers no direct means of determining what the correct (*j*,*k*) might be. Furthermore, if *a* and *b* are not zero, then in general the only places that data points for a specific value of *m* will be equal to data points for a combination of two explicit orders of absorption will be along the axes and on the diagonal. However, the deviation of a plot for a single, noninteger exponent m from a plot for an explicit (*j*,*k*) can provide a substantial amount of information about the true values of *j* and *k*.

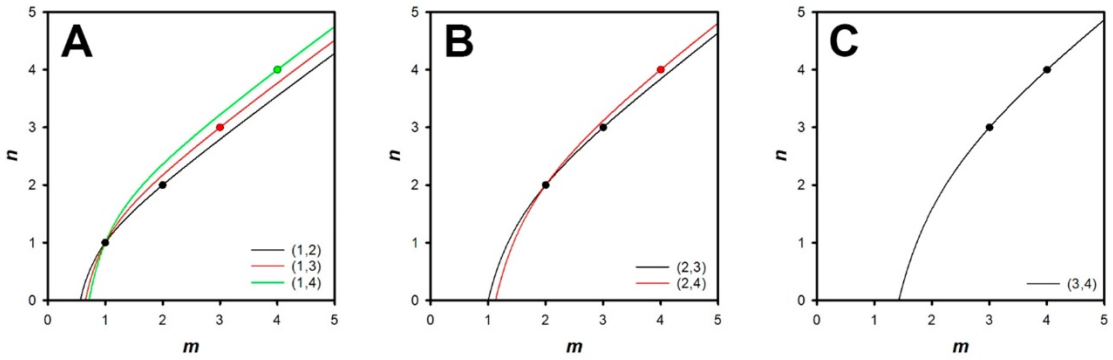


**Figure 4.2** Plots of the logarithmic plot exponent $n$ as a function of the 2-BA exponent $m$ for six different ($j$,$k$): (A) sets for $j$ = 1; (B) sets for $j$ = 2; (C) the set for $j$ = 3. The symbols indicate the points at which $n = m$, which occurs when only a single absorption process is present.

The simplest manner of measuring the deviation between two different 2-BA plots is to determine the radial distance between points that are at the same angle $\theta$ from the $x$ axis (see Figure 4.1(B)). In the case of a plot for a single exponent $m$, the slope $s$ of a line from the origin to a data point at angle $\theta$ is given by

$$s = \tan\theta = \frac{\bar{P}_2}{\bar{P}_1} . \tag{4.17}$$

Accordingly,

$$\bar{P}_2(\theta) = s\bar{P}_1(\theta) . \tag{4.18}$$

Plugging this result into Eq. (4.1) leads to

$$\bar{P}_1(\theta) = \left(\frac{1}{1+s^m}\right)^{1/m} . \tag{4.19}$$

To find the coordinates of a data point at angle $\theta$ when there are contributions from two exponents, we begin by rewriting Eq. (4.5) as

$$\left(\bar{P}_1^k + \bar{P}_2^k\right) + \frac{a}{1-a}\left(\bar{P}_1^j + \bar{P}_2^j\right) - \frac{1}{1-a} = 0\,. \tag{4.20}$$

Combining this result with Eq. (4.18), we find that

$$\bar{P}_1^k(\theta) + \frac{a\left(1+s^j\right)}{(1-a)\left(1+s^k\right)}\bar{P}_1^j(\theta) - \frac{1}{(1-a)\left(1+s^k\right)} = 0\,. \tag{4.21}$$

The *x* coordinate can be determined by finding the appropriate root of this polynomial, with the *y* coordinate then following from Eq. (4.18).

First, we consider the case in which $j = 1$ and $k = 2$. The polynomial for which we must find the root is

$$\bar{P}_1^2(\theta) + \frac{a(1+s)}{(1-a)(1+s^2)}\bar{P}_1(\theta) - \frac{1}{(1-a)(1+s^2)} = 0\,. \tag{4.22}$$

The relevant root of this equation is

$$\bar{P}_1(\theta) = \frac{-a(1+s)+\sqrt{a^2(1+s)^2+4(1-a)(1+s^2)}}{2(1-a)(1+s^2)}\,. \tag{4.23}$$

Along the diagonal this equation becomes

$$\bar{P}_{diag}(\theta) = \frac{-a+\sqrt{a^2-2a+2}}{2(1-a)}\,. \tag{4.24}$$

Equations (4.3) and (4.8) imply that

$$a = \frac{k-n}{\Delta j}\,. \tag{4.25}$$

Plugging this result into Eq. (4.24) and then using Eq. (4.11), we find that

$$m = \ln(1/2)/\ln\left(\frac{n-2+\sqrt{n^2-2n+2}}{2(n-1)}\right). \quad (4.26)$$

Thus, we are able to use this approach to determine *m* from *n* for this particular (*j*,*k*).

The problem of determining *m* as a function of *n* reduces to finding $\bar{P}_{diag}$ as a function of *n* for the different (*j*,*k*). In general we may need to use different roots to determine $\bar{P}_{diag}$ depending on the value of *a* (and therefore the value of *n*). The results of corresponding analyses for the other five possible (*j*,*k*) with individual exponents ranging from 1 to 4 are given below.

***A. (1,3)***

The polynomial for which we must find the root for (1,3) is

$$\bar{P}_1^3(\theta) + A_{(1,3)}\bar{P}_1(\theta) - B_{(1,3)} = 0\ . \quad (4.27)$$

where

$$A_{(1,3)} = \frac{a(1+s)}{(1-a)(1+s^3)} \quad (4.28)$$

and

$$B_{(1,3)} = \frac{1}{(1-a)(1+s^3)}\ . \quad (4.29)$$

Along the diagonal we have

$$A_{(1,3),diag} = \frac{3-n}{n-1} \quad (4.30)$$

and

$$B_{(1,3),diag} = \frac{1}{n-1}\,. \tag{4.31}$$

When $a \leq 1$ ($n > 1$), the relevant root of this equation is

$$\bar{P}_1(\theta) = \sqrt[3]{\frac{B_{(1,3)}}{2} + \sqrt{\frac{A_{(1,3)}^3}{27} + \frac{B_{(1,3)}^2}{4}}} - \frac{A_{(1,3)}}{3}\left(\sqrt[3]{\frac{B_{(1,3)}}{2} + \sqrt{\frac{A_{(1,3)}^3}{27} + \frac{B_{(1,3)}^2}{4}}}\right)^{-1} \tag{4.32}$$

When $a > 1$ ($n < 1$) we must use a different root of Eq. (4.28):

$$\bar{P}_1(\theta) = \left|\sqrt{-\frac{A_{(1,3)}}{3}}\right|\left(X_{(1,3)} + \sqrt{3}Y_{(1,3)}\right), \tag{4.33}$$

where

$$X_{(1,3)} = cos\left(\frac{1}{3}tan^{-1}\left(\frac{2}{B_{(1,3)}}\sqrt{-\frac{A_{(1,3)}^3}{27} - \frac{B_{(1,3)}^2}{4}}\right)\right) \tag{4.34}$$

and

$$Y_{(1,3)} = sin\left(\frac{1}{3}tan^{-1}\left(\frac{2}{B_{(1,3)}}\sqrt{-\frac{A_{(1,3)}^3}{27} - \frac{B_{(1,3)}^2}{4}}\right)\right). \tag{4.35}$$

$\bar{P}_{diag}$ is found by plugging Eqs. (4.31) and (4.42) into the appropriate root of Eq. (4.28).

***B. (1,4)***

The polynomial for which we must find the root in this case is

$$\bar{P}_1^4(\theta) + A_{(1,4)}\bar{P}_1(\theta) - B_{(1,4)} = 0\ . \tag{4.36}$$

where

$$A_{(1,4)} = \frac{a(1+s)}{(1-a)(1+s^4)} \tag{4.37}$$

and

$$B_{(1,4)} = \frac{1}{(1-a)(1+s^4)}\ . \tag{4.38}$$

Along the diagonal these become

$$A_{(1,4),diag} = \frac{4-n}{n-1} \tag{4.39}$$

and

$$B_{(1,4),diag} = \frac{3}{2(n-1)}\ . \tag{4.40}$$

We define

$$X_{(1,4)} = \frac{\sqrt[3]{\sqrt{3}\sqrt{27A_{(1,4)}^4 + 256B_{(1,4)}^3} + 9A_{(1,4)}^2}}{\sqrt[3]{18}} - \frac{4B_{(1,4)}\sqrt[3]{2/3}}{\sqrt[3]{\sqrt{3}\sqrt{27A_{(1,4)}^4 + 256B_{(1,4)}^3} + 9A_{(1,4)}^2}} \tag{4.41}$$

When $0 \leq a \leq 1$ ($4 \geq n \geq 1$) the relevant root of Eq. (4.36) is

$$\bar{P}_1(\theta) = -\frac{1}{2}\sqrt{X_{(1,4)}} + \frac{1}{2}\sqrt{\frac{2A_{(1,4)}}{\sqrt{X_{(1,4)}}} - X_{(1,4)}}\,. \tag{4.42}$$

When $a < 0$ ($n > 4$) the relevant root of Eq. (4.36) is

$$\bar{P}_1(\theta) = \frac{1}{2}\sqrt{X_{(1,4)}} + \frac{1}{2}\sqrt{-\frac{2A_{(1,4)}}{\sqrt{X_{(1,4)}}} - X_{(1,4)}}\,. \tag{4.43}$$

When $a > 1$ ($n < 1$) the relevant root of Eq. (4.36) is

$$\bar{P}_1(\theta) = \frac{1}{2}\sqrt{X_{(1,4)}} - \frac{1}{2}\sqrt{-\frac{2A_{(1,4)}}{\sqrt{X_{(1,4)}}} - X_{(1,4)}}\,. \tag{4.44}$$

***C. (2,3)***

The polynomial for which we must find the root in this case is

$$\bar{P}_1^3(\theta) + A_{(2,3)}\bar{P}_1^2(\theta) - B_{(2,3)} = 0\,. \tag{4.45}$$

where

$$A_{(2,3)} = \frac{a(1+s^2)}{(1-a)(1+s^3)} \tag{4.46}$$

and

$$B_{(2,3)} = \frac{1}{(1-a)(1+s^3)}\,. \tag{4.47}$$

Along the diagonal these become

$$A_{(2,3),diag} = \frac{3-n}{n-2} \tag{4.48}$$

and

$$B_{(2,3),diag} = \frac{1}{2(n-2)}\,. \tag{4.49}$$

We define

$$X_{(2,3)} = \sqrt[3]{\frac{B_{(2,3)}}{2} - \frac{A_{(2,3)}^3}{27} + \sqrt{\frac{B_{(2,3)}^2}{4} - \frac{A_{(2,3)}^3 B_{(2,3)}}{27}}} \tag{4.50}$$

When $a \leq 0.6882$ ($n \geq 2.31118$) the relevant root of Eq. (4.45) along the diagonal is

$$\bar{P}_1(\theta) = X_{(2,3)} + \frac{A_{(2,3)}^2}{9Z_{(2,3)}} - \frac{A_{(2,3)}}{3}\,. \tag{4.51}$$

The upper bound for $a$ corresponds to the value at which the expression in the square root in Eq. (4.50) becomes zero. When $0.6882 < a \leq 0.75$ ($2.31118 \geq n \geq 2.25$) the relevant root of Eq. (4.45) is

$$\bar{P}_1(\theta) = \frac{1}{2}A_{(2,3)}\left(2Y_{(2,3)} - 1\right), \tag{4.52}$$

where

$$Y_{(2,3)} = cos\left(\frac{1}{3}tan^{-1}\left(\frac{\sqrt{-\frac{B_{(2,3)}^2}{4}+\frac{A_{(2,3)}^3 B_{(2,3)}}{27}}}{\frac{B_{(2,3)}}{2}-\frac{A_{(2,3)}^3}{27}}\right)\right). \tag{4.53}$$

The upper bound for $a$ corresponds to when the term that is not in the square root in Eq. (4.50) becomes zero. When $0.75 < a < 3$ ($2.25 > n > 0$) the relevant root of Eq. (4.45) is

$$\bar{P}_1(\theta) = -\frac{1}{2}A_{(2,3)}\left(2Z_{(2,3)} + 1\right), \tag{4.54}$$

where

$$Z_{(2,3)} = cos\left(\frac{1}{3}tan^{-1}\left(\frac{\sqrt{-\frac{B_{(2,3)}^2}{4}+\frac{A_{(2,3)}^3 B_{(2,3)}}{27}}}{\frac{B_{(2,3)}}{2}-\frac{A_{(2,3)}^3}{27}}\right)-\frac{2\pi}{3}\right). \tag{4.55}$$

***D. (2,4)***

The polynomial for which we must find the root in this case is

$$\bar{P}_1^4(\theta) + A_{(2,4)}\bar{P}_1^2(\theta) - B_{(2,4)} = 0\,. \tag{4.56}$$

where

$$A_{(2,4)} = \frac{a\left(1+s^2\right)}{(1-a)(1+s^4)} \tag{4.57}$$

and

$$B_{(2,4)} = \frac{1}{(1-a)(1+s^4)} . \tag{4.58}$$

Along the diagonal these become

$$A_{(2,4),diag} = \frac{4-n}{n-2} \tag{4.59}$$

and

$$B_{(2,4),diag} = \frac{1}{n-2} . \tag{4.60}$$

When $a \leq 1$ ($n \geq 2$) the relevant root of Eq. (4.56) along the diagonal is

$$\bar{P}_1(\theta) = \sqrt{\frac{1}{2}\left(\sqrt{A_{(2,4)}^2 + 4B_{(2,4)}} - A_{(2,4)}\right)} . \tag{4.61}$$

When $a > 1$ ($n < 2$) the relevant root of Eq. (4.56) along the diagonal is

$$\bar{P}_1(\theta) = \sqrt{\frac{1}{2}\left(-\sqrt{A_{(2,4)}^2 + 4B_{(2,4)}} - A_{(2,4)}\right)} . \tag{4.62}$$

***E. (3,4)***

The polynomial for which we must find the root in this case is

$$\bar{P}_1^4(\theta) + A_{(3,4)}\bar{P}_1^3(\theta) - B_{(3,4)} = 0 . \tag{4.63}$$

where

$$A_{(3,4)} = \frac{a\left(1+s^3\right)}{(1-a)(1+s^4)} \tag{4.64}$$

and

$$B_{(3,4)} = \frac{1}{(1-a)(1+s^4)}\,. \tag{4.65}$$

Along the diagonal these become

$$A_{(3,4),diag} = \frac{4-n}{n-3} \tag{4.66}$$

and

$$B_{(3,4),diag} = \frac{1}{2(n-3)}\,. \tag{4.67}$$

We define

$$X_{(3,4)} = \sqrt[3]{\sqrt{3}\sqrt{27A_{(3,4)}^4 B_{(3,4)}^2 + 256B_{(3,4)}^3} - 9A_{(3,4)}^2 B_{(3,4)}} \tag{4.68}$$

and

$$Y_{(3,4)} = \frac{A_{(3,4)}^2}{4} + \frac{X_{(3,4)}}{\sqrt[3]{18}} - \frac{4\sqrt[3]{2/3}B_{(3,4)}}{X_{(3,4)}}\,. \tag{4.69}$$

When $0 < a < 1$ ($4 > n > 3$) the relevant root of Eq. (4.63) along the diagonal is

$$\bar{P}_1(\theta) = -\frac{A_{(3,4)}}{4} - \frac{1}{2}\sqrt{Y_{(3,4)}} + \frac{1}{2}\sqrt{\frac{3A_{(3,4)}^2}{4} - Y_{(3,4)} + \frac{A_{(3,4)}^3}{4\sqrt{Y_{(3,4)}}}}\,. \tag{4.70}$$

When $a < 0$ ($n > 4$) the relevant root of Eq. (4.63) along the diagonal is

$$\bar{P}_1(\theta) = -\frac{A_{(3,4)}}{4} + \frac{1}{2}\sqrt{Y_{(3,4)}} + \frac{1}{2}\sqrt{\frac{3A_{(3,4)}^2}{4} - Y_{(3,4)} - \frac{A_{(3,4)}^3}{4\sqrt{Y_{(3,4)}}}}\,. \tag{4.71}$$

When $a > 1$ ($n < 3$) the relevant root of Eq. (4.63) along the diagonal is

$$\bar{P}_1(\theta) = -\frac{A_{(3,4)}}{4} + \frac{1}{2}\sqrt{Y_{(3,4)}} - \frac{1}{2}\sqrt{\frac{3A_{(3,4)}^2}{4} - Y_{(3,4)} - \frac{A_{(3,4)}^3}{4\sqrt{Y_{(3,4)}}}}\,. \tag{4.72}$$

In Figure 4.3(A) we plot the difference between the (1,2) curve (from Eq. (4.5)) and the single-effective-exponent curve (from Eq. (4.1)) as a function of $\theta$ for values of $a$ ranging from 0.1 to 0.9. The difference is symmetric about the diagonal because the two beams are interchangeable. In all cases the deviation is negative, i.e., the plot with a single effective exponential extends a greater distance from the origin than the actual plot, except on the axes and on the diagonal. When $a$ is close to 0 or 1, there is only a small contribution from one exponent, and the deviations are relatively small. The largest deviations are observed when $a = 0.5$. In all cases, the largest deviation is observed at an angle that lies in the range from roughly 5° to 15°. The larger the value of $a$, the smaller the angle at which the largest deviation is observed.

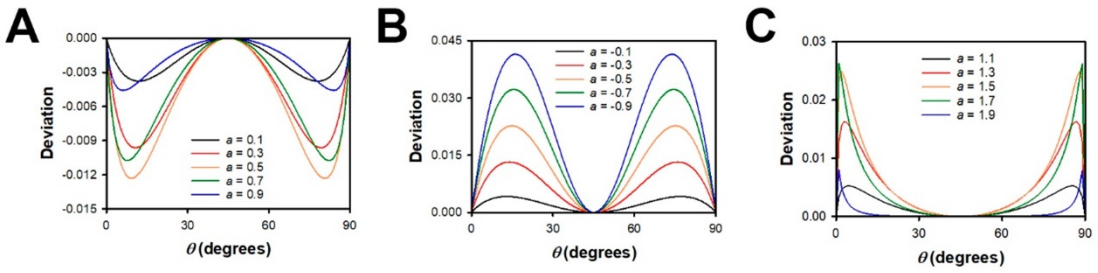


**Figure 4.3** Difference between Eq. (4.5) and Eq. (4.1) with *m* determined along the diagonal for a combination of linear and quadratic components as a function of the amplitude of the linear component, *a*. The panels show results for *a* values in the ranges (A) 0.1 to 0.9, (B) -0.1 to -0.9, and (C) 1.1 to 1.9.

Although in most circumstances the contributions of two different orders of absorption are expected to be additive, it is also possible for them to be of opposite sign. One example of this situation would be a system in which linear absorption generates fluorescence but two-photon absorption populates a dark state. We should therefore also consider values of *a* that are less than zero or greater than 1. We investigate the former case in Figure 4.3(B) for values of a ranging from -0.1 to -0.9. In this case the deviation is positive and grows in magnitude as |a| increases. The angle of maximum deviation also increases as |*a*| increases.

In Figure 4.3(C) we plot the deviation for values of *a* ranging from 1.1 to 1.9. We note that when $a > 1$ the quantity $1-a$ is negative, and so the other root of Eq. (4.22) (with a negative sign before the square root) is used. This range of *a* was chosen because the slope of a logarithmic plot is 0 when $a = 2$ (see Eq. (4.25)). In this case the deviation is also positive. The maximum deviation grows with increasing *a* but becomes smaller again as *a* approaches 2. The angle at which the maximum deviation occurs also decreases with increasing *a*.

Plots corresponding to Figure 4.3 for the other five pairs of combinations of exponents from 1 to 4 are given in Figures 4.4-4.8. The same general trends are

observed for these other sets of exponents. The deviations are negative for $0 < a < 1$, and are generally positive for $a < 0$ and $a > 1$, although for large enough values of $a$ the deviations can become negative. The angle at which the maximum deviation occurs shifts in the same manner as $a$ is varied, but for fixed $a$ the angle at which the largest deviation occurs generally becomes larger as the exponents become larger. The magnitudes of the deviations are also dependent upon $(j,k)$.

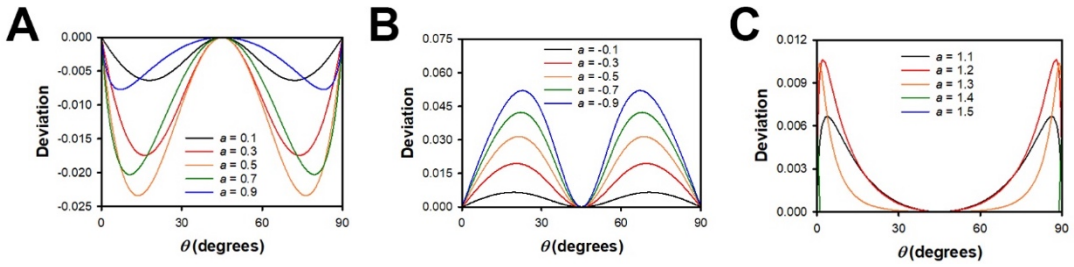


**Figure 4.4** The difference between Eq. (4.5) and Eq. (4.1) with $m$ determined along the diagonal for (1,3) as a function of the amplitude of the linear component, $a$. The panels show results for $a$ values ranging from (A) 0.1 to 0.9; (B) -0.1 to -0.9; and (C) 1.1 to 1.5.

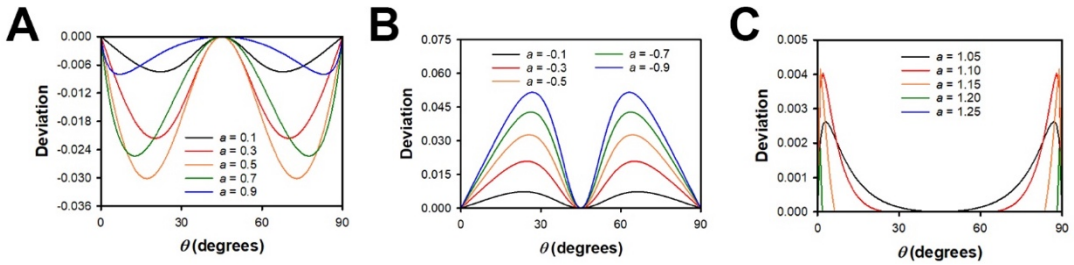


**Figure 4.5** The difference between Eq. (4.5) and Eq. (4.1) with $m$ determined along the diagonal for (1,4) as a function of the amplitude of the linear component, $a$. The panels show results for $a$ values ranging from (A) 0.1 to 0.9; (B) -0.1 to -0.9; and (C) 1.1 to 1.25.

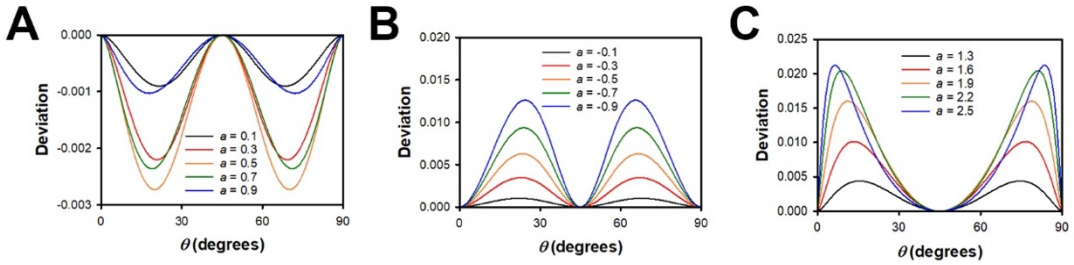


**Figure 4.6** The difference between Eq. (4.5) and Eq. (4.1) with $m$ determined along the diagonal for (2,3) as a function of the amplitude of the quadratic component, $a$. The panels show results for $a$ values ranging from (A) 0.1 to 0.9; (B) -0.1 to -0.9; and (C) 1.1 to 1.25.

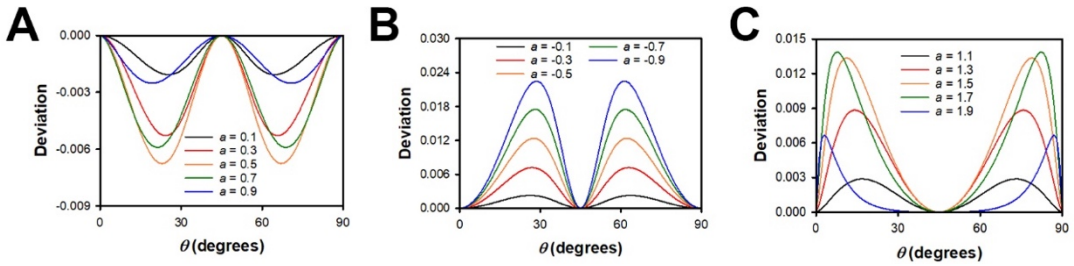


**Figure 4.7** The difference between Eq. (4.5) and Eq. (4.1) with $m$ determined along the diagonal for (2,4) as a function of the amplitude of the quadratic component, $a$. The panels show results for $a$ values ranging from (A) 0.1 to 0.9; (B) -0.1 to -0.9; and (C) 1.1 to 1.25.

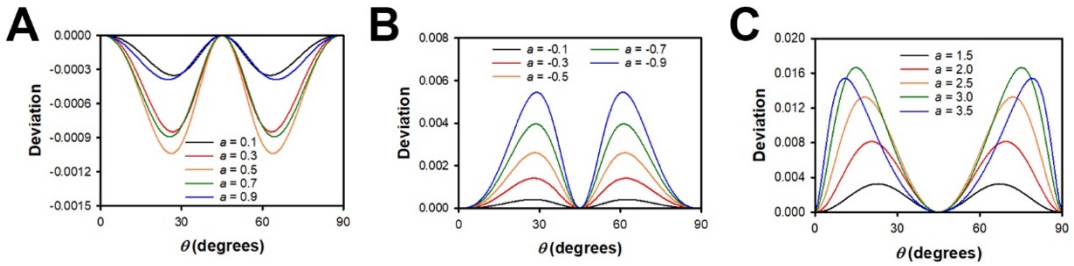


**Figure 4.8** The difference between Eq. (4.5) and Eq. (4.1) with $m$ determined along the diagonal for (3,4) as a function of the amplitude of the cubic component, $a$. The panels show results for $a$ values ranging from (A) 0.1 to 0.9; (B) -0.1 to -0.9; and (C) 1.1 to 1.25.

It is also useful to consider how the deviations for a fixed value of $m$ depend on $(j,k)$. As a representative case, in Figure 4.9 we plot the deviations for $m = 2.5$ for the six different $(j,k)$. Two general trends are apparent in this plot. First, the deviations are positive when $j$ and $k$ are both less than $m$ or both greater than $m$, and are negative when $m$ is between $j$ and $k$. Second, for deviations of the same sign, the magnitude of the deviation grows with the ratio $k/j$.

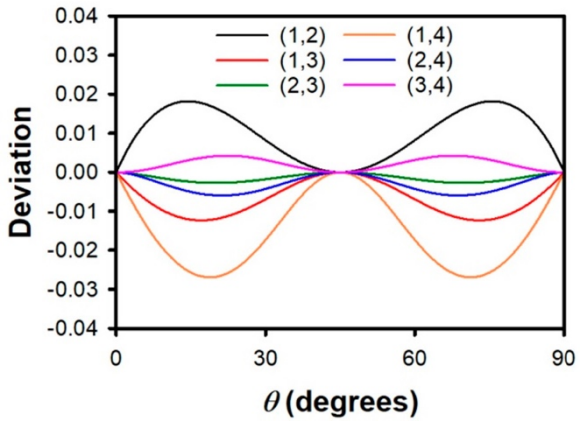


**Figure 4.9** Difference between Eq. (4.5) and Eq. (4.1) for $m = 2.5$ for each of the different $(j,k)$ examined.

As discussed above, 2-BA spectroscopy data can generally be fit to Eq. (4.6) for multiple $(j,k)$. The correct values of $j$ and $k$ can be determined by determining $a$ and $b$ for different values of $m$ and finding which set of exponents is consistent with Eq. (4.9). However, it is worthwhile to consider whether there are conditions under which $(j,k)$ can be determined from data obtained for a single value of $m$ and what data would be required to make such a determination. Making a measurement for a single value of $m$ requires fewer experiments than making measurements for multiple values. Furthermore, in the case of processes with thresholds, such as photopolymerization, it is not possible to make measurements at different values of $m$.

As a representative example, we consider the case in which $m = 2.1$. In Figure 4.10 we plot Eq. (4.6) for data corresponding to (1,2). The data points are color-coded based on their angles relative to the $x$ axis in a 2-BA plot. Given any significant experimental uncertainty, the data could also be fit well to (2,3), (2,4), and (3,4). Equivalent plots for (1,3) and (2,3) are shown in Figures 4.11 and 4.12, respectively. In the former case, any combination other than (1,2) might reasonably fit the plots given a noise level that is typical experimentally. In the latter case, (1,3) could likely be ruled

out as well. Plots for the other three combinations of $j$ and $k$ for $m$ = 2.1 are given in Figures 4.13-4.15.

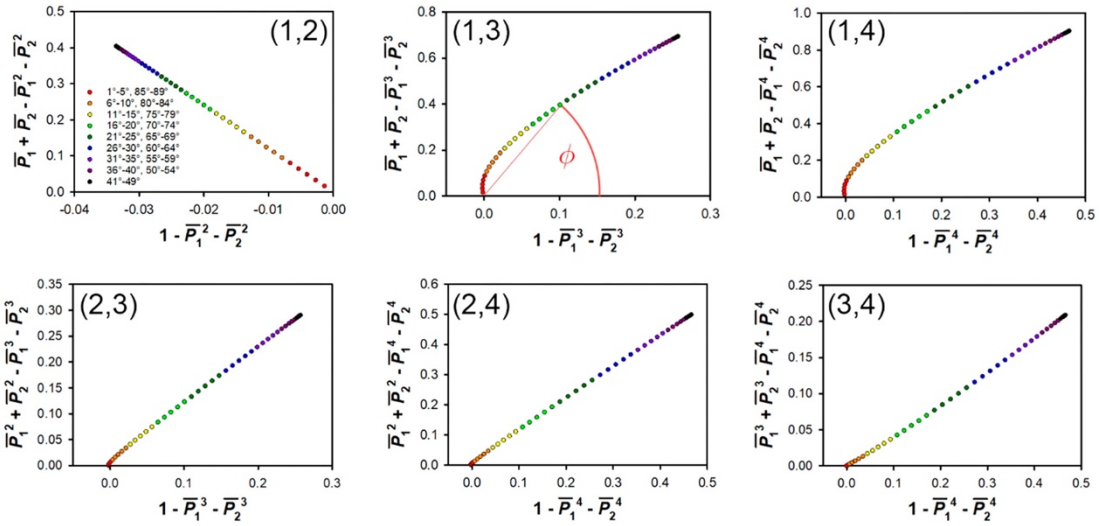


**Figure 4.10** Plots of Eq. (4.6) using different ($j$,$k$) for data generated using (1,2) and $m$ = 2.1. The data points are color-coded on the basis of their angles $\theta$ relative to the $x$ axis in a 2-BA plot (see the legend). $\varphi$ is the angle a line from the origin to a data point makes with the $x$ axis.

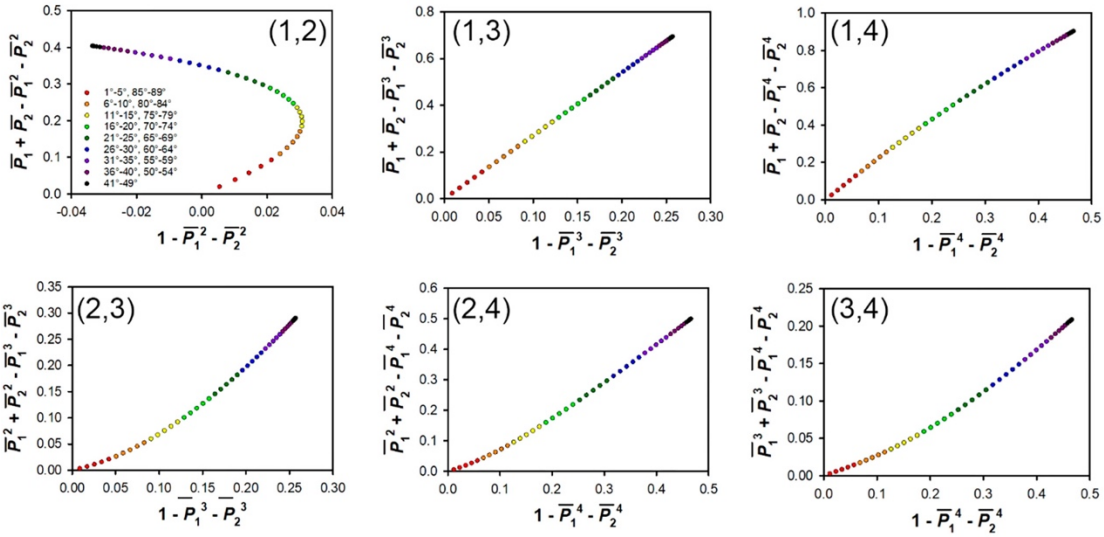


**Figure 4.11** Plots of Eq. (4.6) using different ($j$,$k$) for data generated using (1,3) and $m$ = 2.1. The data points are color-coded on the basis of their angles $\theta$ relative to the $x$ axis in a 2-BA plot (see the legend).

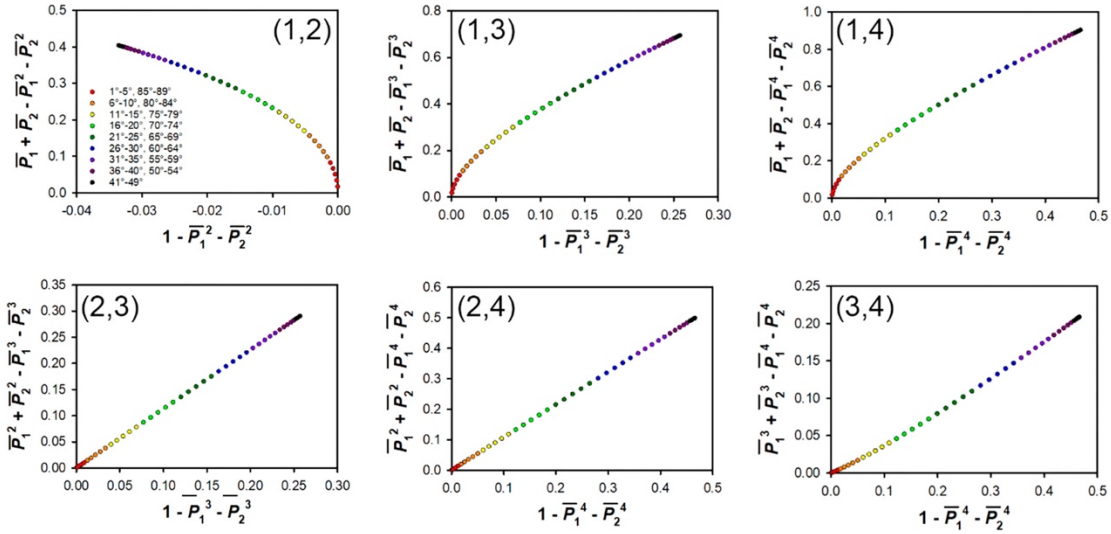


**Figure 4.12** Plots of Eq. (4.6) using different ($j$,$k$) for data generated using (2,3) and $m$ = 2.1. The data points are color-coded on the basis of their angles $\theta$ relative to the $x$ axis in a 2-BA plot (see the legend).

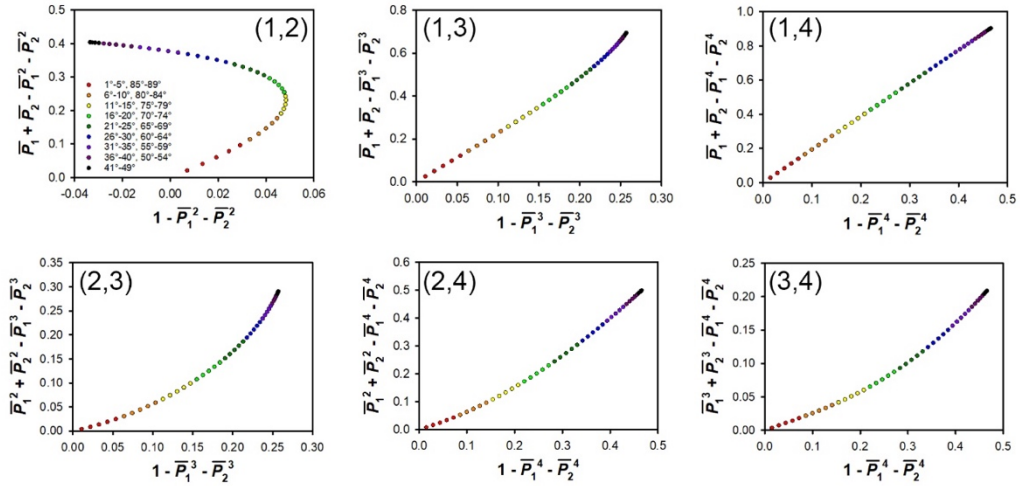


**Figure 4.13** Plots of Eq. (4.6) using different ($j$,$k$) for data generated using (1,4) and $m$ = 2.1. The data points are color-coded on the basis of their angles $\theta$ relative to the $x$ axis in a 2-BA plot (see the legend).

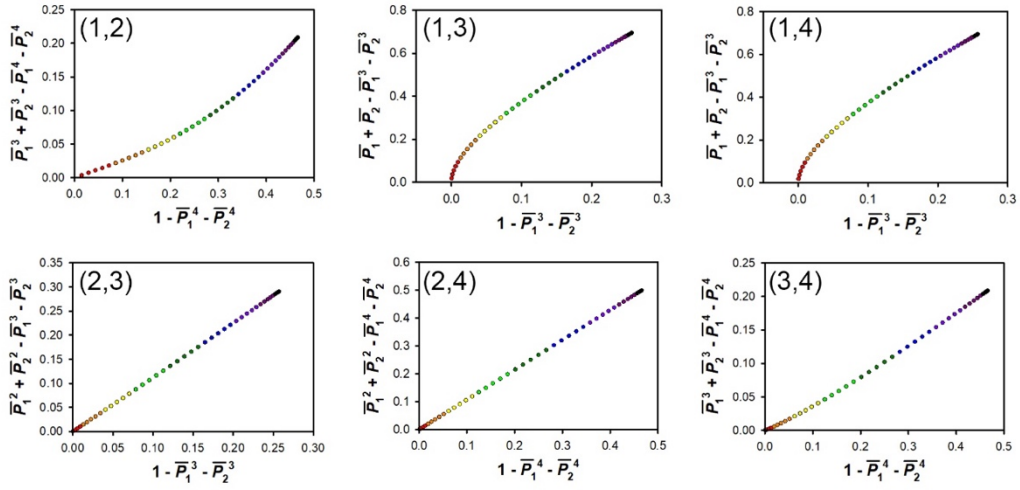


**Figure 4.14** Plots of Eq. (4.6) using different ($j$,$k$) for data generated using (2,4) and $m$ = 2.1. The data points are color-coded on the basis of their angles $\theta$ relative to the $x$ axis in a 2-BA plot (see the legend).

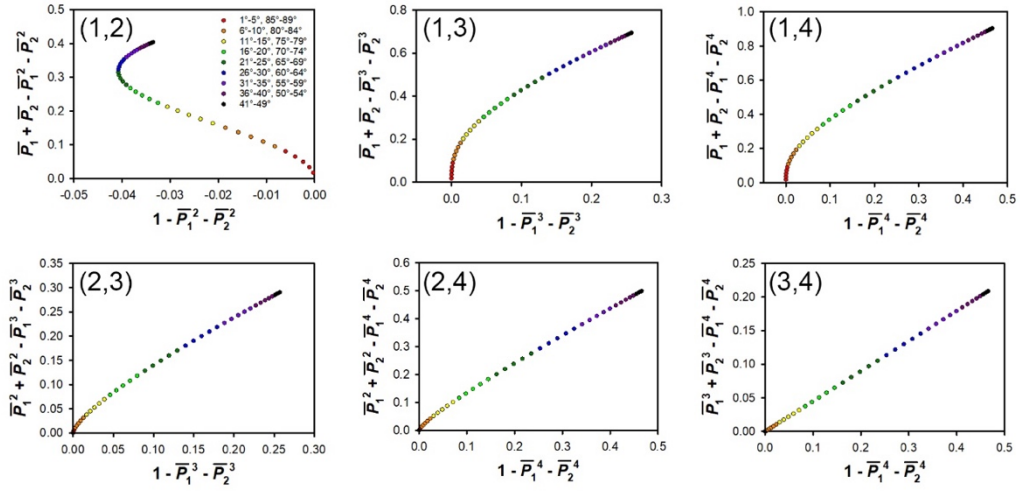


**Figure 4.15** Plots of Eq. (4.6) using different ($j$,$k$) for data generated using (3,4) and $m$ = 2.1. The data points are color-coded on the basis of their angles $\theta$ relative to the $x$ axis in a 2-BA plot (see the legend).

Although the plots of Eq. (4.6) for the specific ($j$,$k$) of interest do not always yield a clear sense of the appropriate sets of exponents, it should be noted that plots for other sets of exponents can be quite revealing. For instance, in the (2,3) case, the data points for plots for (1,2) are entirely in the second quadrant. However, in the (1,3) case, the data points for plots for (1,2) are in the first and second quadrants. Thus, even when a plot for a given $j$ and $k$ ends up not to be linear, it can still give insight into the actual

values of ($j$,$k$). When $m$ is not an integer, it is therefore generally useful to make plots of Eq. (4.6) for all six ($j$,$k$) explored here, even when not all of these ($j$,$k$) are physically plausible.

An additional approach that can be used to analyze 2-BA data that have a noninteger $m$ is to plot the angles that the data points in Eq. (4.6) make with the $x$ axis ($\varphi$) as a function of the angle $\theta$ derived from the 2-BA plot (see Figure 4.10). Such plots can complement plots of Eq. (4.6), giving insight into which orders of absorption contribute to the signal in 2-BA spectroscopies. In many cases such plots in conjunction with plots of Eq. (4.6) can lead to an unambiguous determination of two different orders of absorption that contribute to 2-BA spectroscopy data. In Figure 4.16 we show the angular plots corresponding to the plots in Figures 4.10-4.12. In Figure 4.17 we show the angular plots corresponding to the plots in Figures 4.13-4.15. In conjunction with plots of Eq. (4.6), these angular plots provide clear distinctions among different ($j$,$k$) in most cases, with the one exception in this example being that it remains difficult to tell the difference between (2,3) and (2,4).

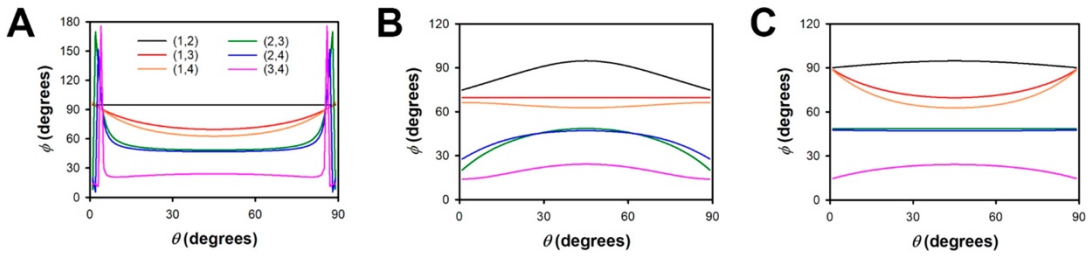


**Figure 4.16** Angle that plots of Eq. (4.6) make with the $x$ axis ($\varphi$) as a function of the 2-BA plot angle $\theta$ for $m$ = 2.1 and different ($j$,$k$) using the data in (A) Figure 4.10, (B) Figure 4.11, and (C) Figure 4.12.

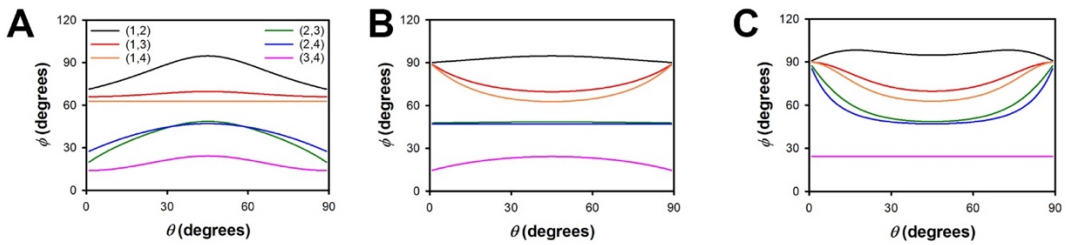


**Figure 4.17** Angle that plots of Eq. (4.6) make with the $x$ axis ($\varphi$) as a function of the 2-BA plot angle $\theta$ for $m$ = 2.1 and different ($j$,$k$) using the data in (A) Figure 4.13, (B) Figure 4.14, and (C) Figure 4.15.

Once a noninteger value of $m$ has been measured along the diagonal in a 2-BA spectroscopy experiment, it is useful to make plots of Eq. (4.6) and the associated angular plots for the different ($j$,$k$) examined here. Such plots will reveal the angles at which 2-BA data will provide that greatest degree of discrimination among different possible ($j$,$k$). The most useful angles for measuring 2-BA data are typically ones at which there is a substantial deviation from linearity observable when incorrect ($j$,$k$) are tested.

## 4.4 *Conclusions*

2-BA spectroscopies are a useful alternative to traditional logarithmic plots for determining the order(s) of absorption that contribute to an experimental observable. A measured exponent that is nonintegral is generally indicative of a signal that is generated by two (or more) orders of absorption. In such situations, logarithmic plots and 2-BA plots yield different effective exponents. We have developed a mathematical description of the relationships between these exponents for six different pairs of absorption orders: (1,2), (1,3), (1,4), (2,3), (2,4), and (3,4).

We have demonstrated previously how 2-BA measurements made at different values of the observable can be used to make an unambiguous determination of which

two orders of absorption contribute to an observable.[54] However, in some circumstances the observable may be single-valued, as in the case of a photopolymerization threshold.[53] Here we have presented general principles for data analysis that, in most cases, can lead to the unambiguous determination of the orders of absorption at a single value of the observable. The crux of this strategy is the fact that 2-BA plots for pairs of contributions differ from "idealized" plots for a single noninteger exponent. The form of this deviation is dependent upon the orders of absorption that contribute to the signal. Furthermore, analyzing 2-BA data assuming pairs of orders of absorption other than the pair that contributes to the signal can provide a characteristic signature of the actual orders of absorption.

Based on the results presented here, we suggest the following approach for analyzing 2-BA data. First, for a given value of the observable, the three-point method should be used to determine the 2-BA exponent m via Eq. (4.11). At this point, the expected shapes of plots of Eq. (4.6) and plots of $\varphi$ as a function of $\theta$ can be determined. These plots will give guidance regarding the range of values of $\theta$ that will be most useful for distinguishing among different plausible ($j$,$k$). Additional 2- BA measurements can then be made in this range.

The ultimate success of this approach depends upon a number of factors. First, as discussed above, in some relatively rare cases this strategy on its own will not allow for distinction between two or three ($j$,$k$). However, practical considerations may still allow the appropriate set to be determined under such circumstances. Second, experimental uncertainty can be a limiting factor in such analysis. The higher the precision and accuracy of the 2-BA data, the better is the ability to distinguish among

different ($j$,$k$). Finally, in some cases a 2-BA signal with a noninteger exponent will not arise from two independent contributions. For instance, the observable may arise from two sequential contributions (e.g., absorption followed by ESA) or more than two contributions. Although the framework developed here does not describe such situations, in practice the inability to describe 2-BA data within this scheme can be taken to be indicative of the need for a more complex model. For noncumulative observables (e.g., fluorescence and photocurrent, as opposed to photopolymerization), one way to test for phenomena such as thermal effects or interpulse ESA is to compare results when the beams are overlapped in space and when they are not overlapped in space. If the data are not the same in these two cases, then additional effects must be considered. We have shown previously how to model the signal in the presence of intrapulse ESA when there is also two-photon or three-photon absorption,[55] and similar approaches can be used for related cases.

## *4.5 References*


1. Bhawalkar, J. D.; He, G. S.; Prasad, P. N. Nonlinear Multiphoton Processes in Organic and Polymeric Materials. *Rep. Prog. Phys.* **1996**, *59*, 1041-1070.
2. He, G. S.; Tan, L. S.; Zheng, Q.; Prasad, P. N. Multiphoton Absorbing Materials: Molecular Designs, Characterizations, and Applications. *Chem. Rev.* **2008**, *108*, 1245-1330.
3. Liaros, N.; Fourkas, J. T. The Characterization of Absorptive Nonlinearities. *Laser Photon. Rev.* **2017**, *11*, 1700106.
4. Rumi, M.; Perry, J. W. Two-Photon Absorption: An Overview of Measurements and Principles. *Adv. Opt. Photonics* **2010**, *2*, 451-518.

5. Frohlich, D.; Sondergeld, M. Experimental Techniques in Two-Photon Spectroscopy. *J. Phys. E: Sci. Instrum.* **1977**, *10*, 761-766.
6. Friedrich, D. M.; McClain, W. M. Two-Photon Molecular Electronic Spectroscopy. *Annu. Rev. Phys. Chem.* **1980**, *31*, 559-577.
7. Birge, R. R. Two-Photon Spectroscopy of Protein-Bound Chromophores. *Acc. Chem. Res.* **1986**, *19*, 138-146.
8. Dai, H. L.; Kung, A. H.; Moore, C. B. Resonant Multi-Photon Dissociation and Mechanism of Excitation for Ethyl Chloride. *Phys. Rev. Lett.* **1979**, *43*, 761-764.
9. Carriles, R.; Schafer, D. N.; Sheetz, K. E.; Field, J. J.; Cisek, R.; Barzda, V.; Sylvester, A. W.; Squier, J. A. Imaging Techniques for Harmonic and Multiphoton Absorption Fluorescence Microscopy. *Rev. Sci. Instrum.* **2009**, *80*, 081101.
10. Denk, W.; Strickler, J.; Webb, W. Two-Photon Laser Scanning Fluorescence Microscopy. *Science* **1990**, 248, 73-76.
11. Diaspro, A.; Robello, M. Two-Photon Excitation of Fluorescence for Three-Dimensional Optical Imaging of Biological Structures. *J. Photochem. Photobiol., B* **2000**, *55*, 1-8.
12. Kirejev, V.; Guldbrand, S.; Borglin, J.; Simonsson, C.; Ericson, M. B. Multiphoton Microscopy - A Powerful Tool in Skin Research and Topical Drug Delivery Science. *J. Drug Delivery Sci. Technol.* **2012**, *22*, 250-259.
13. Schrader, M.; Bahlmann, K.; Hell, S. W. Three-Photon-Excitation Microscopy: Theory, Experiment and Applications. *Optik* **1997**, *104*, 116-124.

14. So, P. T. C.; Dong, C. Y.; Masters, B. R.; Berland, K. M. Two-Photon Excitation Fluorescence Microscopy. *Annu. Rev. Biomed. Eng.* **2000**, *2*, 399-429.

15. Wang, B. G.; Konig, K.; Halbhuber, K. J. Two-Photon Microscopy of Deep Intravital Tissues and its Merits in Clinical Research. *J. Microsc.* **2010**, *238*, 1-20.

16. LaFratta, C. N.; Fourkas, J. T.; Baldacchini, T.; Farrer, R. A. Multiphoton Fabrication. *Angew. Chem., Int. Ed.* **2007**, *46*, 6238-6258.

17. Stampfl, J.; Liska, R.; Ovsianikov, A. *Multiphoton Lithography: Techniques, Materials and Applications*; Wiley-VCH: Weinheim, Germany, 2017.

18. Baldacchini, T. *Three-Dimensional Microfabrication Using Two-Photon Polymerization*; Elsevier: Amsterdam, 2016.

19. Maruo, S.; Fourkas, J. T. Recent Progress in Multiphoton Microfabrication. *Laser Photonics Rev.* **2008**, *2*, 100-111.

20. Yang, D.; Jhaveri, S. J.; Ober, C. K. Three-Dimensional Microfabrication by Two-Photon Lithography. *MRS Bull.* **2005**, *30*, 976-982.

21. Farsari, M.; Vamvakaki, M.; Chichkov, B. N. Multiphoton Polymerization of Hybrid Materials. *J. Opt.* **2010**, *12*, 124001.

22. Sugioka, K.; Cheng, Y. Femtosecond Laser Three-Dimensional Micro- and Nanofabrication. *Appl. Phys. Rev.* **2014**, *1*, 041303.

23. Iliopoulos, K.; Krupka, O.; Gindre, D.; Salle, M. Reversible Two-Photon Optical Data Storage in Coumarin-Based Copolymers. *J. Am. Chem. Soc.* **2010**, *132*, 14343-5.

24. Olson, C. E.; Previte, M. J.; Fourkas, J. T. Efficient and Robust Multiphoton Data Storage in Molecular Glasses and Highly Crosslinked Polymers. *Nat. Mater.* **2002**, *1*, 225-8.

25. Parthenopoulos, D. A.; Rentzepis, P. M. Three-Dimensional Optical Storage Memory. *Science* **1989**, *245*, 843-5.

26. Strickler, J. H.; Webb, W. W. 3-Dimensional Optical Data Storage in Refractive media by 2-Photon Point Excitation. *Opt. Lett.* **1991**, *16*, 1780-1782.

27. Giuliano, C.; Hess, L. Nonlinear Absorption of Light: Optical Saturation of Electronic Transitions in Organic Molecules with High Intensity Laser Radiation. *IEEE J. Quantum Electron.* **1967**, *3*, 358-367.

28. Sutherland, R. L.; Brant, M. C.; Heinrichs, J.; Rogers, J. E.; Slagle, J. E.; McLean, D. G.; Fleitz, P. A. Excited-State Characterization and Effective Three-Photon Absorption Model of Two-Photon-Induced Excited-State Absorption in Organic Push-Pull Charge-Transfer Chromophores. *J. Opt. Soc. Am. B* **2005**, *22*, 1939-1948.

29. Zou, X.; Izumitani, T. Spectroscopic Properties and Mechanisms of Excited State Absorption and Energy Transfer Upconversion for $Er^{3+}$-Doped Glasses. *J. Non-Cryst. Solids* **1993**, *162*, 68-80.

30. Bechtel, J. H.; Smith, W. L. Two-Photon Absorption in Semiconductors with Picosecond Laser Pulses. *Phys. Rev. B* **1976**, *13*, 3515-3522.

31. Ehrlich, J. E.; Wu, X. L.; Lee, I. Y. S.; Hu, Z. Y.; Röckel, H.; Marder, S. R.; Perry, J. W. Two-Photon Absorption and Broadband Optical Limiting with bis-Donor Stilbenes. *Opt. Lett.* **1997**, *22*, 1843-1845.

32. Tian, P.; Warren, W. S. Ultrafast Measurement of Two-Photon Absorption by Loss Modulation. *Opt. Lett.* **2002**, *27*, 1634-1636.

33. Xu, C.; Webb, W. W. Measurement of Two-Photon Excitation Cross Sections of Molecular Fluorophores with Data from 690 to 1050 nm. *J. Opt. Soc. Am. B* **1996**, *13*, 481-491.

34. Xu, C.; Williams, R. M.; Zipfel, W.; Webb, W. W. Multiphoton Excitation Cross-Sections of Molecular Fluorophores. *Bioimaging* **1996**, *4*, 198-207.

35. Twarowski, A. J.; Kliger, D. S. Multiphoton Absorption Spectra using Thermal Blooming. *Chem. Phys.* **1977**, *20*, 253-258.

36. White, W. T.; Henesian, M. A.; Weber, M. J. Photothermal-Lensing Measurements of Two-Photon Absorption and Two-Photon-Induced Color Centers in Borosilicate Glasses at 532 nm. *J. Opt. Soc. Am. B* **1985**, *2*, 1402-1408.

37. Fang, H. L.; Gustafson, T. L.; Swofford, R. L. Two-Photon Absorption Photothermal Spectroscopy using a Synchronously Pumped Picosecond Dye Laser. Thermal Lensing Spectra of Naphthalene and Diphenylbutadiene. *J. Chem. Phys.* **1983**, *78*, 1663-1669.

38. Streltsov, A. M.; Moll, K. D.; Gaeta, A. L.; Kung, P.; Walker, D.; Razeghi, M. Pulse Autocorrelation Measurements Based on Two- and Three-Photon Conductivity in a GaN Photodiode. *Appl. Phys. Lett.* **1999**, *75*, 3778-3780.

39. Fischer, J.; Mueller, J. B.; Kaschke, J.; Wolf, T. J.; Unterreiner, A. N.; Wegener, M. Three-Dimensional Multi-Photon Direct Laser Writing with Variable Repetition Rate. *Opt. Express* **2013**, *21*, 26244-60.

40. Mueller, J. B.; Fischer, J.; Mayer, F.; Kadic, M.; Wegener, M. Polymerization Kinetics in Three-Dimensional Direct Laser Writing. *Adv. Mater.* **2014**, *26*, 6566-71.

41. Clauset, A.; Shalizi, C. R.; Newman, M. E. J. Power-Law Distributions in Empirical Data. *SIAM Rev.* **2009**, *51*, 661-703.

42. Sheik-Bahae, M.; Said, A. A.; Wei, T. H.; Hagan, D. J.; Van Stryland, E. W. Sensitive Measurement of Optical Nonlinearities using a Single Beam. *IEEE J. Quantum Electron.* **1990**, *26*, 760-769.

43. Ma, H.; Gomes, A. S. L.; de Araujo, C. B. Measurements of Nondegenerate Optical Nonlinearity using a Two-Color Single Beam Method. *Appl. Phys. Lett.* **1991**, *59*, 2666-2668.

44. Sheik-Bahae, M.; Wang, J.; DeSalvo, R.; Hagan, D. J.; Van Stryland, E. W. Measurement of Nondegenerate Nonlinearities using a Two-Color Z Scan. *Opt. Lett.* **1992**, *17*, 258-260.

45. Balu, M.; Hales, J.; Hagan, D. J.; Van Stryland, E. W. White- Light Continuum Z-Scan Technique for Nonlinear Materials Characterization. *Opt. Express* **2004**, *12*, 3820-3826.

46. Xia, T.; Hagan, D. J.; Sheik-Bahae, M.; Van Stryland, E. W. Eclipsing Z-Scan Measurement of $\lambda/10^4$ Wave-Front Distortion. *Opt. Lett.* **1994**, *19*, 317-319.

47. Petrov, D. V. Reflection Z-Scan Technique for the Study of Nonlinear Refraction and Absorption of a Single Interface and Thin Film. *J. Opt. Soc. Am. B* **1996**, *13*, 1491-1498.

48. Petrov, D. V.; Gomes, A. S. L.; de Araujo, C. B. Reflection Z-Scan Technique for Measurements of Optical Properties of Surfaces. *Appl. Phys. Lett.* **1994**, *65*, 1067-1069.

49. Sengupta, P.; Balaji, J.; Banerjee, S.; Philip, R.; Kumar, G. R.; Maiti, S. Sensitive Measurement of Absolute Two-Photon Absorption Cross Sections. *J. Chem. Phys.* **2000**, *112*, 9201-9205.

50. Castro, H. P. S.; Pereira, M. K.; Ferreira, V. C.; Hickmann, J. M.; Correia, R. R. B. Optical Characterization of Carbon Quantum Dots in Colloidal Suspensions. *Opt. Mater. Express* **2017**, *7*, 401-408.

51. He, J.; Qu, Y.; Li, H.; Mi, J.; Ji, W. Three-Photon Absorption in ZnO and ZnS Crystals. *Opt. Express* **2005**, *13*, 9235-9247.

52. Correâ, D. S.; De Boni, L.; Misoguti, L.; Cohanoschi, I.; Hernandez, F. E.; Mendonça, C. R. Z-Scan Theoretical Analysis for Three-, Four- and Five-Photon Absorption. *Opt. Commun.* **2007**, *277*, 440-445.

53. Tomova, Z.; Liaros, N.; Gutierrez Razo, S. A.; Wolf, S. M.; Fourkas, J. T. In Situ Measurement of the Effective Nonlinear Absorption Order in Multiphoton Photoresists. *Laser Photon. Rev.* **2016**, *10*, 849-854.

54. Liaros, N.; Cohen, S. R.; Fourkas, J. T. Determination of the Contributions of Two Simultaneous Absorption Orders using 2-Beam Action Spectroscopy. *Opt. Express* **2018**, *26*, 9492-9501.

55. Liaros, N.; Gutierrez Razo, S. A.; Fourkas, J. T. Probing Multiphoton Photophysics Using Two-Beam Action Spectroscopy. *J. Phys. Chem. A* **2018**, *122*, 6643-6653.

56. Zandrini, T.; Liaros, N.; Jiang, L. J.; Lu, Y. F.; Fourkas, J. T.; Osellame, R.; Baldacchini, T. Effect of the Resin Viscosity on the Writing Properties of Two-Photon Polymerization. *Opt. Mater. Express* **2019**, *9*, 2601-2616.

# Chapter 5: Structure and Dynamics of Bulk Acetonitrile: Molecular Simulation and Neutron Scattering

Adapted from: Cohen, S. R.; Plazanet, M.; Rols, S.; Voneshen, D. J.; Fourkas, J. T.; Coasne, B. (in preparation).
Research designed by: John T. Fourkas and Benoit Coasne
Research conducted by: Samuel R. Cohen, Marie Plazanet, Stéphane Rols, David J. Voneshen, John T. Fourkas, and Benoit Coasne
I did simulations, experiments, analyzed the data, and am co-writing the paper.

## 5.1 *Introduction*

Acetonitrile (methyl cyanide) is an aprotic organic molecule with a large, permanent dipole moment of 3.92 D.[1] The amphiphilic character of this molecule makes acetonitrile (ACN) a good solvent for many dipolar and non-dipolar solutes. Accordingly, both neat ACN and its binary mixtures with water are commonly used as the solvent medium for many reactions and separations.[2,3] ACN has also served, for several decades, as an important model system for the study of molecular liquids, due to the combination of its strong dipolar interactions and its nonassociated character.[4-43] Despite the fact that ACN is a simple, small molecule that is aprotic, the liquid nevertheless exhibits unexpectedly complex behavior. Perhaps the most notable feature of this liquid is its short-range structure and strong orientational correlations.[4-11] The most commonly cited feature of this structure is the propensity for the cyano groups of neighboring molecules to align antiparallel to one another.[4-8] This behavior is often attributed to dipole-dipole interactions, although reference interaction-site model (RISM) calculations[12] and integral equation methods[13] can reproduce the structure of this liquid without taking into account explicit attractive interactions, indicating that the molecular shape plays an important role in this organization as well.

Many theoretical,[12,13,16-19] molecular simulation,[20-35] and experimental[4-11,36-43] studies have explored the intermolecular organization and dynamics of ACN. Despite many decades of investigation, there are important outstanding questions regarding the properties of the bulk liquid, particularly with regard to the details of its orientational ordering and the relationship of this ordering to dynamics and solvation. For example, it is not yet well understood how the organization about a molecule depends on intermolecular distance in the liquid state. Previous molecular simulations using three- and six-site models for ACN revealed oscillations in an orientational correlation function extending out to at least 10 Å from a central molecule, but these works focused solely on the relative orientation as a function of the distance from this molecule.[23,32-34] A more recent study applied a reverse Monte Carlo approach to X-ray and neutron diffraction data to explore the joint orientational and positional ordering in ACN.[29]

The organization and dynamics of neat ACN at interfaces,[44-46] in mesoporous media,[47-51] and mixed with bulk[52-57] and interfacial[58-62] water are examples of topics of considerable current interest that require a more detailed understanding of the microscopic properties of neat acetonitrile. These are some of the outstanding problems that have been a driving force in the active development, characterization, and comparison of force fields for liquid ACN.[30-35,63-74] With these issues in mind, we report the results of molecular simulations and neutron scattering experiments on bulk ACN. We employ a widely-used and reliable force field for ACN[68] to undertake an in-depth characterization of this liquid's structure and dynamics. We also benchmark our results against experimental data from the literature and from our own inelastic and quasielastic neutron scattering studies.

In Section 5.2, we describe the technical details of the molecular simulations and neutron-scattering experiments. In Section 5.3, we benchmark the force field by comparing simulated structure factors with those obtained from neutron-diffraction experiments. To gain further insight into the microscopic structure, we calculate angularly resolved radial distribution functions, $g(r,\theta)$, which provide deeper insight into the organization of the liquid than is possible using conventional radial distribution functions. These two-dimensional distribution functions allow us to elucidate the details of the molecular associations among nearest-neighbor ACN molecules, which we divide into antiparallel and head-to-tail configurations. We then explore the connections between structure and dynamics by determining typical pairing times between acetonitrile molecules using the formalism of mean-first passages. We explore additional dynamical properties of ACN, including different vibrational densities of states, which we discuss in light of our experimental results obtained via quasielastic and inelastic neutron scattering (self and collective diffusivity and generalized density of states). In Section 5.4, we give concluding remarks and directions for future work.

## 5.2 *Computational and Experimental Methods*

### 5.2.1. Molecular Simulation

#### 5.2.1.1. Model

Liquid ACN was simulated using the flexible, 6-site, all-atom model developed by Nikitin and Lyubartsev,[68] which has been shown to reproduce the density, the heat of evaporation, and the site-site radial distribution functions of this liquid accurately. The model also reproduces the experimental values for the self-diffusion coefficient

and the dielectric constant of the liquid to a good approximation. An ACN molecule, with the atom labels and partial charges used in this work, is shown in Figure 5.1(A). The non-bonded interactions are described via a pair potential given by

$$E_{non-bonded} = \sum_i \sum_{j \neq i} \left\{ 4\varepsilon_{ij} \left[ \left( \frac{\sigma_{ij}}{r_{ij}} \right)^{12} - \left( \frac{\sigma_{ij}}{r_{ij}} \right)^{6} \right] + \frac{1}{4\pi\varepsilon_0} \frac{q_i q_j}{r_{ij}} \right\}. \quad (5.1)$$

This potential consists of 12-6 Lennard-Jones and Coulombic terms, where *i* and *j* are on different molecules, $\varepsilon_{ij}$ and $\sigma_{ij}$ are the Lennard-Jones parameters for the potential-well depth and characteristic site radius, respectively, $r_{ij}$ is the separation distance between sites *i* and *j*, $\varepsilon_0$ is the permittivity of vacuum, and $q_i$ and $q_j$ are the charges on sites *i* and *j*, respectively. For atoms on the same molecule, the only non-bonded interactions considered are the 1,4 interactions. The 1,4 electrostatic interactions are scaled by a factor 0.83, and the 1,4 Lennard-Jones interactions are scaled by a factor 0.5. The energy $E_{bonded}$ of the intramolecular terms is

$$E_{bonded} = \sum_{bonds} K_r (r - r_0)^2 + \sum_{angles} K_\theta (\theta - \theta_0)^2, \quad (5.2)$$

where $K_r$ is the harmonic bond coefficient, *r* is the bond distance, $r_0$ is the equilibrium bond distance, $K_\theta$ is the harmonic angle coefficient, and $\theta_0$ is the equilibrium value of angle $\theta$. The CT-YC-YN angle is 180˚, the HC-CT-YC angle is 110˚, and the HC-CT-HC angle is 109.5˚. The total energy of the system is the sum of the bonded and non-bonded energies. Long-range Coulombic interactions were included using Ewald

summation with a precision of $10^{-5}$. The cut-off distances for the Lennard-Jones interactions and the real-space part of the Ewald sum were both set to 14 Å. Figure 5.1(B) shows a representative configuration from a simulation of the bulk liquid.

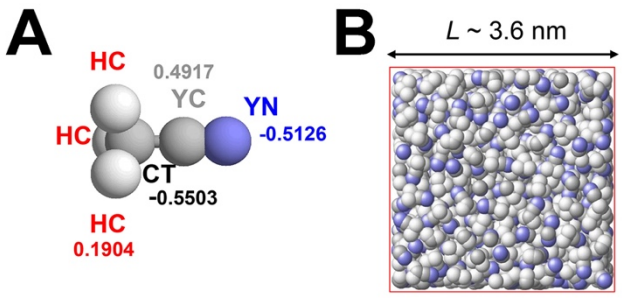


**Figure 5.7** (A) An acetonitrile molecule, showing the label and partial charge for each atom type. Representative molecular configuration at $T$ = 298 K for (B) bulk liquid acetonitrile; the red frame indicates the molecular simulation box used in the calculations.

### 5.2.1.2. Molecular Dynamics Simulations

Molecular dynamics simulations were performed with LAMMPS[75] using the interaction potentials in Eqs. (5.1) and (5.2). The equations of motion were integrated with a time step of 1 fs. Configurations and thermodynamic data were stored every 5 fs, except in the calculation of the velocity autocorrelation function, for which such information was stored every 1 fs. All of the initial configurations were built using PACKMOL,[76] and the simulations were preceded by an energy minimization with an energy tolerance of $10^{-6}$. The simulations for the bulk liquid used a 36 Å×36 Å×36 Å box with periodic boundary conditions. A simulation was performed to measure the density of the bulk liquid by equilibrating in the isothermal/isobaric (*NPT*) ensemble at 298 K and 1 bar for 200 ps using a Nosé-Hoover thermostat and barostat[77] with 30 fs and 1000 fs relaxation constants, respectively. Using the equilibrated systems, the

simulation was then run in the *NPT* ensemble up to 2 ns. All other simulations were equilibrated in the *NVT* ensemble at 298 K for 200 ps using a Nosé-Hoover thermostat with a 30 fs relaxation constant. Using the equilibrated systems, the simulations were then run in the *NVE* ensemble up to 2 ns for the bulk liquid.

### 5.2.2. Neutron-Scattering Experiments

Neutron-scattering measurements were performed at ISIS (UK) on the LET time-of-flight spectrometer. Based on the repetition-rate multiplication, energies of 1.78, 2.83, 5.18, 12.39, and 60.11 meV were selected from the incoming beam. Scattered neutrons were monitored on detector banks covering the angular range from 5° to 135°. Because all incident energies gave consistent data, we present here only data recorded with $E_i = 2.83$ meV, which best cover the energy and $q$ ranges of interest, enabling a resolution of 70 μeV for the elastic line. Data were reduced using standard routines included in Mantid,[78] and fitting of the data was performed in the Large-Array Manipulation Program (LAMP).[79]

#### 5.2.2.1. Inelastic Neutron Scattering

Scattering involving energy transfers larger than ~1 meV that arises from a periodic excitation is considered to be inelastic. Scattering in such a process is not limited by any selection rules, and multiphonon processes occur. The double differential cross section of neutron scattering can be written as:[80]

$$\left(\frac{d^2\sigma}{d\Omega d\omega}\right)_{inc} =$$

$$\frac{k_f}{k_i}\sum_\kappa \frac{\sigma_{inc}(\kappa)}{8\pi m_\kappa}\sum_{j\in\{j_\kappa\}} e^{-2W_j(\vec{q})}\sum_i \frac{|\vec{q}.\vec{e}_i(j)|^2}{\omega_i}[(n(\omega_i)+1)\delta(\omega-\omega_i)]\ , \quad (5.3)$$

where $k_{we}$ and $k_f$ are the wave vectors of the incident and scattered neutrons, $\Omega$ is the scattering solid angle, $\omega$ is the angular frequency, $\vec{q}$ is the momentum transfer, $W(\vec{q})$ is the Debye-Waller factor, $n(\omega)$ is the Bose occupation factor, $m$ the mass of the scattering atom, and $\vec{e}_i(j)$ its displacement in the vibrational mode $i$, $\sigma_{inc}(\kappa)$ the neutron incoherent scattering cross section of the atoms of type $\kappa$. For an isotropic and incoherent sample, one can simplify Eq. (5.3) to obtain:[80]

$$\left(\frac{d^2\sigma}{d\Omega d\omega}\right)_{inc} = \frac{k_f}{k_i}\frac{q^2}{3}\sum_\kappa \frac{\sigma_{inc}(\kappa)}{8\pi m_\kappa}\sum_{j\in\{j_\kappa\}} e^{-2W_j(\vec{q})}\frac{g_j(\omega)}{\omega}(n(\omega)+1)\ , \quad (5.4)$$

where $\sigma_{inc}(\kappa)$ is the neutron incoherent scattering cross section, and $g_j(\omega)$ is the density of states of atom $j$ of type $\kappa$ for all the modes $i$:

$$g_j(\omega) = \sum_i |\vec{e}_i(j)|^2\delta(\omega-\omega_i)\ . \quad (5.5)$$

Summing Eq. (5.4) over all atoms $j$ and type $\kappa$, we obtain:

$$\left(\frac{d^2\sigma}{d\Omega d\omega}\right)_{inc} = \frac{k_f}{k_i}q^2\frac{N}{8\pi}e^{-2W(q)}\frac{G(\omega)}{\omega}(n(\omega)+1)\ , \quad (5.6)$$

where $G(\omega)$ is the generalized density of states (GDOS) given by

$$G(\omega) = \sum_{\kappa=1}^{N} \frac{\sigma_{inc(\kappa)}}{m_\kappa} g_\kappa(\omega) \,, \tag{5.7}$$

and $g_\kappa(\omega)$ is the partial density of states for all of the atoms *N* of a given chemical species $\kappa$. The quantity $g_\kappa(\omega)$ is experimentally accessible using inelastic neutron scattering. In the case of ACN, the experimentally-derived GDOS is dominated by the hydrogen contribution. When H is replaced by D (ACN-$d_3$), one must invoke the so-called "incoherent approximation"[81] to derive $G(\omega)$. The use of this approximation necessitates averaging the coherent cross section over a large domain of momentum transfer, which is assured in our experiments by the use of a detector bank covering a range of scattering angles.

#### 5.2.2.2. Quasielastic Neutron Scattering

Quasielastic neutron scattering (QENS) refers to the symmetric broadening of the elastic line by the scattering of neutrons from diffusive excitations, such as rotational and translational dynamics. The QENS signal, from which $S(q,\omega)$ is extracted, can be sliced at constant $q$ and described in a first approximation by a sum of Lorentzian functions:

$$S(q,\omega) = e^{-2W(q)}\{\sum_i A_i(q) \times L_i(q,\omega)\} \otimes R(q,\omega) + b(q) \,, \tag{5.8}$$

where the $L_i(q,\omega)$ are the Lorentzian contribution to the QENS signal, the $A_i(q)$ are the corresponding amplitudes, $R(q,\omega)$ is the resolution function of the instrument, and $b(q)$ is the flat background. The widths and amplitudes of the Lorentzians as a function of $q$ enable the determination of the rotational or translational nature of the dynamics.

We further refined the model using a sum of two terms describing molecular rotations convolved with the translational dynamics, so that we obtain:

$$S(q,\omega) = \exp\left(-\frac{\langle u^2 \rangle q^2}{3}\right)\begin{pmatrix} \left(I(q)_{El}\,\delta(\omega)\right) \\ +\left(S(q,\omega)_T \otimes S_1(q,\omega)_R\right) \\ +\left(S(q,\omega)_T \otimes S_2(q,\omega)_R\right) \end{pmatrix}, \tag{5.9}$$

where $\langle u^2 \rangle$ is the mean-squared displacement and $I(q)_{\mathrm{El}}$ is the remaining elastic peak arising from the sample holder. This latter feature was fitted with an elastic peak by multiplication with the delta function $\delta(\omega)$. The first and second rotational contributions correspond to the spinning and tumbling of the molecule. The translational contribution can be written as:[82]

$$S(q,\omega)_T = \frac{1}{\pi}\frac{\Gamma_T}{\omega^2+\Gamma_T^2}\ , \tag{5.10}$$

where $\Gamma_T$ is the half-width at half maximum of the translational Lorentzian function, and is defined as:

$$\Gamma_T = \frac{D_T q^2}{1+\tau D_T q^2}\ , \tag{5.11}$$

where $D_T$ is the self-diffusion constant and $\tau$ is the residence time. we assume isotropic rotational contributions such that the rotational contribution can be written as:[82]

$$S(q,\omega)_R = A_0(q)\delta(\omega) + \sum_{i=1}^{\infty} A_i(q)\frac{1}{\pi}\frac{\Gamma_i}{(\omega)^2+\Gamma_i^2}\,, \tag{5.12}$$

with

$$A_i(q) = (2i+1)j_i^2(qR) \tag{5.13}$$

and

$$\Gamma_i = i(i+1)D_R\,, \tag{5.14}$$

where $R$ is the radius of rotation. $D_R$ is the isotropic rotational diffusion constant, which is related to the characteristic rotational time by $\tau_R = 1/(2D_R)$.

## 5.3 *Results and Discussion*

### 5.3.1. Structure

To compare the structure of the simulated liquid with experimental measurements, the total static structure factor $S(q)$ was calculated for three different ACN isotopologues. The total structure factor is proportional to the differential scattering cross-section that is measured in diffraction experiments. For a polyatomic system such as ACN, the total structure factor is essentially a weighted sum of the partial structure factors.[83] The partial structure factors $S_{\alpha\beta}(q)$ for $N_{mol}$ molecules consisting of atoms $\alpha$ and $\beta$ were calculated according to[84]

$$S_{\alpha\beta}(q) = \left\langle \frac{1}{N_{mol}}\rho_q^{\alpha}\rho_{-q}^{\beta} \right\rangle, \tag{5.15}$$

where $\rho_q^{\alpha}$ and $\rho_{-q}^{\beta}$ are the Fourier components of the microscopic density,

$$\rho_q^{\alpha} = \sum_{i=1}^{N_\alpha} e^{-iq \cdot r_{\alpha,i}} \tag{5.16}$$

and

$$\rho_{-q}^{\beta} = \sum_{i=1}^{N_\beta} e^{iq \cdot r_{\beta,i}} \tag{5.17}$$

for the numbers $N_\alpha$ and $N_\beta$ of atoms in the system with position vectors $r_{\alpha,i}$ and $r_{\beta,i}$ for the *i*th atom of type $\alpha$ and $\beta$, respectively, and $q$ is the magnitude of the scattering wave vector. The brackets in Eq. (5.15) denote an ensemble average. To obtain the total structure factor, the partial structure factors were multiplied by the corresponding neutron coherent scattering lengths $\overline{b}_\alpha$, $\overline{b}_\beta$ of each component according to

$$S(q) = \sum_{\alpha,\beta=1}^{6} \overline{b}_\alpha \overline{b}_\beta S_{\alpha\beta}(q) / \sum_{\alpha=1}^{6} \overline{b}_\alpha{}^2 , \tag{5.18}$$

where the choice of denominator normalizes the function to 1 at large $q$.

The simulated structure factors for the three isotopologues are plotted in Figure 5.2, and the corresponding experimental static structure factors for $CD_3C^{15}N$ and $CD_3C^{14}N$ are shown for comparison. There is excellent agreement between the simulated and experimental static structure factors for these liquids. Note that we could not find any experimental results for $CH_3CN$ in the literature, presumably because the strong incoherent background from the hydrogen atoms masks most of the signal. A sharp diffraction peak in the vicinity of $q$ = 1.5 to 2 Å$^{-1}$ is present in all cases, and is indicative of short-range order. However, it is difficult to interpret the structure factors qualitatively beyond this observation. It is more informative to study pair correlations in real space via partial radial distribution functions.

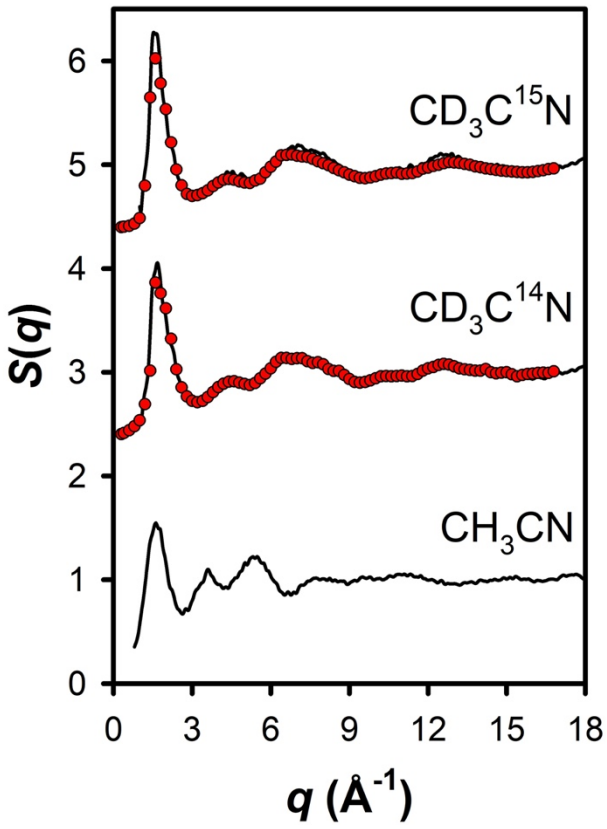


**Figure 5.8** Static structure factor $S(q)$ for bulk ACN at 298 K as obtained from molecular simulations (black) and neutron-diffraction experiments[9,10] (red), where $q$ is the magnitude of the scattering wave vector. The three sets of data are for different isotopologues, with deuterium/hydrogen and/or $^{14}N/^{15}N$ isotopic substitutions. The $S(q)$ for the three different isotopologues are offset vertically for clarity.

The center-of-mass radial distribution function and partial radial distribution functions are shown in Figure 5.3. In previous works, the partial radial distribution functions for ACN have been found to be quite sensitive to the dipole-dipole interactions.[23,32,34] In contrast, the structure factors have been shown to be reproducible without taking attractive interactions into account explicitly,[12,13] which led to the conclusion[32] that structure factors are not particularly sensitive to details of the intermolecular effects of electrostatic attractions. The subset of partial radial distribution functions shown in Figure 5.3 that have been reported previously are essentially the same as in prior work,[68] and all of the partial radial distribution functions

are similar to those reported for extensively-studied three-[32,33,65] and six-site[64,66] models and reverse Monte Carlo simulations.[29] Although only a single replica was simulated, the radial distributions for both the bulk (Chapter 5) and interfacial (Chapter 6) simulations are identical regardless of where in the trajectory the analysis begins. This observation suggests that there is stabilization of structural properties.

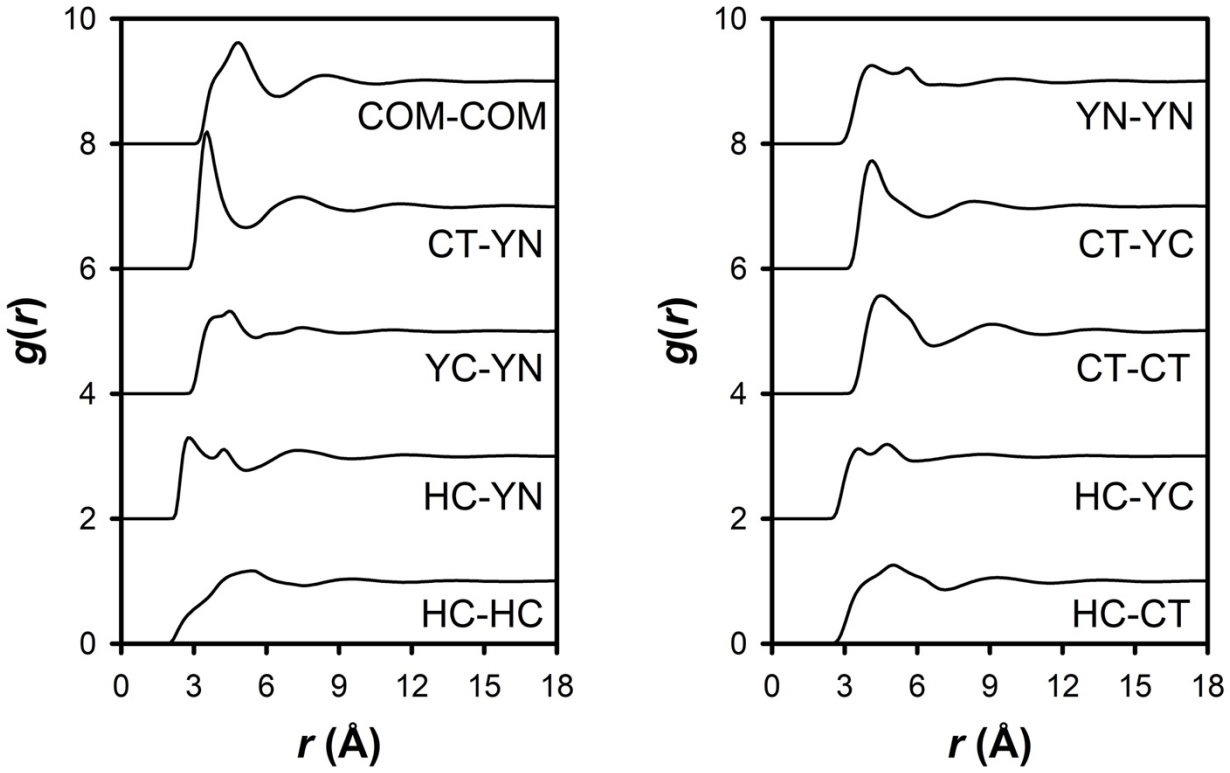


**Figure 5.3** Simulated radial distribution function $g(r)$ between different acetonitrile atom types and for the molecular center of mass (COM) in the bulk liquid at 298 K. In both panels, some of the functions are offset vertically for clarity.

To gain deeper insight into the orientational ordering of liquid ACN, we calculated angularly resolved radial distribution functions, $g(r,\theta)$. By normalizing the data to the value of $g(r)$ for each $r$, these plots give the probability that two ACN molecules with selected sites separated by a distance $r$ make an angle $\theta$. Here, $\theta$ is calculated from the dot product between unit vectors on different molecules, as determined using the CT-YN vector in the direction of YN on each molecule. In polyatomic liquids, $g(r,\theta)$ can be considerably more informative than a traditional radial distribution function.[56,85,86] In Figure 5.4, we show $g(r,\theta)$ for the molecular center-of-mass, along with the corresponding $g(r)$. The center-of-mass $g(r,\theta)$ shows that there are two distinct populations contributing to $g(r)$ at short distances. The first peak in $g(r)$ arises from antiparallel pairs of molecules with a center-of-mass separation on the order of 3.8 Å (configuration 1 in Figure 5.4). We note that these molecules are not dipole-paired in the traditional sense in which this term is used for acetonitrile, in which the cyano groups of the two molecules interact with one another;[4] rather, the molecules align as to allow for favorable interactions among all of the complementary partial charges on the atoms (see Figure 5.1). We therefore refer to this motif as octupole pairing. The second peak arises from a population of head-to-tail pairs with a broad distribution of angles centered around ~90° (configuration 2 in Figure 5.4). Note that the area under this second peak is much larger than that under the first peak. The center-of-mass separation in the latter pairs decreases with increasing $\theta$.

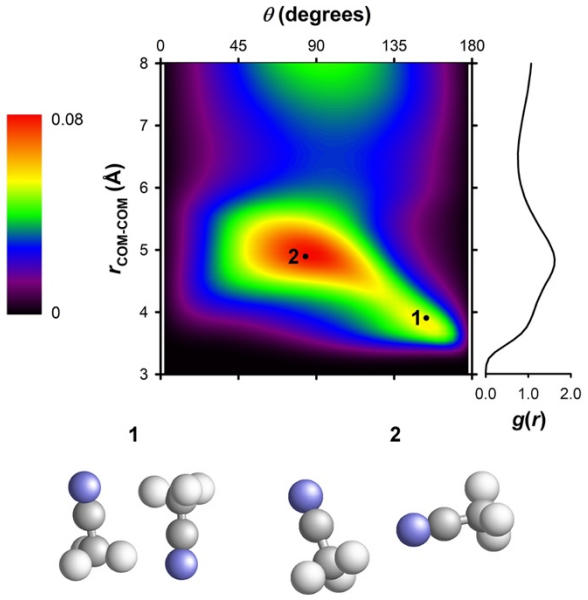


**Figure 5.4** The center-of mass $g(r,\theta)$ and $g(r)$ for acetonitrile, along with representative configurations from the indicated regions.

For comparison with the reverse Monte Carlo work of Pothoczki and Pusztai,[29] we show in Figure 5.5 our distance-dependent, normalized angular probability distribution $g_{\text{CT-CT}}(r,\cos\theta)$ alongside that from the reverse Monte Carlo study. We note that $\theta$ and $\cos\theta$ have both been used for the abscissa in previously published angularly resolved radial distribution functions.[87-89] We have chosen to use $\theta$ here to maintain a linear scale. In Figure 5.6, we show the normalized angularly resolved $g(r,\theta)$, calculated with respect to the distances between the centers of mass, alongside the corresponding $g(r,\cos\theta)$. Despite the fact that the two plots differ substantially in appearance, we demonstrate in Figure 5.7 that the angular integral of each normalized function at fixed $r$ is the same.

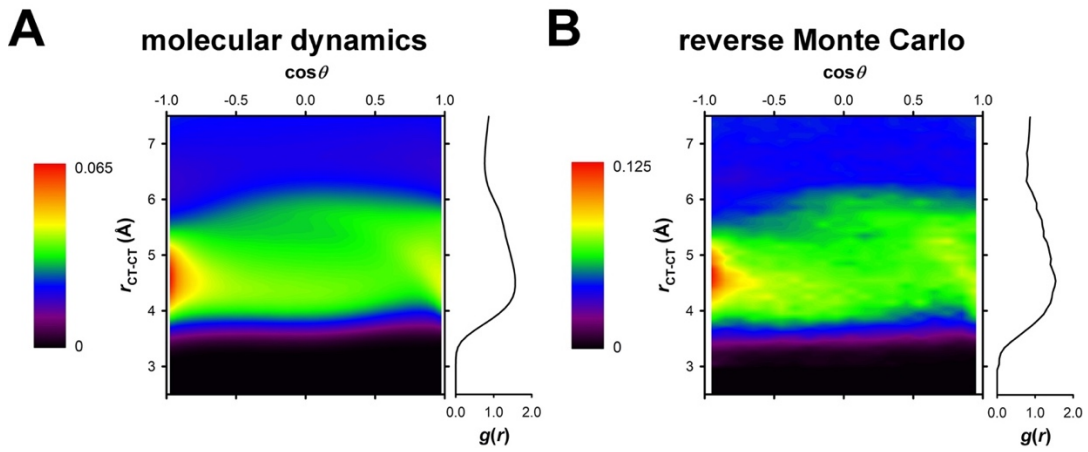


**Figure 5.5** Comparison of $g_{CT\text{-}CT}(r,\cos\theta)$ calculated (A) from a molecular dynamics simulation (this work) using the force field of Nikitin and Lyubartsev[68] and (B) by the reverse Monte Carlo method[29] using the OPLS-AA[90] force field as a constraint. In each case the corresponding $g(r)$ is shown for comparison. The data in panel (B) for both $g_{CT\text{-}CT}(r)$ and the unnormalized $g_{CT\text{-}CT}(r,\cos\theta)$ were provided by one of the authors (S. Pothoczki) of the reverse Monte Carlo study. In (A) the bin size is 0.1 Å in $r$ and 0.05 in cos $\theta$. In (B) the bin size is 0.1 Å in $r$ and 0.10 in cos $\theta$. The difference in bin sizes in $\theta$ is responsible for the different $z$ scaling of the two heat maps.

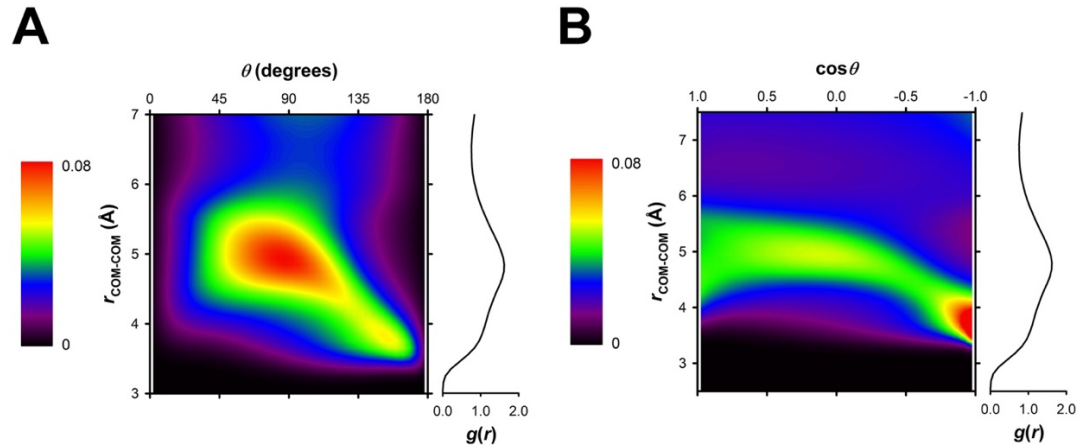


**Figure 5.6** Angularly resolved radial distribution functions calculated with respect to the center-of-mass separation. Panel (A) shows $g(r,\theta)$ and panel (B) shows $g(r,\cos\theta)$. Note that in (B) the $\cos\theta$ axis goes from 1 to -1 for ease of comparison. The corresponding $g(r)$ is shown next to each heat map. These two plots indicate that the two different representations highlight different features of the orientational distribution. The bin size in $r$ is 0.1 Å in each plot. The bin size in $\theta$ is 4° and the bin size in $\cos\theta$ is 0.05.

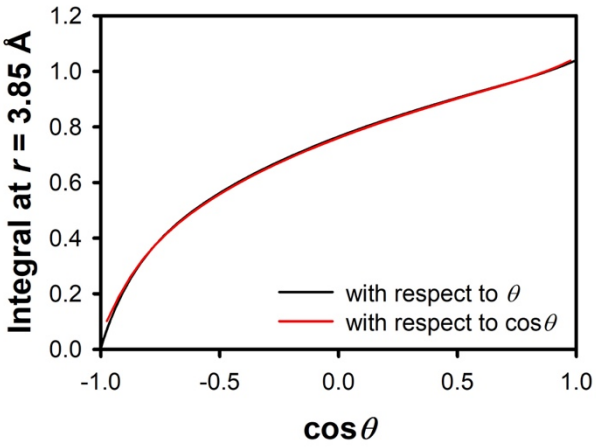


**Figure 5.7** Integral of normalized $g(r,\theta)$ and $g(r,\cos\theta)$ with respect to $\theta$ and with respect to $\cos\theta$, respectively, at a center of mass-center of mass distance of $r$ = 3.85 Å. The integrals extend from 180° to $\cos^{-1}(\cos\theta)$ and -1 to $\cos\theta$, respectively. The close correspondence between the two plots indicates that the heat maps in Fig. 5.5 display the same data, despite their different appearances.

As shown in Figure 5.5, our molecular simulation results are in good agreement with the results of Pothoczki and Pusztai,[29] which were obtained using the reverse Monte Carlo method with the OPLS-AA[90] force field as a constraint. It is interesting to note that these two distinct numerical approaches lead to similar microscopic organization despite very different hypotheses. Molecular dynamics relies purely on a force field, whereas reverse Monte Carlo consists of an error minimization between the experimental and simulated radial distribution function. In particular, even though the reverse Monte Carlo calculations in [29] are further constrained by the use of the OPLS-AA force field, this force field differs from the one used in our molecular dynamics simulations, and so cannot be the source of the similarities. Reconstruction of a fully three-dimensional picture of a material from knowledge of lower-order correlation functions is a well-known inverse problem,[91] and from this perspective it can be understood that one-dimensional structural functions, which give pair

information, under-constrain the problem of liquid structure. It is therefore not obvious that the microscopic organization in the two models should be the same, and our comparison of the models highlights the ability of multidimensional visualizations to reveal liquid structure. Our results show that molecular simulation can reveal details that are inaccessible using either the reverse Monte Carlo method or experiment.

In Figure 5.8, we show the angularly resolved radial distribution functions involving the physical centers of the methyl (Me) and cyano (CN) groups, i.e., $g_{\text{Me-Me}}(r,\theta)$, $g_{\text{Me-CN}}(r,\theta)$, and $g_{\text{CN-CN}}(r,\theta)$. The corresponding $g(r)$ is presented in each case for comparison. Our choice of these two functional groups was inspired by investigations into nanostructural organization in ionic liquids,[92] and by molecular simulations[55,57] of acetonitrile-water mixtures that showed evidence of microheterogeneities when examining differences in the partial radial distribution function between the methyl group and the central carbon of ACN at different concentrations. Although our results do not provide unambiguous evidence of such organization in bulk ACN, these angularly resolved radial distribution functions provide a wealth of new information about the organization of this liquid.

The Me-Me partial radial distribution is broad and relatively featureless. Correspondingly, $g_{\text{Me-Me}}(r,\theta)$ (Figure 5.8) is also relatively featureless, indicating that the methyl groups do not have a preference for specific directional interactions. It is notable, however, that this distribution peaks at an angle of ~90° for the initial maximum in $g(r)$, and there is a low probability for relative orientations near 0° and 180° through the entire range of $r$ investigated. There is a roughly monotonic decrease in the closest distance between methyl groups with increasing angle between

molecules. There is lobe in the distribution at a distance of approximately 5 Å arising from roughly antiparallel, octupole-paired molecules (configuration 3), and another lobe at approximately 6 Å arising from offset, head-to-tail molecules (configuration 4). The peak at ~90˚ indicates that this population is composed largely of offset, head-to-tail pairs rather than end-on, head-to-tail pairs (configuration 5).

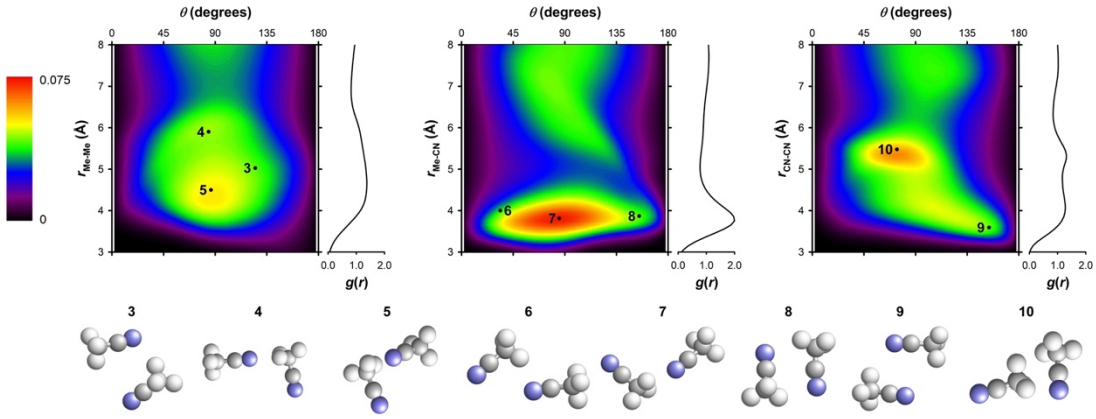


**Figure 5.8** Radial distribution functions and angularly resolved radial distribution functions for acetonitrile with respect to the methyl-methyl distance, the methyl-cyano distance, and the cyano-cyano distance for different molecules, with the angle $\theta$ defined as described in the text, along with representative configurations from the indicated regions. Note each representative configuration in the figure is unique.

The pronounced first peak in $g_{\text{Me-CN}}(r)$ is qualitatively similar to the first peak in the $g_{\text{CT-YN}}(r)$ corresponding to the CT-YN distance (Figure 5.3), which has been interpreted previously in simulations of both three-[32] and six-site[34] models of ACN to reflect the head-to-tail alignment of neighboring dipoles. The $g_{\text{Me-CN}}(r,\theta)$ in Figure 5.8 instead reveals the presence of structures in which the nitrogen atom associates with a methyl group in an offset head-to-tail fashion, with angles ranging from small acute angles (configuration 6) to large acute angles (configuration 7) to octupole pairs

(configuration 8). Even the pairs at small acute angles are dominated by offset, rather than true, head-to tail structures.

Based on previous work, $g_{CN\text{-}CN}(r)$ is expected to reflect dipole pairing of cyano groups.[32] However, the first feature of $g_{CN\text{-}CN}(r)$ exhibits two peaks. The corresponding angularly resolved radial distribution function (Figure 5.8) demonstrates that these peaks correspond to two different types of local structures. The peak at shorter separations corresponds to antiparallel, octupole-paired dimers (configuration 9), in which the nitrogen atom of one molecule is associated with a hydrogen atom of another molecule. Here, and in the other angularly resolved radial distribution functions, we find no evidence for a significant population of dipole-paired dimers. The other dominant structural motif in liquid acetonitrile, the formation of head-to-tail dimers, is observed in all of the angularly resolved radial distribution functions shown here. In $g_{CN\text{-}CN}(r, \theta)$ in Figure 5.8, the peak at larger separations arises from dimers in which one cyano group associates with a methyl group in an offset, head-to-tail fashion (configuration 10).

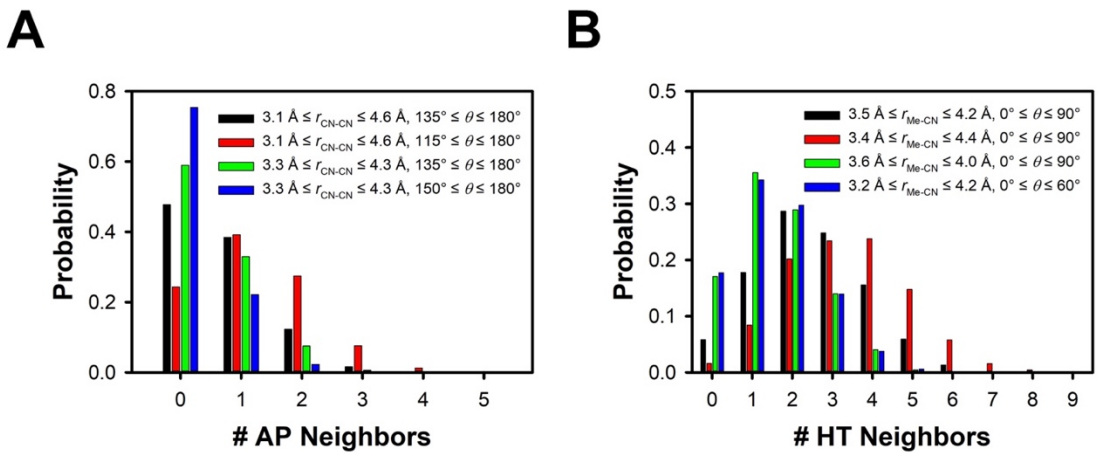


**Figure 5.9** Histograms comparing the probability distributions for neighbors that are (A) antiparallel and (B) head-to-tail for different sets of criteria. In both cases, the qualitative characteristics of the distributions are not highly sensitive to the selection criteria.

To analyze the population of head-to-tail dimers, we isolated molecular pairs based on $g_{\text{Me-CN}}(r,\theta)$. We investigated several sets of reasonable criteria for dimers based on $r$ and $\theta$. All of the sets tested gave qualitatively similar results, revealing a population of neighboring head-to-tail dimers, with many molecules forming dimers with more than one neighbor. In Figure 5.9 we show a comparison of the populations of dimers for the different sets of criteria. Here we use the criteria 3.5 Å ≤ $r_{\text{Me-CN}}$ ≤ 4.2 Å and 0˚ ≤ $\theta$ ≤ 90˚. We isolated molecular pairs meeting these criteria and calculated the angle $\alpha$ formed by the unit vector along the principal molecular axis of a molecule 1 with the unit vector between the methyl group of a molecule 1 and the cyano group of a molecule 2, as indicated schematically in Figure 5.10. We used this information to assess whether head-to-tail pairing predominantly involves end-on or offset associations. Figure 5.10 shows the probability that two acetonitrile molecules that meet the above criteria are separated by a distance $r$ and make an angle $\alpha$. Note that we have normalized the data to $P(r)$, the probability of the molecules in the pair having a center-of-mass separation of $r$ for each $r$. The probability $P'(\alpha)$ of the molecules in the

pair having an angle $\alpha$ is also shown. For end-on dimers, we would expect the latter distribution to be peaked at a relatively small value of α, with the center-of-mass separation decreasing with increasing α. The fact that the peak at an angle of ~97° indicates, however, that offset head-to-tail dimers dominate this population. This picture is confirmed by the representative pair configuration shown (configuration 11). The appearance of molecular pairs at angles greater than 90˚ (configurations 11 and 12) is a clear sign that offset pairing is dominant. An end-on configuration is also shown (configuration 13) for comparison.

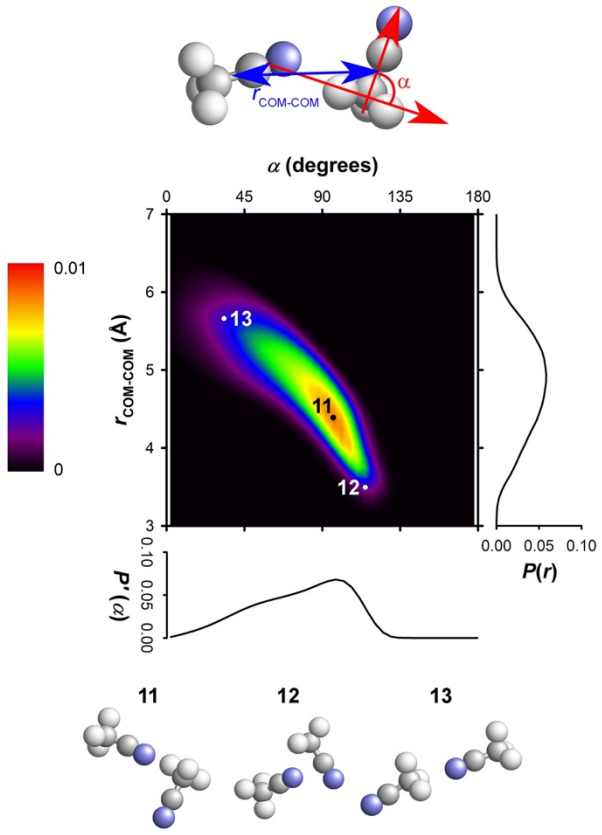


**Figure 5.10** Analysis of head-to-tail dimers, with the angle $\alpha$ defined by the unit vector along the principal molecular axis of a molecule 1 with the unit vector between the methyl group of the molecule 1 and the cyano group of a molecule 2. The directions of the unit vectors are illustrated schematically in the figure. The probabilities $P(r)$ and $P'(\alpha)$ are defined as described in the text.

Together, these results point to the existence of two distinct pair populations in liquid acetonitrile: antiparallel, octupole-paired molecules, and offset, head-to-tail molecules. It is interesting to explore whether these same motifs are prominent in the common crystalline phases of acetonitrile. We therefore determined the angularly resolved radial distribution functions for the $\alpha$ and $\beta$ crystalline polymorphs of acetonitrile, based on crystallographic data.[93] The $g(r,\theta)$ for the Me-CN and CN-CN interactions for both phases are shown in Figure 5.11. For the high-temperature $\alpha$ polymorph, $g_{\text{Me-CN}}(r,\theta)$ in Figure 5.8 reveals the presence of a substantial population of perpendicular, end-on, head-to-tail dimers (configuration 14) and parallel, offset dimers (configuration 15) that are not common in the liquid. There are also dimers that are arranged in a perpendicular, offset, head-to-tail fashion (configuration 16) and an octupole-paired fashion (configuration 17) that correspond strong with the liquid structure. The corresponding $g_{\text{Me-CN}}(r,\theta)$ for the $\beta$ polymorph also features end-on, head-to-tail dimers (configuration 18) and offset parallel dimers (configuration 19) that do not have a strong presence in the liquid. The highest peak in this angularly-resolved radial distribution function is for roughly perpendicular, offset, head-to-tail dimers (configuration 20), again as found in the liquid.

The plot of $g_{\text{CN-CN}}(r,\theta)$ for the $\alpha$ polymorph shown in Figure 5.11 reveals populations of octupole-paired dimers (configuration 21), and perpendicular, offset, head-to-tail dimers (configuration 22), as in the bulk liquid. There are also offset parallel dimers (configuration 23) that are not present in the bulk liquid, as well as roughly perpendicular head-to-tail dimers at larger separations (configuration 24) that are found in the bulk liquid. In the $\beta$ polymorph, the largest peak arises from offset

parallel dimers (configuration 25) that do not have a strong presence in the liquid. There are also two peaks corresponding to roughly perpendicular head-to-tail dimers (configurations 26 and 27) that are important in the liquid. The angularly resolved radial distribution functions for the Me-Me and center-of mass separations tell a similar story (Figure 5.12). We can conclude that the offset parallel dimers that are seen in the crystalline phase are driven by packing constraints, whereas the offset, head-to-tail and octupole-paired dimers present in all three phases are energetically favorable.

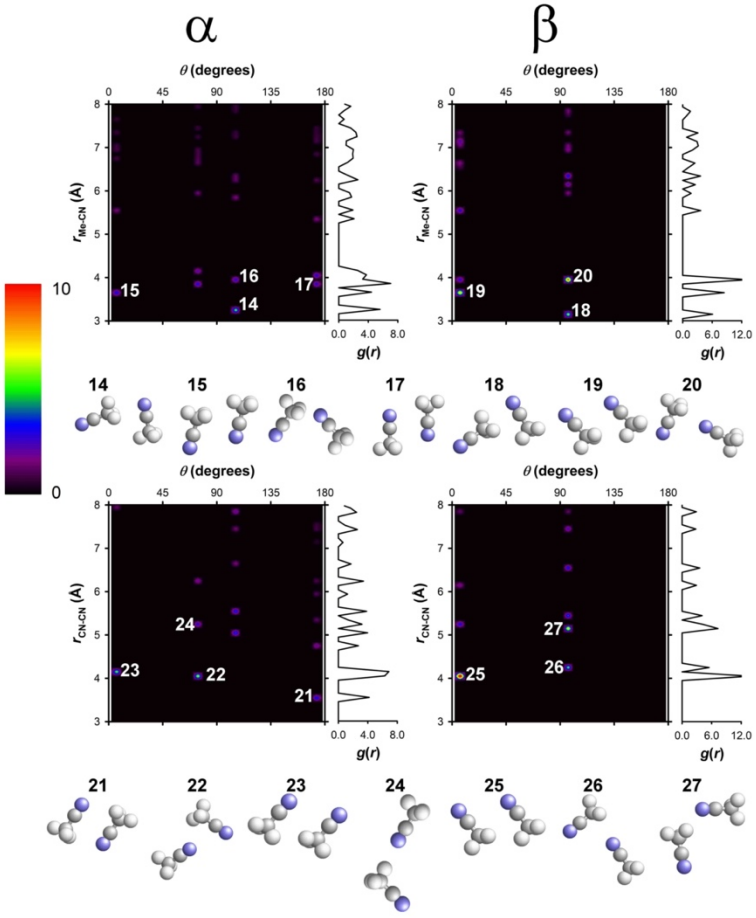


**Figure 5.11** Radial distribution functions and angularly resolved radial distribution functions for crystalline acetonitrile with respect to the methyl-cyano distance for the $\alpha$ polymorph (top left) and the $\beta$ polymorph (top right) as well as with respect to the cyano-cyano distance for the $\alpha$ polymorph (bottom left) and for the $\beta$ polymorph (bottom right).

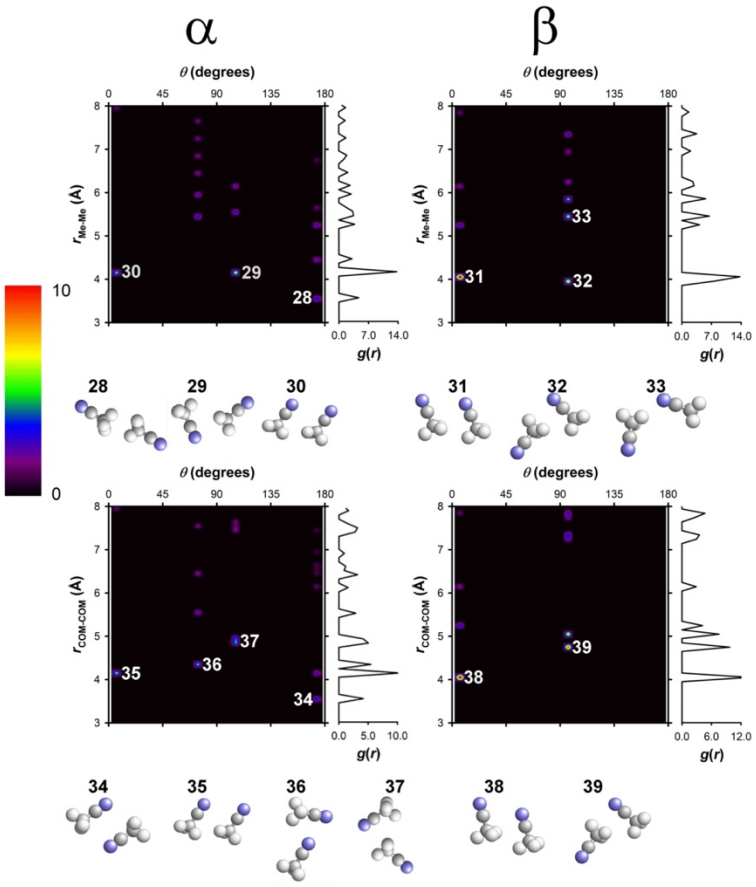


**Figure 5.12** Radial distribution functions and angularly resolved radial distribution functions for crystalline acetonitrile with respect to the center-of-mass distance for the $\alpha$ polymorph (top left) and the $\beta$ polymorph (top right) as well as with respect to the cyano-cyano distance for the $\alpha$ polymorph (bottom left) and for the $\beta$ polymorph (top right).

To analyze the pairing in the liquid in more detail, we created a 2-D histogram of the number of paired antiparallel and head-to-tail molecules (Figure 5.13), with the pairing for antiparallel molecules defined, based on $g_{\text{CN-CN}}(r,\theta)$, by the criteria 3.1 Å ≤ $r_{\text{CN-CN}}$ ≤ 4.6 Å and 135˚ ≤ $\theta$ ≤ 180˚ (for a comparison of different criteria, see Figure 5.9). The 1-D probabilities $P(n)$ for either antiparallel or head-to-tail dimers are given alongside the 2-D histogram. It is clear from Fig. 5.13 that molecules are not necessarily paired only to a single neighbor, and molecules participating in head-to-tail pairs are

rarely paired only to one neighbor. It is noteworthy that less than 2% of molecules are unpaired at any given time. The lifetimes of pairs are discussed in Sec. 5.3.2.1.

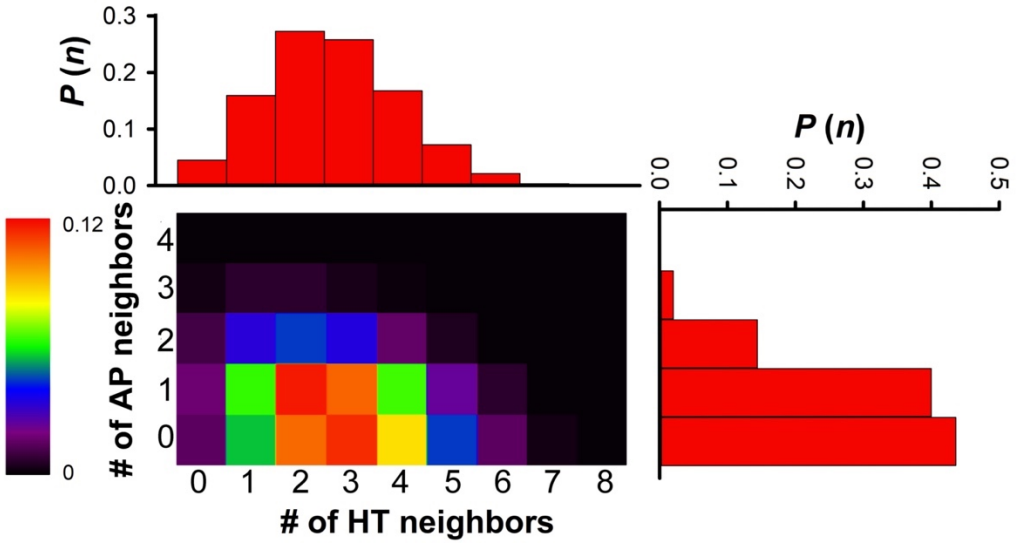


**Figure 5.13** Probability that an acetonitrile molecule is associated with antiparallel (AP) or head-to-tail (HT) neighbors, as defined in the text.

### 5.3.2. Dynamics and Vibrational Properties

#### 5.3.2.1. Molecular Dynamics

Figure 5.14 shows the mean-squared displacements (MSDs) as a function of time for each atomic site, as determined from the molecular dynamics trajectory. As expected, in the long-time limit, all atomic MSDs merge, as rotations and individual motions become negligible compared to the typical center-of-mass displacements. In this long-time limit, the self-diffusivity can be obtained from such atomic MSDs using the Einstein equation, $D_s \sim \Delta r^2/6t$.[84] From the MSD, we calculated a value of $3.79\times10^{-5}$ cm$^2$/s for the self-diffusion coefficient (Table 5.1). This self-diffusivity is somewhat lower than the experimental value, in agreement with previous results.[68] Additional

useful dynamical information can be inferred from short-time behavior of the atomic MSDs in Figure 5.14. The hydrogen atoms, which are light, move in a superdiffusive, ballistic regime at short times, due to the spinning of the molecule about its long axis (which is the same as methyl-group rotation). Because spinning constrains the hydrogen atoms to move in circles, the hydrogen-atom MSD only appears ballistic on sufficiently short time scales. The fact that the hydrogen atoms are farther from the molecular center of mass than are any other atoms means that tumbling rotation makes this MSD larger than any of the other atomic MSDs until the Fickian limit is reached. Conversely, the central carbon (YC) is close to the center of mass, which means that its MSD is the least affected by tumbling, and is slightly smaller than the values for the other atomic sites until the Fickian limit is reached.

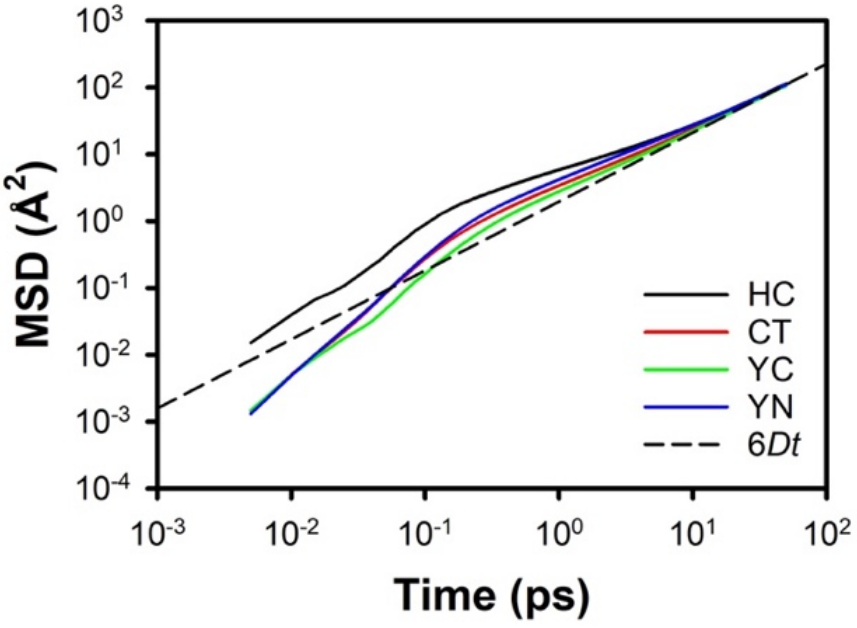


**Figure 5.14** Mean-squared displacement as a function of time for each atomic site. The line indicates the Fickian limit, in which the MSD is given by 6*Dt*.

**Table 5.6** Self-diffusivity for acetonitrile and acetonitrile-$d_3$, along with a comparison to values from the literature.

| Property | Simulation (this work) | Experiment (literature or **this work**) |
|---|---|---|
| Self-diffusivity ($10^{-5}$ cm$^2$/s) | 3.79[a] | 4.12[b], 4.2[c], 4.3[d], 4.31[e], 4.34[f], 4.37[g,h], 4.7[i], 5.0[j], **4.24** |
| Self-diffusivity, ACN-$d_3$ ($10^{-5}$ cm$^2$/s) | 3.64[a] | 4.04[j], 4.14[l], **3.94** |

[a] Calculated via mean-squared displacement. [b] Determined in Ref. [94] from conductivity measurements. [c] Determined in Ref. [42] from quasielastic neutron scattering measurements. [d,e] Determined, respectively, in Refs. [95] and [96] from NMR spin echo measurements. [f] Determined in Ref. [97] via an open-ended capillary method. [g-l] Determined, respectively, in Refs. [98], [99], [43], [7], [100], and [98] from NMR spin-echo measurements.

The simulated vibrational density of states $g(\omega)$ was calculated for each atom, and for the center of mass, using

$$g(\omega) = \frac{1}{2\pi}\mathrm{Re}\left[\mathrm{FT}\left(C(\tau)\right)\right] \ , \tag{5.19}$$

where $C(\tau) = \langle v(0) \cdot v(\tau) \rangle$ is the velocity autocorrelation function. Figure 5.15 shows these velocity autocorrelation functions. For the calculation of the simulated vibrational density of states, only the first half of the velocity autocorrelation function was used, and the autocorrelation function was padded with zeros out to ~65 ps. A Savitzky-Golay filter was used to smooth the data. The GDOS was obtained by weighting the vibrational densities of states for each atomic site according to Eq. (5.7), using the neutron incoherent scattering cross sections. The low-frequency GDOS is shown in Figure 5.16(A). This region of the spectrum corresponds to intermolecular modes. The partial densities of states for each site and for the center of mass are shown in Figure 5.16(B). In the case of the center-of-mass vibrational density of states, the low-

frequency region reflects the influence of molecular tumbling, and thus can be regarded, in a sense, as a single-molecule analog to the low-frequency Raman spectrum. In Figure 5.16(A), we also show the density of states as obtained from inelastic neutron scattering; these data will be discussed in detail in Section 5.3.2.2. In the simulated data, modes due to the intramolecular part of the force field appear at higher frequencies, as shown in Figure 9(B). Table 5.2 lists the modes and their assignments. We also performed a normal-mode analysis along the molecular axis, using the force constants reported in Ref. [68] along with a unified methyl group. This analysis was found to give similar frequencies for the CT-YC and YC-YN stretches.

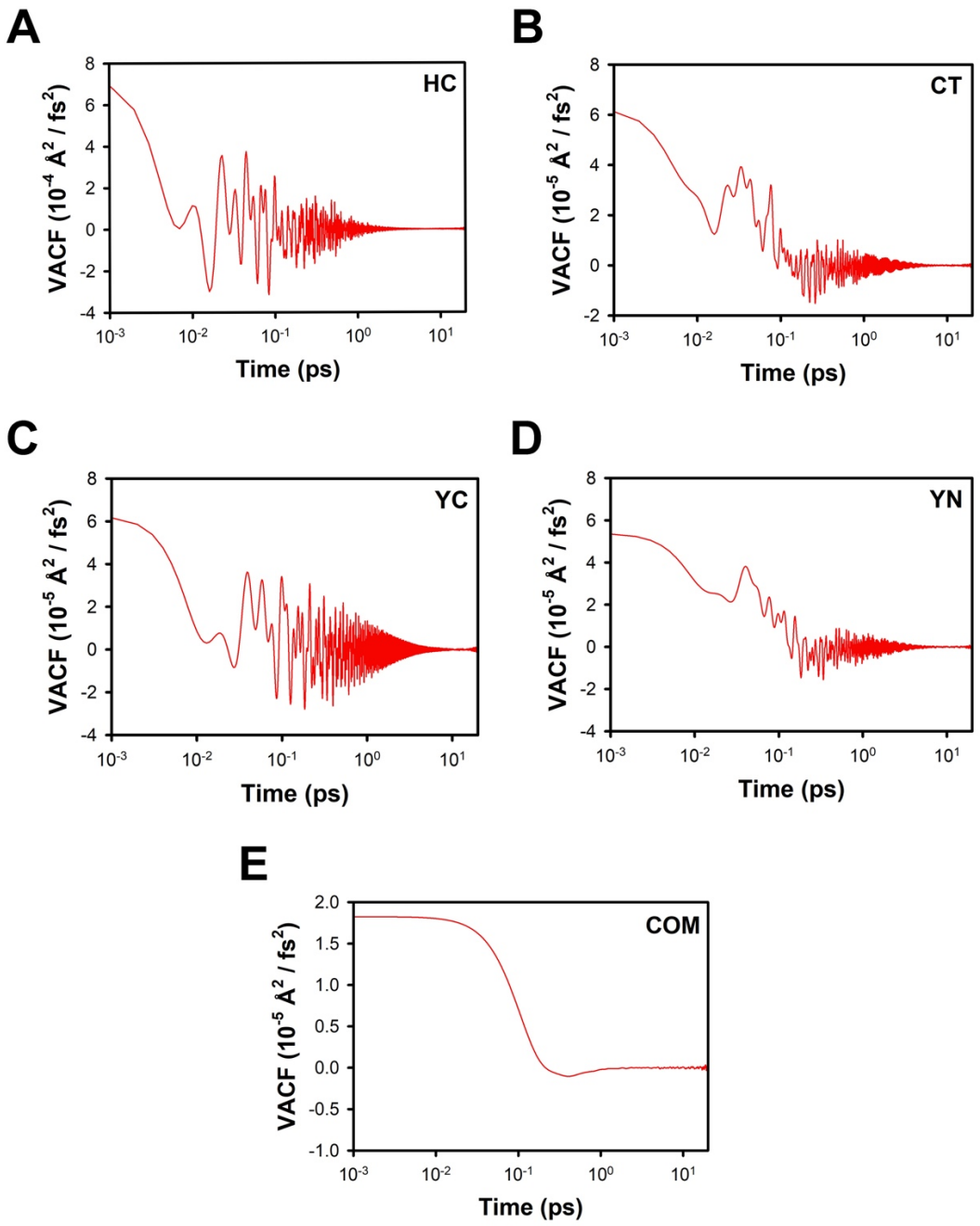


**Figure 5.15** Acetonitrile velocity autocorrelation functions for (A) HC, (B) CT, (C) YC, (D) YN, and (E) the center of mass.

**Table 5.7** Type of intramolecular mode and corresponding experimental frequency. The approximate frequencies of the modes in the model are also given.

| Mode | Experiment[a] ($cm^{-1}$) | Simulation ($cm^{-1}$) | Degeneracy |
|---|---|---|---|
| CCN bend | 379 | 631 | 2 |
| CC stretch | 917 | 832 | 1 |
| $CH_3$ rock | 1040 | 956 | 2 |
| CH bend | 1372 | 1318 | 1 |
| CH bend | 1440 | 1388 | 2 |
| CN stretch | 2253 | 1722 | 1 |
| CH stretch | 2943 | 2921 | 1 |
| CH stretch | 3003 | 3036 | 2 |

[a] Ref. [40].

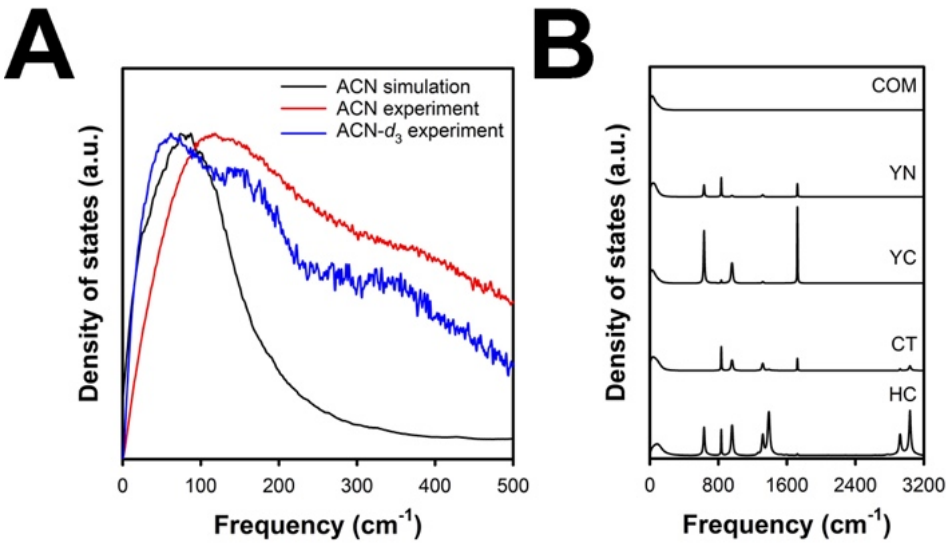


**Figure 5.16** (A) Low-frequency region of the simulated generalized density of states for ACN, along with an overlay of the experimental, height-normalized inelastic neutron spectra for ACN and ACN-$d_3$. (B) Full spectra of the simulated vibrational density of states for ACN calculated with respect to the molecule center of mass (COM, top spectrum) and for each atomic site on the molecule. The densities of states are offset vertically for clarity.

We investigated the pairing lifetime for both the antiparallel and head-to-tail configurations, as defined in Section 5.3.1.1. WE employed the formalism of Impey *et al.*,[101] in which the mean first passage time[102] is used to calculate $\Psi(t)dt$, the probability that a molecule remains paired at a time $t$ after being paired at a time $t$ =

0.[103,104] As proposed by Impey *et al.*,[101] we introduce a tolerance time $\tau^*$, that allows two molecules to be unpaired for a time $\tau^*$. In other words, if the molecules unpair for a shorter time than $\tau^*$ but are paired both before and after, then these molecules are still considered as having remained paired. $\Psi(t,\tau^*)dt$ is the probability that a molecule remains continuously paired to any molecule at a time *t* after being paired at a time *t* = 0. As discussed by Laage and Hynes,[105] transition-state theory is a more robust tool for determining pairing times, as the approach used here is $\tau^*$-dependent. The $\tau^*$ approach is however sufficient to investigate the phenomena in which we are interested, particularly because our neutron scattering experiments have a time resolution of ~1 ps. Thus, $\tau^*$ = 1 ps is ideal for comparison of our simulations with our experimental data.

Figure 5.17 shows $\Psi(t,\tau^*)$ for both antiparallel and head-to-tail configurations for different $\tau^*$. It is clear that the typical antiparallel pairing time is shorter than the head-to-tail pairing time. This observation is consistent with the histogram in Figure 5.13, which indicates that the population of head-to-tail pairs is larger than that of antiparallel pairs. A molecule in a head-to-tail pair has a longer pairing lifetime because it has many nearest neighbors with which it may pair in this configuration. As $\tau^*$ increases, we find that the majority of molecules that participate in head-to-tail pairs remain paired almost continuously. In contrast, for molecules participating in antiparallel pairs, even when the value of $\tau^*$ is large, the pair lifetime is considerably shorter than that for head-to-tail pairs.

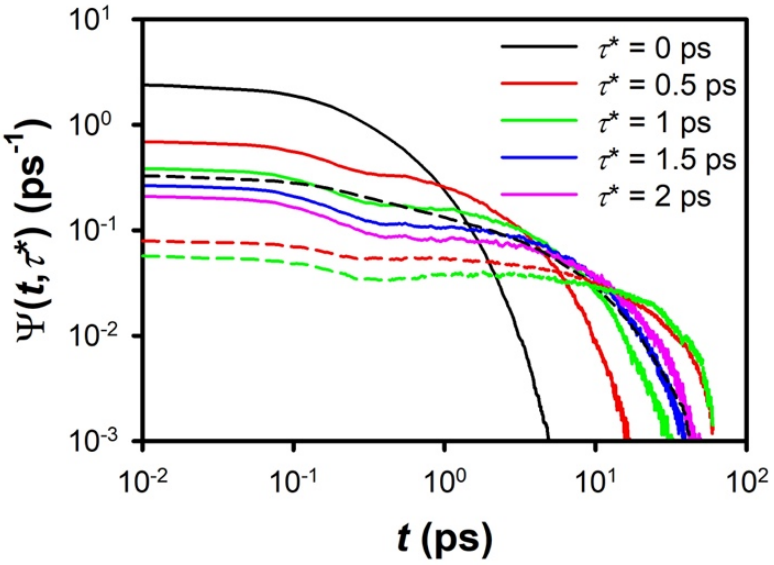


**Figure 5.17** Mean first passage times for molecules in pairs, calculated following the methodology of Impey *et al*.[101] The solid lines correspond to antiparallel pairs and the dashed lines correspond to head-to-tail pairs. The curves are color-coded by the tolerance time $\tau^*$; note that results are only shown for head-to-tail pairs out to $\tau^*$ = 1 ps.

### 5.3.2.2. Neutron scattering

Neutron scattering data for ACN and ACN-$d_3$ provide complementary information, due to the different neutron scattering cross sections of hydrogen and deuterium. In particular, because of the large incoherent cross section of hydrogen, the spectrum of ACN is dominated by information on the individual dynamics of hydrogen, i.e., the methyl group.

**Neutron GDOS.** The generalized densities of states extracted from neutron scattering measurements are shown in Figure 5.16(A). The most striking feature is the intensity and width of the low-frequency region, extending up to 500 cm$^{-1}$. We assign this feature in the experimental neutron density of states to the intense scattering from the methyl group, arising from librational motion and broadened by multiphonon contributions,

eventually convolved with the translational dynamics. For the deuterated sample, the intensity between 150 and 300 $cm^{-1}$ also suffers from imperfect subtraction of the empty cell in this region (DOS of aluminum, see Figure 5.18). The small bump at 390 $cm^{-1}$ in the ACN-$d_3$ spectrum corresponds to the IR- and Raman-active CCN bending mode,[40] which does not have a strong intensity in inelastic neutron scattering.

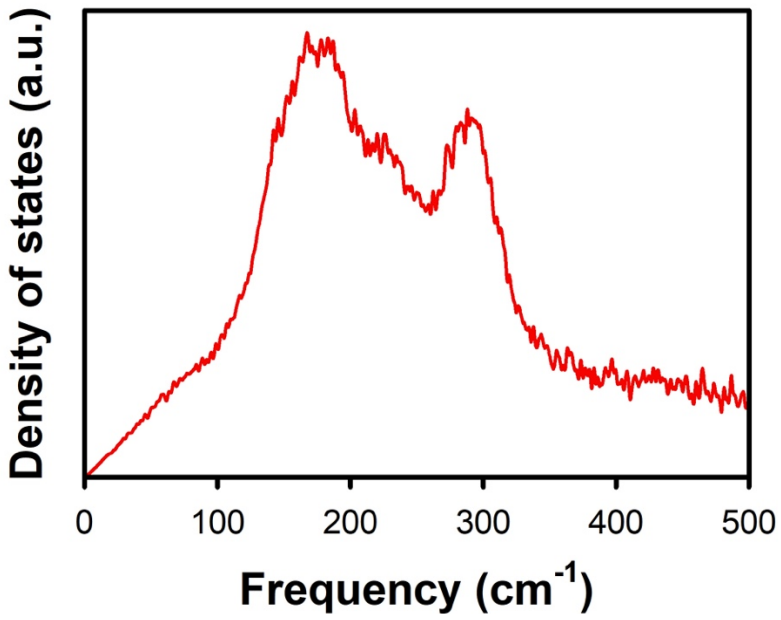


**Figure 5.18** Spectrum for the aluminum that was used as the cell for the inelastic neutron-scattering experiments. The intensity of the spectra for ACN and ACN-$d_3$ is affected by imperfect subtraction of the features in the aluminum data between 150 and 300 $cm^{-1}$.

**QENS**. The quasielastic signal gives insight into diffusional dynamics. As shown in Figure 5.19, the spectra at different $q$ values are well reproduced by our simulations. Our first analysis of the experimental data was based on a model composed of two Lorentzian contributions, without making any specific hypothesis about the diffusive dynamics. The widths of the two contributions for ACN and ACN-$d_3$ are shown in

Figure 5.20. Figure 5.20(A) shows a clear translational contribution, with the width linearly varying with $q^2$, whereas Figure 5.20(B) shows broad contributions with a mixed localized and translational character. Both types of dynamics in ACN-$d_3$ are slowed down at momentum values approaching the maximum of the structure factor, a typical effect observed in coherent neutron scatterers that is described as de Gennes narrowing.[106] A more refined model was therefore proposed based on two isotropic rotational contributions, convolved by the same translational dynamics, and modeled by a jump diffusion behavior. We constrained the rotational radii to 1.03 and 1.9 Å, corresponding, respectively, to the spinning and tumbling of the molecule. The de Gennes narrowing was taken into account by constraining $D_T$ of the deuterated compound to follow the modulation of the structure factor, according to the relation

$$\Gamma_T = \frac{D_T q^2}{1+\tau D_T q^2} \frac{1}{S(q)} \quad . \tag{5.20}$$

Using this framework, We were able to extract the translational and rotational diffusion coefficients, residence times $\tau_{res}$, and spinning and tumbling times $\tau_{spin}$ and $\tau_{tumbling}$, respectively (Table 5.3). The spinning mode has a short characteristic time (~0.2-0.3 ps), which is in agreement with previous QENS[42] and NMR[107] studies. The tumbling mode has a longer characteristic time (1.6-2 ps), which also is in agreement with previous spectroscopic work.[41] We also fitted the simulated $S(q,\omega)$ with the same model. Constraining the translational diffusion coefficient to $3.79 \times 10^{-5}$ cm$^2$/s, as extracted from the MSD, and the rotational radius as 1.03 Å and 1.9 Å from the experimental data, We find rotational constants of $1.79 \pm 0.07$ and $0.26 \pm 0.02$ ps$^{-1}$ for the tumbling and spinning motions, respectively, in excellent agreement with the values

extracted from the experimental spectra. We should note that We could not find any experimental evidence for the dynamics of the dimers.

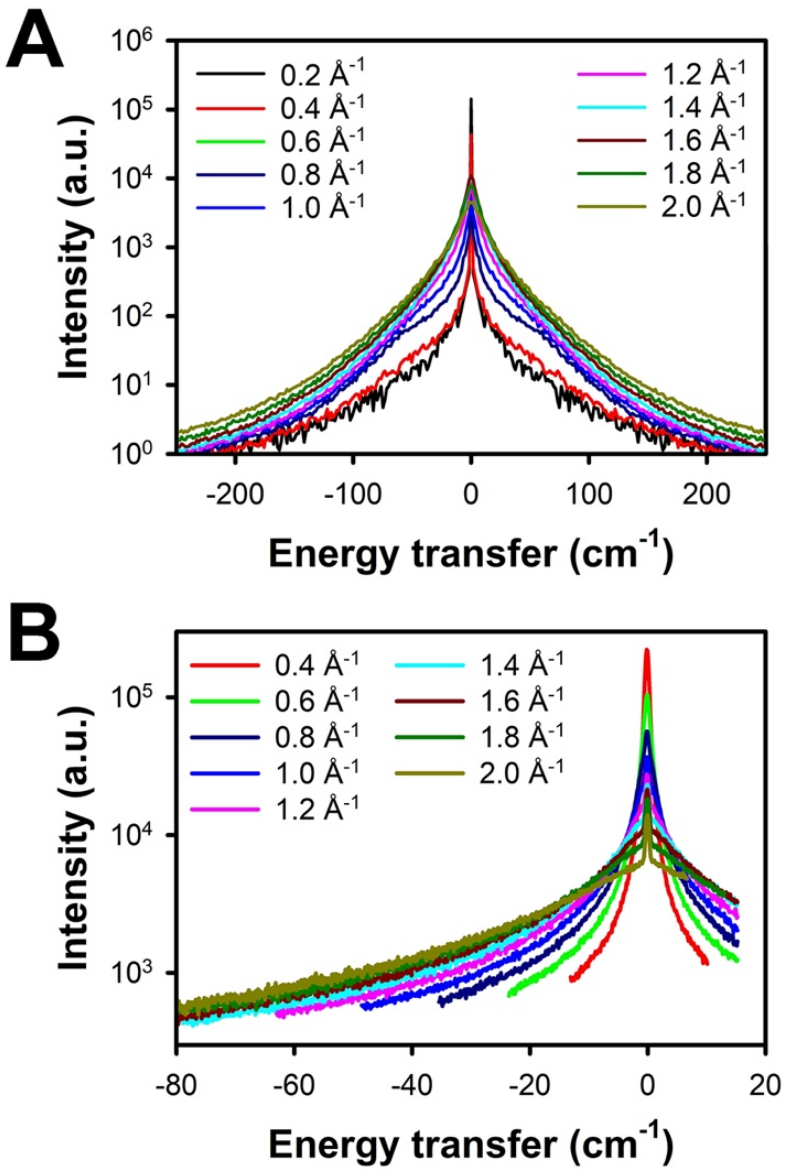


**Figure 5.19** $S(q,\omega)$ as a function of energy transfer $\omega$ for ACN obtained from (A) molecular dynamics simulations and (B) quasielastic neutron scattering. The legends indicate the different values of $q$ that were used. The quasielastic neutron scattering experiments were performed on LET (at ISIS, UK) with an incident energy $E_{we} = 2.83$ meV.

**Table 5.8** Translational diffusion coefficients $D_T$, rotational diffusion coefficients for tumbling $D_{rot,tumbling}$ and spinning $D_{rot,spin}$, along with residence times $\tau_{res}$, and spinning and tumbling times $\tau_{spin}$ and $\tau_{tumbling}$, respectively, for both acetonitrile and acetonitrile-$d_3$.

| Species | $D_T$ ($10^{-5}$ cm$^2$/s) | $D_{rot,tumbling}$ (ps$^{-1}$) | $D_{rot,spin}$ (ps$^{-1}$) | $\tau_{res}$ (ps) | $\tau_{tumbling}$ (ps) | $\tau_{spin}$ (ps) |
|---|---|---|---|---|---|---|
| ACN | 4.24 ± 0.3 | 0.26 ± 0.03 | 1.77 ± 0.1 | 0.42 ± 0.1 | 1.94 ± 0.02 | 0.29 ± 0.02 |
| ACN-$d_3$ | 3.94 ± 0.4 | 0.3 ± 0.03 | 1.91 ± 0.15 | 0.42 ± 0.1 | 1.66 ± 0.01 | 0.26 ± 0.02 |

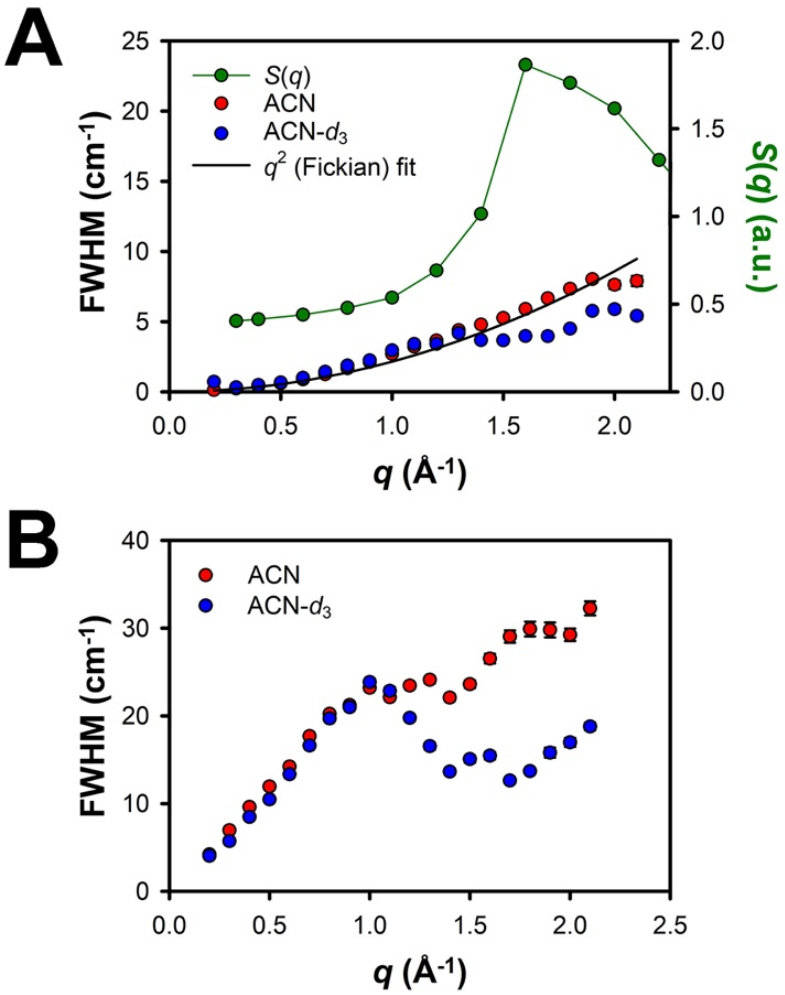


**Figure 5.20** (A) The QENS data from Figure 5.19(B) were analyzed with a sum of two Lorentzian contributions whose full-widths at half maximum (FWHMs) are shown on panels (A) and (B). (A) FWHM of the translational contribution, with the values for $D_s$(ACN) and $D_s$(ACN-$d_3$) as in Table 5.1. The data for ACN-$d_3$ exhibit de Gennes narrowing at $q$ ~ 1.6 Å$^{-1}$, which is at the maximum of the structure factor $S(q)$ (also shown for comparison). The fit is to the data for ACN. (B) The larger contribution is characteristic of a fast transition fitted with a jump-diffusion model, and is assigned to the coupling between translation and the rotation of the methyl groups.

## 5.4 *Discussion and Conclusions*

We have presented a detailed investigation of the structure and dynamics of bulk liquid ACN based on a combination of molecular simulation and neutron-scattering experiments. Our structural results obtained using molecular simulation reveal a complex organization in which molecules tend to form oriented dimers with their neighbors. Such marked pairing, which leads to characteristic pairing times that extend beyond the typical rotational and translational times, results from many-body interactions. Although the classic picture of pairing in ACN involves the antiparallel organization of neighboring cyano groups via dipole pairing, we find that antiparallel organization is best described as octupole pairing. Furthermore, head-to-tail pairing is an even more prevalent and robust motif. However, as discussed above, this head-to-tail pairing does not predominantly involve end-on interactions. Rather, the nitrogen atom of one molecule has a propensity to interact with the hydrogen atoms on the side of the methyl group of another molecule.

These results suggest that the microscopic organization of ACN is determined by a complex interplay among different structural motifs. ACN dimers in vacuum and in helium droplets are known to take on an antiparallel structure.[108] Free trimers are believed to be "liquid-like," whereas in helium droplets the preferred trimer structure consists of a dimer with an associated monomer.[108] The free tetramer has a structure composed of two perpendicular dimers ($S_4$ symmetry), whereas in a helium droplet the molecules form a ring with alternating dipole pairing ($D_{2d}$ symmetry).[108] In contrast, the common crystalline phases of acetonitrile are characterized by head-to-tail

interactions rather than antiparallel interactions,[93] as shown above. As in our simulations, the head-to-tail interactions are predominantly offset, rather than end-on. The strong contrast between the crystal structure and the cluster structure may reflect packing constraints, e.g., the inability to create a stable, 3D, space-filling structure whose main motif is octupole dipole pairing. A liquid is three-dimensional, but does not fill space in a regular pattern. From this perspective, it is perhaps not surprising that our simulations indicate that the liquid has elements of both the cluster and crystalline structure. We do observe a significant population of antiparallel dimers and trimers, but head-to-tail structures are considerably more prevalent.

Our pairing analysis of the antiparallel and head-to-tail motifs found in the bulk liquid shows that nearly all of the molecules are paired at any given time, and most of them are paired to more than one neighbor. Additionally, the antiparallel pairing lifetime – as defined using the formalism of mean first passage time while allowing for a short escape time in pairing – is shorter than the head-to-tail pairing lifetime. This finding, which is not unique to a particular choice of initial conditions, is consistent with the fact there are more head-to-tail paired molecules than antiparallel paired molecules. Our results can be understood based on the idea that head-to-tail dimers, unlike antiparallel dimers, do not experience any strong directional forces. The prominence of head-to-tail dimers is presumably an entropic effect, which further suggests that this feature is not unique to the force field used here.

Our findings highlight the ability of angularly-resolved radial distribution functions, $g(r,\theta)$, to provide a wealth of information about the organization of bulk liquid acetonitrile. Although this methodology has previously been used previously to

study microheterogeneities in simulations of ACN/water mixtures,[56] the angularly-resolved radial distribution functions in that work were not calculated with respect to the functional groups of ACN. Doing so can be expected to yield greater insight. In studies of the liquid at silica interfaces, applying the pairing analysis may also be helpful in teasing out details of the bilayer-like organization that forms in those systems.[46] In particular, using the angularly-resolved radial distribution functions and pairing analysis to study the population of tail-to-tail dimers at the silica interface is expected to reveal key details about the ACN bilayer.

## 5.5 *References*


1. Steiner, P. A.; Gordy, W. Precision Measurement of Dipole Moments and Other Spectral Constants of Normal and Deuterated Methyl Fluoride and Methyl Cyanide. *J. Mol. Spectrosc.* **1966**, *21*, 291−301.
2. McConvey, I. F.; Woods, D.; Lewis, M.; Gan, Q.; Nancarrow, P. The Importance of Acetonitrile in the Pharmaceutical Industry and Opportunities for its Recovery from Waste. *Org. Process Res. Dev.* **2012**, *16*, 612−624.
3. Yamada, Y.; Furukawa, K.; Sodeyama, K.; Kikuchi, K.; Yaegashi, M.; Tateyama, Y.; Yamada, A. Unusual Stability of Acetonitrile-Based Superconcentrated Electrolytes for Fast-Charging Lithium-Ion Batteries. *J. Am. Chem. Soc.* **2014**, *136*, 5039−5046.
4. Saum, A. M. Intermolecular Association in Organic Nitriles; the CN Dipole-pair Bond. *J. Polym. Sci.* **1960**, *42*, 57−66.
5. Saitô, H.; Tanaka, Y.; Nagata, S.; Nukada, K. $^{13}$C Nuclear Magnetic

Resonance Studies on Molecular Association. I. Self-Association of Dipolar Molecules. *Can. J. Chem.* **1973**, *51*, 2118−2123.

6. Kratochwill, A.; Weidner, J. U.; Zimmermann, H., Röntgenstrukturuntersuchung des flüssigen Acetonitrils. *Ber. Bunsenges. Phys. Chem.* **1973,** *77*, 408−425.
7. Kratochwill, A. $^{13}C$-$^{1}H$ Intermolecular Relaxation Rate and Molecular Pair Distribution Function in Liquid Acetonitrile *Ber. Bunsenges. Phys. Chem.* **1978**, *82*, 783−789.
8. Versmold, H. Depolarized Rayleigh Scattering: Reorientational Motion and Orientational Correlation in Acetonitrile and Carbon Disulfide. *Ber. Bunsenges. Phys. Chem.* **1978**, *82*, 451−457.
9. Bertagnolli, H.; Chieux, P.; Zeidler, M. D. A Neutron-Diffraction Study of Liquid Acetonitrile I. $CD_3C^{14}N$. *Mol.Phys.* **1976**, *32*, 759−773.
10. Bertagnolli, H.; Chieux, P.; Zeidler, M. D. A Neutron-Diffraction Study of Liquid Acetonitrile II. $CD_3C^{15}N$. *Mol. Phys.* **1976**, *32*, 1731−1736.
11. Bertagnolli, H.; Zeidler, M. D. Molecular Pair-Correlation Function of Liquid Acetonitrile from X-Ray and Neutron-Diffraction Studies. *Mol. Phys.* **1978**, *35*, 177−192.
12. Hsu, C. S.; Chandler, D. RISM Calculation of the Structure of Liquid Acetonitrile. *Mol. Phys.* **1978**, *36*, 215−224.
13. Fraser, K. J.; Dunn, L. A.; Morriss, G. P. An Integral Equation Study of Liquid Acetonitrile, *Mol. Phys.* **1987**, *61*, 775–782.
14. Chandler, D. Structure of Molecular Liquids. *Annu. Rev. Phys. Chem.* **1978**,

*29*, 441−471.

15. Maroncelli, M. Computer Simulations of Solvation Dynamics in Acetonitrile. *J. Chem. Phys.* **1991**, *94*, 2084−2103.
16. Steinhauser, O.; Bertagnolli, H. Molecular Pair Correlation Function of Liquid Acetonitrile Derived from Perturbation Theory with a Computer-Generated Reference Function. *Chem. Phys. Lett.* **1981**, *78*, 555–559.
17. Salamito, B.; Fries, P. H. Structure Factor Calculations for Molecular Liquids: Beyond the RISM Approximation. *Physica B* **1989**, *156–157*, 161–163.
18. Fries, P. H.; Richardi, J.; Krienke, H. Dielectric and Structural Results for Liquid Acetonitrile, Acetone and Chloroform from the Hypernetted Chain Molecular Integral Equation, *Mol. Phys.* **1997**, *90*, 841–854.
19. Richardi, J.; Fries, P. H.; Fischer, R.; Rast, S.; Krienke, H. J. Structure and Thermodynamics of Liquid Acetonitrile via Monte Carlo simulation and Ornstein-Zernike theories. *J. Mol. Liq.* **1997**, *73–74*, 465–485.
20. Böhm, J. B.; Lynden-Bell, R. M.; Madden, P. A.; McDonald, I. R. Molecular Motion in a Model of Liquid Acetonitrile. *Mol. Phys.* **1984**, *51*, 761−777.
21. Westlund, P.-O.; Lynden-Bell, R. M. A Molecular Dynamics Study of the Intermolecular Spin-Spin Dipole-Dipole Correlation Function of Liquid Acetonitrile. *J. Magn. Reson.* **1987**, *72*, 522−531.
22. Kovacs, H.; Kowalewski, J.; Laaksonen, A. Molecular Dynamics Simulation of Liquid Mixtures of Acetonitrile and Chloroform, *J. Phys. Chem.* **1990**, *94*, 7378−7385.
23. Ohba, T.; Ikawa, S. Molecular Dynamics Study of Local Structure and

Reorientational Dynamics in Liquid Acetonitrile. *Mol. Phys.* **1991**, *73*, 999−1010.

24. Radnai, T.; Jedlovszky, P. Reverse Monte Carlo Simulation of a Heteronuclear Molecular Liquid: Structural Study of Acetonitrile. *J. Phys. Chem.* **1994**, *98*, 5994−6002.
25. Terzis, A. F.; Samulski, E. T. Spatial Distribution Functions: Liquid $CH_3CN$ and $CO_2$, *Chem. Phys. Lett.* **1996**, *251*, 157–163.
26. Mountain, R. D. Shear Viscosity and Dielectric Constant of Liquid Acetonitrile. *J. Chem. Phys.* **1997**, *107*, 3921−3923.
27. Hirata, Y. Molecular Dynamics Simulation Study of the Rotational and Translational Motions of Liquid Acetonitrile. *J. Phys. Chem. A* **2002**, *106*, 2187−2191.
28. Gerig, J. T. Simulations of Nuclear Spin Relaxation in Liquid Acetonitrile. *Mol. Simul.* **2012**, *38*, 1085−1093.
29. Pothoczki, S.; Pusztai, L. Intermolecular Orientations in Liquid Acetonitrile: New Insights Based on Diffraction Measurements and All-Atom Simulations. *J. Mol. Liq.* **2017**, *225*, 160−166.
30. Evans, M. Molecular Dynamics and Structure of Liquid Acetonitrile – A Review and Computer Simulation. *J. Mol. Liq.* **1983**, *25*, 149–175.
31. Koverga, V. A.; Korsun, O. M.; Kalugin, O. N.; Marekha, B. A.; Idrissi, A. A New Potential Model for Acetonitrile: Insight into the Local Structure Organization. *J. Mol. Liq.* **2017**, *233*, 251−261.
32. Jorgensen, W. L.; Briggs, J. M. Monte Carlo Simulations of Liquid

Acetonitrile with a Three-Site Model. *Mol. Phys.* **1988**, *63*, 547−558.

33. Edwards, D. M. F.; Madden, P. A.; McDonald, I. R. A Computer Simulation Study of the Dielectric Properties of a Model of Methyl Cyanide: I. The Rigid Dipole Case. *Mol. Phys.* **1984**, *51*, 1141−1161.
34. Böhm, J. B.; McDonald, I. R.; Madden, P. A. An Effective Pair Potential for Liquid Acetonitrile. *Mol. Phys.* **1983**, *49*, 347−360.
35. Gee, P. J.; van Gunsteren, W. F. Acetonitrile Revisited: A Molecular Dynamics Study of the Liquid Phase. *Mol. Phys.* **2006**, *104*, 477–483.
36. Langer, H.; Versmold, H. Depolarized Rayleigh Scattering: Orientational Correlation Functions of Acetonitrile and Carbon Disulfide. *Ber. Bunsenges. Phys. Chem.* **1979,** *83*, 510−517.
37. Yuan, P.; Schwartz, M. Molecular Reorientation in Acetonitrile: A Comparison of Diffusion Coefficients from Raman Bandshapes and Nuclear Magnetic Resonance Relaxation Times. *J. Chem. Soc. Faraday Trans.* **1990**, *86*, 593−596.
38. McMorrow, D.; Lotshaw, W. T. Intermolecular Dynamics of Acetonitrile Probed with Femtosecond Fourier Transform Raman Spectroscopy. *J. Phys. Chem.* **1991**, *95*, 10395−10406.
39. Giorgini, M. G.; Morresi, A.; Mariani, L.; Cataliotti, R. S. Molecular Reorientation in Liquid Acetonitrile Studied by Depolarized Light Scattering Experiments. *J. Raman Spectrosc.* **1995**, *26*, 601–605.

40. Deàk, J. C.; Iwaki, L. K.; Dlott, D. D. Vibrational Energy Redistribution in Polyatomic Liquids: Ultrafast IR-Raman Spectroscopy of Acetonitrile. *J. Phys. Chem. A* **1998**, *102*, 8193−8201.

41. Loughnane, B. J.; Scodinu, A.; Farrer, R. A.; Fourkas, J. T. Exponential Intermolecular Dynamics in Optical Kerr Effect Spectroscopy of Small-Molecule Liquids. *J. Chem. Phys.* **1999**, *111*, 2686–2694.

42. Kunz, W.; Calmettes, P.; Bellissent-Funel, M.-C. Dynamics of Liquid Acetonitrile at High Frequencies. *J. Chem. Phys.* **1993**, *99*, 2079−2082.

43. Zeidler, M. D. A Comparative Study of Quasielastic Neutron Scattering and NMR Relaxation in Liquid Acetonitrile. *Ber. Bunsenges. Phys. Chem.* **1971**, *75*, 769−776.

44. Hu, Z.; Weeks, J. D. Acetonitrile at Silica Surfaces and at Its Liquid-Vapor Interface: Structural Correlations and Collective Dynamics. *J. Phys. Chem. C* **2010**, *114*, 10202–10211.

45. Ding, F.; Hu, Z.; Zhong, Q.; Manfred, K.; Gattass, R. R.; Brindza, M. R.; Fourkas, J. T.; Walker, R. A.; Weeks, J. D. Interfacial Organization of Acetonitrile: Simulation and Experiment. *J. Phys. Chem. C* **2010**, *114*, 17651–17659.

46. Berne, B. J.; Fourkas, J. T.; Walker, R. A.; Weeks, J. D. Nitriles at Silica Interfaces Resemble Supported Lipid Bilayers. *Acc. Chem. Res.* **2016**, *49*, 1605–1613.

47. Loughnane, B. J.; Farrer, R. A.; Scodinu, A.; Fourkas, J. T. Dynamics of a Wetting Liquid in Nanopores: An Optical Kerr Effect Study of the Dynamics

of Acetonitrile Confined in Sol-Gel Glasses. *J. Chem. Phys.* **1999**, *111*, 5116–5123.

48. Yamaguchi, T.; Yoshida, K.; Smirnov, P.; Takamuku, T.; Kittaka, S.; Takahara, S.; Kuroda, Y.; Bellissent-Funel, M.-C. Structure and Dynamic Properties of Liquids Confined in MCM-41 Mesopores. *Eur. Phys. J. Spec. Top.* **2007**, *141*, 19–27.
49. Cheng, L.; Morrone, J. A.; Berne, B. J. Structure and Dynamics of Acetonitrile Confined in a Silica Nanopore. *J. Phys. Chem. C* **2012**, *116*, 9582–9593.
50. Milischuk, A. A.; Ladanyi, M. Polarizability Anisotropy Relaxation in Nanoconfinement: Molecular Simulation Study of Acetonitrile in Silica Pores. *J. Phys. Chem. B* **2013**, *117*, 15729–15740.
51. Thompson, W. H. Structure, Dynamics, and Hydrogen Bonding of Acetonitrile in Nanoscale Silica Pores. *Mol. Simul.* **2015**, *41*, 788–794.
52. Kovacs, H.; Laaksonen, A. Molecular Dynamics Simulation and NMR Study of Water-Acetonitrile Mixtures. *J. Am. Chem. Soc.* **1991**, *113*, 5596–5605.
53. Bergman, D. L.; Laaksonen, A. Topological and Spatial Structure in the Liquid-Water-Acetonitrile Mixture. *Phys. Rev. E* **1998**, *58*, 4706–4715.
54. Takamuku, T.; Tabata, M.; Yamaguchi, A.; Nishimoto, J.; Kumamoto, M.; Wakita, H.; Yamaguchi, T. Liquid Structure of Acetonitrile-Water Mixtures by X-ray Diffraction and Infrared Spectroscopy. *J. Phys. Chem. B* **1998**, *102*, 8880–8888.

55. Mountain, R. D. Molecular Dynamics Study of Water-Acetonitrile Mixtures. *J. Phys. Chem. A* **1999**, *103*, 10744–10748.

56. Oldiges, C.; Wittler, K.; Tönsing, T.; Alijah, A. MD Calculated Structural Properties of Clusters in Liquid Acetonitrile/Water Mixtures with Various Contents of Acetonitrile. *J. Phys. Chem. A* **2002**, *106*, 7147−7154.

57. Mountain, R. D. Microstructure and Hydrogen Bonding in Water-Acetonitrile Mixtures. *J. Phys. Chem. B* **2010**, *114*, 16460–16464.

58. Melnikov, S. M.; Höltzel, A.; Seidel-Morgenstern, A.; Tallarek, U. Composition, Structure, and Mobility of Water-Acetonitrile Mixtures in a Silica Nanopore Studied by Molecular Dynamics Simulations. *Anal. Chem.* **2011**, *83*, 2569–2575.

59. Mountain, R. D. Molecular Dynamics Simulation of Water-Acetonitrile Mixtures in a Silica Slit. *J. Phys. Chem. C* **2013**, *117*, 3923–3929.

60. Melnikov, S. M.; Höltzel, A.; Seidel-Morgenstern, A.; Tallarek, U. Adsorption of Water-Acetonitrile Mixtures to Model Silica Surfaces. *J. Phys. Chem. C* **2013**, *117*, 6620–6631.

61. Rivera, C. A.; Bender, J. S.; Manfred, K.; Fourkas, J. T. Persistence of Acetonitrile Bilayers at the Interface of Acetonitrile/Water Mixtures with Silica. *J. Phys. Chem. A* **2013**, *117*, 12060–12066.

62. Wang, Y.-P.; Ren, K.; Liu, S. The Joint Effect of Surface Polarity and Concentration on the Structure and Dynamics of Acetonitrile Solution: A Molecular Dynamics Simulation Study. *Phys. Chem. Chem. Phys.* **2020**, *22*, 10322–10334.

63. Cabaleiro-Lago, E. M.; Ríos, M. A. Intermolecular Potential for Acetonitrile Based on ab Initio Calculations. *Mol. Phys.* **1999**, *96*, 309–321.

64. Grabuleda, X.; Jaime, C.; Kollman, P. A. Molecular Dynamics Simulation Studies of Liquid Acetonitrile: New Six-Site Model. *J. Comput. Chem.* **2000**, *21*, 901−908.

65. Guàrdia, E.; Pinzón, R.; Casulleras, J.; Orozco, M.; Luque, F. J. Comparison of Different Three-Site Interaction Potentials for Liquid Acetonitrile. *Mol. Simul.* **2001**, *26*, 287–306.

66. Price, M. L. P.; Ostrovsky, D.; Jorgensen, W. L. Gas-Phase and Liquid-State Properties of Esters, Nitriles, and Nitro Compounds with the OPLS-AA Force Field. *J. Comput. Chem.* **2001**, *22*, 1340−1352.

67. Wick, C. D.; Stubbs, J. M.; Rai, N.; Siepmann, J. I. Transferable Potentials for Phase Equilibria. 7. Primary, Secondary, and Tertiary Amines, Nitroalkanes and Nitrobenzene, Nitriles, Amides, Pyridine, and Pyrimidine. *J. Phys. Chem. B* **2005**, *109*, 18974−18982.

68. Nikitin, A. M.; Lyubartsev, A. P. New Six-Site Acetonitrile Model for Simulations of Liquid Acetonitrile and Its Aqueous Mixtures. *J. Comput. Chem.* **2007**, *28*, 2020−2026.

69. Albertí, M.; Amat, A. De Angelis, F.; Pirani, F. A Model Potential for Acetonitrile: from Small Clusters to Liquid. *J. Phys. Chem. B* **2013**, *117*, 7065−7076.

70. Deublein, S.; Metzler, P.; Vrabec, J.; Hasse, H. Automated Development of Force Fields for the Calculation of Thermodynamic Properties: Acetonitrile as a Case Study. *Mol. Simul.* **2013**, *39*, 109−118.

71. Alvarez, H. A.; Llerena Suster, C.; McCarthy, A. N. Consistent Acetonitrile Molecular Models for Both Standard and Computationally Efficient Molecular Dynamics Studies. *Asian J. Comp. Inf. Syst.* **2014**, *2*, 49−62.

72. Orhan, M. Dielectric and Transport Properties of Acetonitrile at Varying Temperatures: A Molecular Dynamics Study. *Bull. Kor. Chem. Soc.* **2014**, *35*, 1469−1478.

73. Kowsari, M. H.; Tohidifar, L. Systematic Evaluation and Refinement of Existing All-Atom Force Fields for the Simulation of Liquid Acetonitrile. *J. Comput. Chem.* **2018**, *39*, 1843−1853.

74. Hernández-Cobos, J.; Martínez, J. M.; Pappalardo, R. R.; Ortega-Blake, I.; Sánchez Marcos, E. A General Purpose Acetonitrile Interaction Potential to Describe Its Liquid, Solid and Gas Phases. *J. Mol. Liq.* **2020**, *318*, 113975.

75. Plimpton, S. Fast Parallel Algorithms for Short-Range Molecular Dynamics. *J. Comput. Phys.* **1995**, *117*, 1−19.

76. Martínez, L.; Andrade, R.; Birgin, E. G.; Martínez, J. M. PACKMOL: A Package for Building Initial Configurations for Molecular Dynamics Simulations. *J. Comput. Chem.* **2009**, *30*, 2157−2164.

77. Frenkel, D.; Smit, B. *Understanding Molecular Simulation: From Algorithms to Applications*, 2nd ed.; Academic Press: London, 2002.

78. Arnold, O.; Bilheux, J. C.; Borreguero, J. M.; Buts, A.; Campbell, S. I.; Chapon, L.; Doucet, M.; Draper, N.; Ferraz Leal, R.; Gigg, M. A.; Lynch, V. E.; Markvardsen, A.; Mikkelson, D. J.; Mikkelson, R. L.; Miller, R.; Palmen, K.; Parker, P.; Passos, G.; Perring, T. G.; Peterson, P. F.; Ren, S.; Reuter, M. A.; Savici, A. T.; Taylor, J. W.; Taylor, R. J.; Tolchenov, R.; Zhou, W.; Zikovsky, J. Mantid—Data Analysis and Visualization Package for Neutron Scattering and μ SR Experiments. *Nucl. Instrum. Methods Phys. Res. A* **2014**, *764*, 156−166.

79. Richard, D.; Ferrand, M.; Kearley, G. J. Analysis and Visualisation of Neutron-Scattering Data. *J. Neutron Res.* **1996**, *4*, 33−39.

80. Schober, H. An Introduction to the Theory of Nuclear Neutron Scattering in Condensed Matter. *J. Neutron Res.* **2014**, *17*, 109−357.

81. Schober, H.; Tölle, A.; Renker, B.; Heid, R.; Gompf, F. Microscopic Dynamics of $AC_{60}$ Compounds in the Plastic, Polymer, and Dimer Phases Investigated by Inelastic Neutron Scattering. *Phys. Rev. B* **1997**, *56*, 5937−5950.

82. Bée, M. *Quasielastic Neutron Scattering: Principles and Applications in Solid State Chemistry, Biology and Materials Science*; Adam Hilger: Bristol, 1988.

83. Keen, D. A. A Comparison of Various Commonly Used Correlation Functions for Describing Total Scattering. *J. Appl. Crystallogr.* **2001**, *34*, 172−177.

84. Hansen, J.-P.; McDonald, I. R. *Theory of Simple Liquids: with Applications to Soft Matter*, 4th ed.; Academic Press: London, 2013.

85. Elola, M. D.; Ladanyi, B. M. Molecular Dynamics Study of Polarizability Anisotropy Relaxation in Aromatic Liquids and Its Connection with Local Structure. *J. Phys. Chem. B* **2006**, *110*, 15525−15541.

86. Headen, T. F.; Howard, C. A.; Skipper, N. T.; Wilkinson, M. A.; Bowron, D. T.; Soper, A. K. Structure of $\pi$-$\pi$ Interactions in Aromatic Liquids. *J. Am. Chem. Soc.* **2010**, *132*, 5735−5742.

87. Raschke, T.; Levitt, M. Nonpolar Solutes Enhance Water Structure Within Hydration Shells while Reducing Interactions between Them. *Proc. Natl. Acad. Sci. U.S.A.* **2005**, *102*, 6777−6782.

88. Sarangi, S. S.; Zhao, W.; Müller-Plathe, F.; Balasubramanian, S. Correlation between Dynamic Heterogeneity and Local Structure in a Room-Temperature Ionic Liquid: A Molecular Dynamics Study of [bmim][$PF_6$]. *ChemPhysChem* **2010**, *11*, 2001−2010.

89. Linse, P.; Karlström, G. Dipolar Order in Molecular Fluids: II. Molecular Influence. *J. Stat. Phys.* **2011**, *145*, 418−440.

90. Jorgensen, W. L.; Maxwell, D. S.; Tirado-Rives, J. Development and Testing of the OPLS All-Atom Force Field on Conformational Energetics and Properties of Organic Liquids. *J. Am. Chem. Soc.* **1996**, *188*, 11225−11236.

91. Torquato, S. Statistical Description of Microstructures. *Annu. Rev. Mater. Res.* **2002**, *32*, 77−111.

92. Canongia Lopes, J. N. A.; Pádua, A. A. H. Nanostructural Organization in Ionic Liquids. *J. Phys. Chem. B* **2006**, *110*, 3330−3335.

93. Enjalbert, R.; Galy, J. $CH_3CN$: X-ray Structural Investigation of a Unique Single Crystal. $\beta \rightarrow \alpha$ Phase Transition and Crystal Structure. *Acta Crystallogr. B* **2002**, *58*, 1005−1010.

94. Hawlicka, E.; Grabowski, R.; Reimschüssel, W. Self-Diffusion and Conductance of Acetonitrile-Water Solutions of Tetraethylammonium Iodide. *Ber. Bunsenges. Phys. Chem.* **1990**, *94*, 158−162.

95. Hertz, H. G.; Leiter, H. Hydrophobic Interactions in Aqueous Mixtures of Methanol, Ethanol, Acetonitrile, and Dimethyl-Formamide. *Z. Phys. Chem. (Munich)* **1982**, *133*, 45−67.

96. Hurle, R. L.; Woolf, L. A. Self-Diffusion in Liquid Acetonitrile under Pressure. *J. Chem. Soc., Faraday Trans. 1* **1982**, *78*, 2233−2238.

97. Hawlicka, E. Acetonitrile-Water Solutions of Sodium Halides: Viscosity and Self-Diffusion of $CH_3CN$ and $H_2O$. *Z. Naturforsch.* **1988**, *43a*, 769−773.

98. Holz, M.; Mao, X.; Seiferling, D.; Sacco, A. Experimental Study of Dynamic Isotope Effects in Molecular Liquids: Detection of Translation-Rotation Coupling. *J. Chem. Phys.* **1996**, *104*, 669−679.

99. Connell, M. A.; Bowyer, P. J.; Adam Bone, P.; Davis, A. L.; Swanson, A. G.; Nilsson, M.; Morris, G. A. Improving the Accuracy of Pulsed Field Gradient NMR Diffusion Experiments: Correction for Gradient Non-Uniformity. *J. Magn. Reson.* **2009**, *198*, 121−131.

100. Kovacs, H.; Kowalewski, J.; Maliniak, A.; Stilbs, P. Multinuclear Relaxation and NMR-Self-Diffusion Study of the Molecular Dynamics in Acetonitrile-Chloroform Liquid Mixtures. *J. Phys. Chem.* **1989**, *93*, 962−969.

101. Impey, R. W.; Madden, P. A.; McDonald, I. R. Hydration and Mobility of Ions in Solution. *J. Phys. Chem.* **1983**, *87*, 5071−5083.

102. Redner, S. *A Guide to First-Passage Processes*, 1st ed.; Cambridge University Press: Cambridge, 2001.

103. Hartkamp, R.; Coasne, B. Structure and Transport of Aqueous Electrolytes: From Simple Halides to Radionuclide Ions. *J. Chem. Phys.* **2014**, *141*, 124508.

104. Cazade, P.-A.; Hartkamp, R.; Coasne, B. Structure and Dynamics of an Electrolyte Confined in Charged Nanopores. *J. Phys. Chem. C* **2014**, *118*, 5061−5072.

105. Laage, D.; Hynes, J. T. On the Residence Time for Water in a Solute Hydration Shell: Application to Aqueous Halide Solutions. *J. Phys. Chem. B* **2008**, *112*, 7697−7701.

106. Hugouvieux, V.; Farhi, E.; Johnson, M. R.; Juranyi, F.; Bourges, P.; Kob, W. Structure and Dynamics of *l*-Ge: Neutron Scattering Experiments and *ab initio* Molecular Dynamics Simulations. *Phys. Rev. B* **2007**, *75*, 104208.

107. Bopp, T. T. Magnetic Resonance Studies of Anisotropic Molecular Rotation in Liquid Acetonitrile-$d_3$. *J. Chem. Phys.* **1967**, *47*, 3621−3626.

108. Behrens, M.; Fröchtenicht, R.; Hartmann, M.; Siebers, J.-G.; Buck, U.; Hagemeister, F. C. Vibrational Spectroscopy of Methanol and Acetonitrile Clusters in Cold Helium Droplets. *J. Chem. Phys.* **1999**, *111*, 2436−2443.

# Chapter 6: Robustness of the Bilayer Structure in Acetonitrile at the Liquid/Silica Interface

Research designed by: John T. Fourkas and Benoit Coasne
Research conducted by: Samuel R. Cohen, John T. Fourkas, and Benoit Coasne
I did simulations and analyzed the data.

## 6.1 *Introduction*

Liquid acetonitrile (ACN) forms an interdigitated, bilayer-like structure at a silica surface.[1] Recent research has shown that in electrolyte solutions at this interface, an unexpected, concentration-dependent surface charge is present,[2] and that there is little to no effect of added salt on the organization, orientation, or electric field of the liquid. In this chapter, we discuss some preliminary results on interfacial ACN, in particular seeking to understand the robustness of the ACN bilayer with temperature and where flow occurs to help understand the electrolyte results.

## 6.2 *Computational and Experimental Methods*

### 6.2.1. Molecular Simulation

#### 6.2.1.1. Model

Liquid acetonitrile was simulated using the force field[3] described in Chapter 5 of this thesis. Figure 6.1(A) shows a representative configuration from a simulation of ACN at the liquid/vapor interface.

For the simulations involving hydroxylated silica, the Lennard-Jones (LJ) parameters and partial charges of the atoms were taken from the work of Lee and Rossky.[4] Figure 6.1(B) shows the crystalline silica substrate used in this work and the

partial charges and labels of the silanol atoms. The silica surface has a hydroxyl density of 4.50/nm$^2$, in agreement with previous work by Hu and Weeks.[5] All silicon and oxygen atoms in the silica were treated as fixed, with the oxygen in the silanol groups in the $z$ = 0 plane. The hydrogens were allowed to rotate freely by constraining the length of the O−H bond to be 1.0 Å. The harmonic Si−O−H bending potential is 109.27˚.

The mixed LJ interactions between all atoms were treated using the usual Lorentz-Berthelot combining rules, as described in Chapter 2. Figures 6.1(C) and 6.1(D) show representative configurations from simulations of ACN at the liquid/silica interface and confined in a silica slit-pore. For the simulations at the liquid/silica interface, a slab geometry was used with a repulsive wall located at $z$ = 100 Å and an additional 50 Å of vacuum that is not shown in the figure.

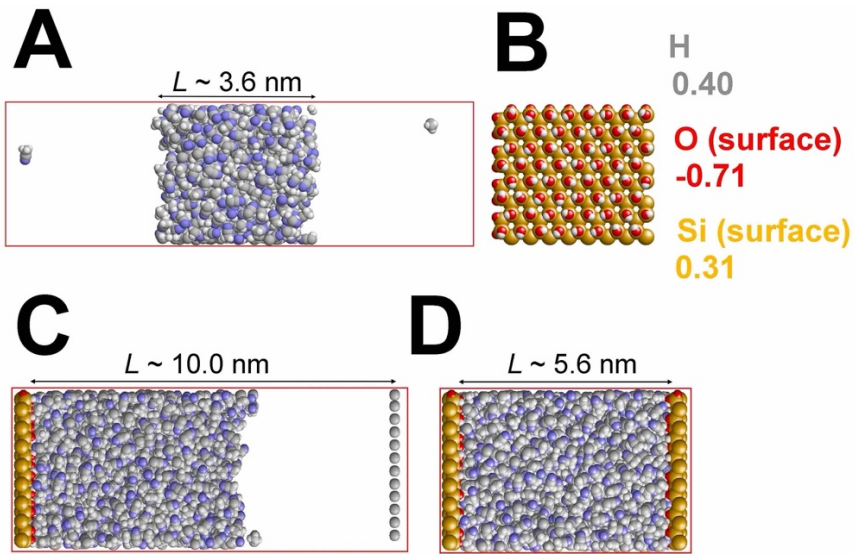


**Figure 6.1** (A) Representative molecular configuration at $T$ = 298 K for the liquid/vapor interface. (B) Top view of the hydroxylated silica substrate used in this work, showing the label and partial charge for the silanol atom types. Representative molecular configurations at $T$ = 298 K for (C) the liquid/silica interface and (D) a slit-pore. For each representative configuration, the red frames indicate the molecular simulation box used in the calculations.

### 6.2.1.2. Molecular Dynamics

Molecular dynamics simulations were performed in LAMMPS.[7] The equations of motion were integrated with a time step of 1 fs. All of the initial configurations were built using PACKMOL,[8] and the simulations were preceded by an energy minimization with an energy tolerance of $10^{-6}$.

The simulations for the bulk liquid were performed with 529 molecules in the isothermal/isobaric (*NPT*) ensemble in a box with periodic boundary conditions at temperatures ranging from 248 K to 348 K and a pressure of 1 bar. The systems were equilibrated for 200 ps using a Nosé-Hoover thermostat and barostat[9] with 30 fs and 1000 fs relaxation constants, respectively. Using the equilibrated systems, the simulations were then run in the *NPT* ensemble up to 2 ns. The simulations for the liquid/vapor systems (Figure 6.1(A)) used a 36 Å × 36 Å × 36 Å box of the liquid

extended in the *z*-direction (values of $L_z$ up to 836 Å were used to test for the presence of finite-size effects). These simulations were equilibrated in the *NVT* ensemble at 298 K for 200 ps using the same Nosé-Hoover thermostat as in the simulations of the bulk liquid. Using the equilibrated systems, the simulations were then run in the *NVE* ensemble up to 1 ns. Long-range Coulombic interactions were included using Ewald summation with a precision of $10^{-5}$. The cut-off distances for the Lennard-Jones interactions and the real-space part of the Ewald sum were both set to 14 Å.

For the simulations at the interface (Figure 6.1(C)), 864 ACN molecules were confined between a silica substrate and a repulsive wall in a 40.5368 Å × 35.1059 Å × 100 Å box. A slab geometry with periodic boundary conditions in the *x*- and *y*-dimensions was used. As mentioned above, there was an additional 50 Å of vacuum between $z = 100$ Å and $z = 150$ Å. For the slit-pore geometry (Figure 6.1(D)), 864 ACN molecules were confined between two silica surfaces with their silanol oxygen atoms separated by a *z*-distance of 56.09703 Å. Periodic boundary conditions were employed in the latter case. In the slab geometry, long-range Coulombic interactions were included using the particle-particle-particle mesh method with a precision of $10^{-5}$, whereas the simulations in the slit-pore geometry used the same Ewald sum parameters as described above. The cut-off distances for the Lennard-Jones interactions and the long-range solver were both set to 14 Å. A first slab simulation was run in the *NVT* ensemble for 1 ns at 348 K, then separate *NVT* simulations were performed at each temperature for 200 ps to equilibrate the systems. The production runs were 40 ns. This time was selected to obtain good statistics for the density profiles. For the slit-pore

geometry, the system was equilibrated at 298 K in the *NVT* ensemble for 300 ps. Production runs lasted 3 ns, also in the *NVT* ensemble.

## 6.3 *Results and Discussion*

### 6.3.1 Static Properties

#### 6.3.1.1. Interfacial Thermodynamics

To validate the performance of the ACN force field for interfacial properties, the bulk saturating vapor pressure was determined using a combination of Grand Canonical Monte Carlo (GCMC) and molecular dynamics (MD) simulations. First, starting from the coexisting gas/liquid acetonitrile system shown in Figure 6.1(C), GCMC simulations were performed at different chemical potentials $\mu$ at $T$ = 298 K. In these simulations, the system with a constant volume $V$ is placed in contact with an infinite reservoir of acetonitrile molecules at constant $\mu$ and $T$, so that the number of acetonitrile molecules is allowed to change. In this direct coexistence method applied to the Grand Canonical ensemble,[10] depending on the chemical potential $\mu$, the system will either evolve toward the gas phase or the liquid phase. If $\mu$ is above the chemical potential at saturation, $\mu_0$, all of the gas will transform into the liquid phase. On the other hand, for $\mu < \mu_0$, the liquid phase will evaporate. By performing such GCMC simulations for many chemical potentials, $\mu_0$ was estimated with an error bar smaller than a few percent. Second, starting from an empty simulation box, a GCMC simulation was performed to estimate the gas density at the gas/liquid coexistence condition for $T$ = 298 K, $\rho(\mu_0,T)$. In parallel, MD simulations in the isothermal/isobaric ensemble

(*NPT*) were performed for the gas phase at different pressures. This second set of simulations allowed us to estimate the gas density as a function of pressure, $\rho(P,T)$ (see Figure 6.2). The saturating vapor pressure $P_0$ was then estimated by finding the gas pressure for which $\rho(P_0,T) = \rho(\mu_0,T)$. For the 6-site acetonitrile model considered in this paper, $P_0$ was found to be equal to 17.9 kPa (see Table 6.1). Although this value is greater than the experimental value of ~12 kPa, it should be noted that such disagreement is not unusual for force fields that are not specifically developed to match this specific interfacial property. Finally, by performing separate MD simulations of the liquid and the gas at their determined densities at $P_0$, the heat of vaporization was calculated using the relation

$$\Delta H_{vap} = H_{gas} - H_{liquid} \,, \tag{6.1}$$

where $H = U + P_0V$ is the enthalpy, $U$ is the internal energy determined from the simulation, $P_0$ is the saturating vapor pressure determined previously, and $V$ is the volume of the simulation box. We found $\Delta H_{vap}$ =33.1 kJ/mol, which is in excellent agreement with the experimental value of 33.225 kJ/mol (Table 6.1).[11]

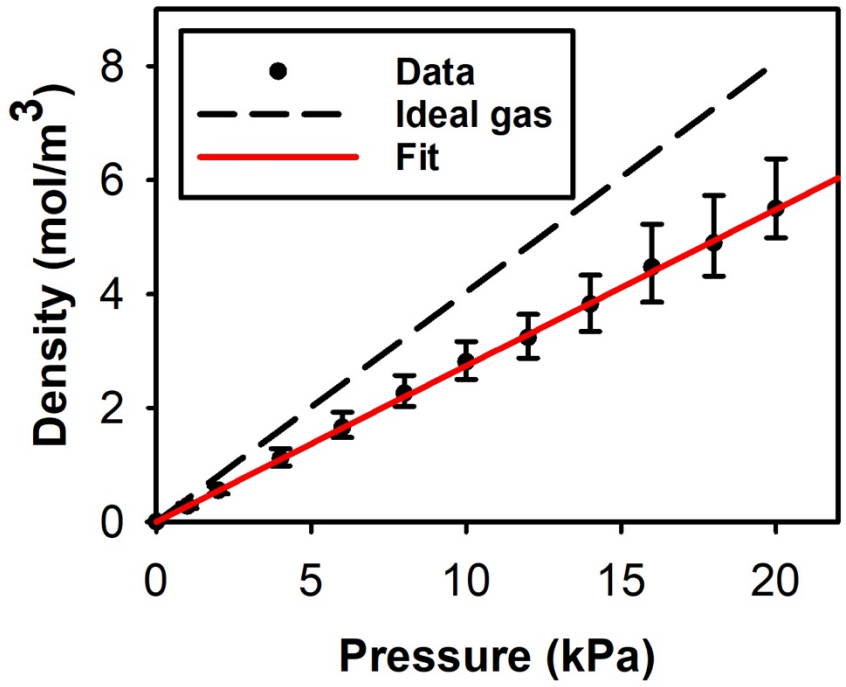


**Figure 6.2** Data from simulations in the isothermal/isobaric ensemble used to calculate the saturating vapor pressure. The linear fit is constrained to go through the origin. The error bars represent the 95% confidence levels.

To study the liquid/vapor interface, a liquid slab of ACN molecules in contact with the gas phase was simulated, as illustrated in Figure 6.1(C). The surface tension $\gamma$ for the liquid was calculated using the Kirkwood-Buff integral:

$$\gamma = \frac{1}{2}\int_0^{L_z}\left(\langle P_{zz}\rangle - \frac{1}{2}\left(\langle P_{xx}\rangle + \langle P_{yy}\rangle\right)\right)\mathrm{dz}\,, \tag{6.2}$$

where $\langle P_{zz}\rangle$ represents the ensemble average of the normal pressure, and $\frac{1}{2}\left(\langle P_{xx}\rangle + \langle P_{yy}\rangle\right)$ represents the ensemble average of the tangential pressure. The factor

½ in Eq. (6.2) takes into account the two interfaces in the system that arise from the use of periodic boundary conditions. These different contributions were calculated using the virial expression for the pressure tensor,[12]

$$PV = \sum_{i,a} m_{\mathrm{ia}} v_{\mathrm{ia}} v_{\mathrm{ia}} + \sum_{i,a} r_{\mathrm{ia}} f_{\mathrm{ia}} \,, \tag{6.3}$$

where the sum runs over each site *a* of each molecule *i*. Here, $m_{\mathrm{ia}}$, $v_{\mathrm{ia}}$, $r_{\mathrm{ia}}$ and $f_{ia}$ are the mass, velocity, position, and force, respectively, acting on site *a* of molecule *i*. To check that our surface-tension calculations were not affected by finite-size effects, different liquid slab thicknesses from 3.6 to 12.5 nm were considered. A typical example of the time evolution for the normal and tangential pressures, as well as the surface tension itself, are shown in Figure 6.3. The calculated value for the surface tension of 28.7 mJ/m$^2$ is in excellent agreement with the experimental value of 28.2 mJ/m$^2$ (Table 6.1).[13] It can be concluded, therefore, that even though our chosen force field[1] was not originally developed to treat such phenomena, interfacial behavior is reproduced well with this model.

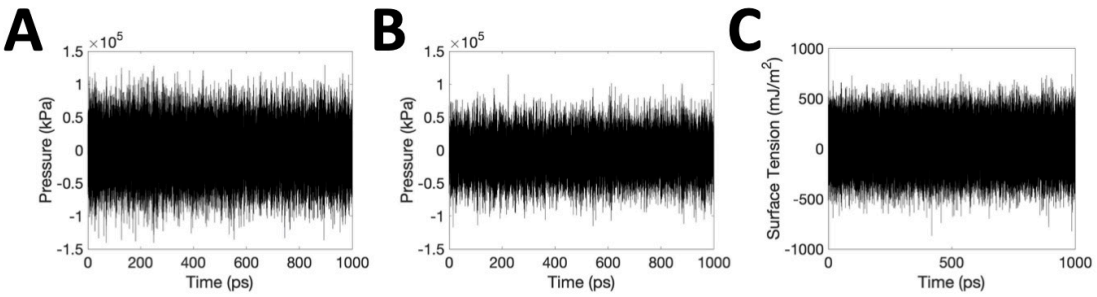


**Figure 6.3** (A) Normal pressure, (B) tangential pressure, and (C) surface tension for the gas/liquid interface with $L_z$ = 108 Å.

**Table 6.9** Some thermodynamic and transport properties for acetonitrile, along with a comparison to experimental values from the literature.

| Property | Simulation (this work) | Experiment (literature) |
|---|---|---|
| Surface tension (mJ/m$^2$) | 28.7 | 28.2[a] |
| Saturating vapor pressure $P_0$ (kPa) | 17.9 | 11.7[b], 12.5[c] |
| Liquid density at $P_0$ (g/cm$^3$) | 0.761 | 0.7795[c] |
| Gas density at $P_0$ (mol/m$^3$) | 4.9157 | 5.29[c] |
| Heat of vaporization (kJ/mol) | 33.1 | 33.225[d] |
| Viscosity (cP) | 0.307 | 0.333[e,f], 0.3358[g], 0.3369[h], 0.3417[i], 0.3426[j], 0.354[k], 0.3693[l], 0.370[m] |

[a] Ref. 13. [b] Determined from the semi-empirical Antoine equation of state published in Ref. 14. [c] Ref. 15. [d] Ref. 16. [e-m] Ref. 17.

### 6.3.1.2. Structure

To compare the structure of ACN at the liquid/silica interface with that of the bulk liquid, we calculated the angularly resolved radial distribution function $g_{\text{Me-Me}}(r, \theta)$ (Figure 6.4) for both systems. Calculation of this function with respect to the methyl-methyl distance enables us to look for evidence of the tail-to-tail dimers that might be expected to be dominant given the lipid-bilayer-like organization at the interface. Moreover, the effects of isotopic dilution on the symmetric methyl stretch at the interface is sensitive to the distance, strength, and relative orientation of the methyl transition dipole moments, facilitating a comparison between simulation and experiments that have been performed in our laboratory. For the interface, we restricted our analysis to pairs where both molecules were near the surface, as defined by the first minimum in the density profile with respect to the center-of-mass separation.[5] The bulk $g_{\text{Me-Me}}(r, \theta)$ was shown previously in Chapter 5 (Figure 5.8). As shown in the difference map (Figure 6.4), there are pronounced differences between $g_{\text{Me-Me}}(r, \theta)$ for the interface

and the bulk populations. In contrast to the interfacial system, the bulk liquid is dominated by offset, head-to-tail dimers (configuration 1). These results are in agreement with our findings discussed in Chapter 5. However, the difference map also reveals a tail-to-tail population in the bulk (configuration 2) that is not that common in the bulk, but is not present at all at the interface. The most common structures at the interface that are observed more often than in the bulk are parallel, offset dimers (configurations 3 and 4) that are roughly perpendicular to the silica. These dimers constitute each sublayer. There are also dimers that are arranged in an octupole-paired, antiparallel fashion (configurations 5 and 6) that constitute the interdigitated, first bilayer.

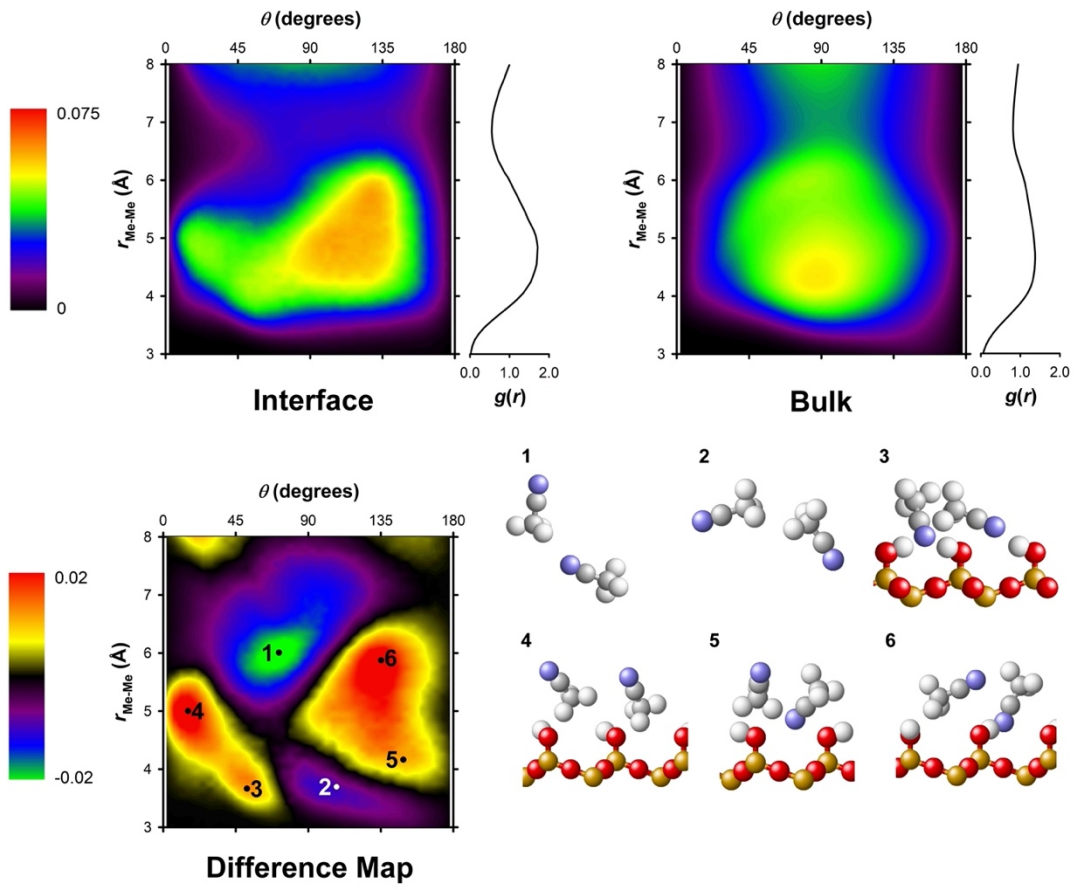


**Figure 6.4** Radial distribution functions and angularly resolved radial distribution functions for acetonitrile with respect to the methyl-methyl distance, with the angle $\theta$ defined as described in Chapter 5. The difference map between the angularly resolved radial distribution functions at the interface and the bulk is also given, along with representative configurations from the indicated regions.

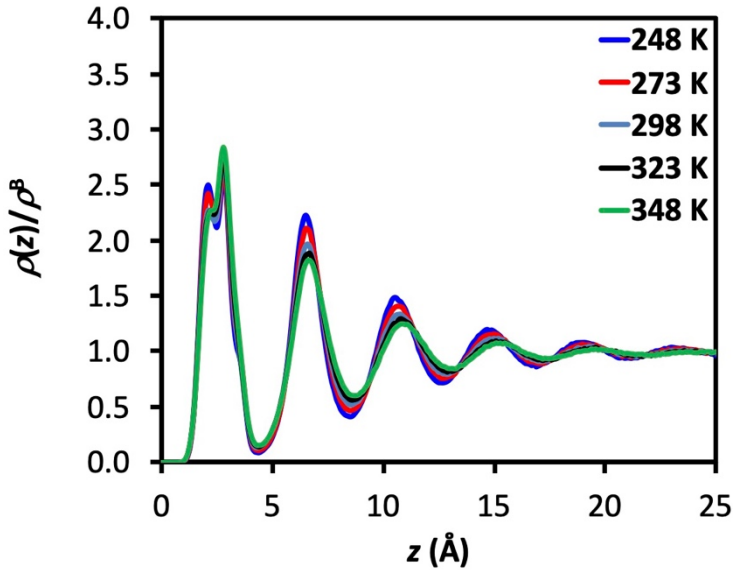


**Figure 6.5** Methyl-carbon density $\rho(z)$ of ACN as a function of distance from the interface, normalized to the corresponding bulk density $\rho^{B}(T)$ for each temperature.

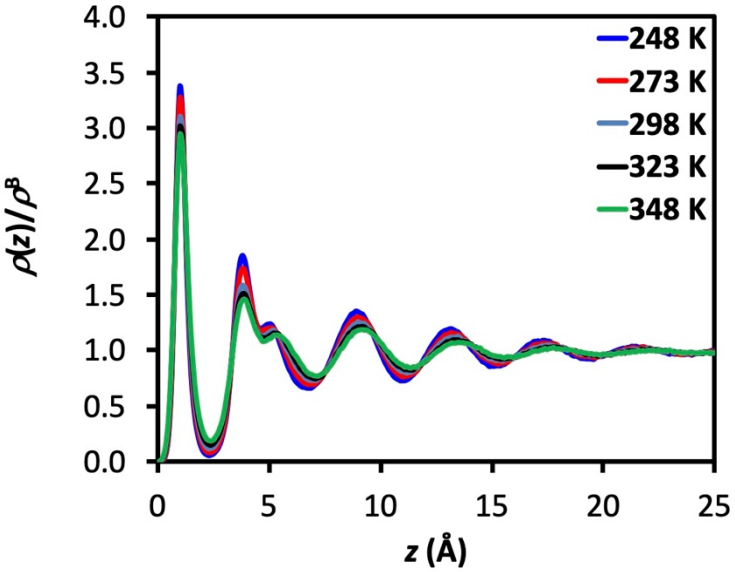


**Figure 6.6** Nitrogen density $\rho(z)$ of ACN as a function of distance from the interface for each temperature.

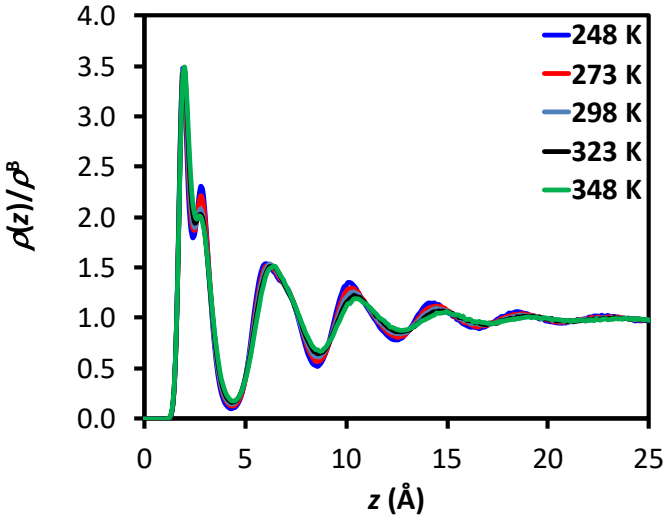


**Figure 6.7** Center-of-mass density $\rho(z)$ of ACN as a function of distance from the interface, normalized to the corresponding bulk density $\rho^{B}(T)$ for each temperature.

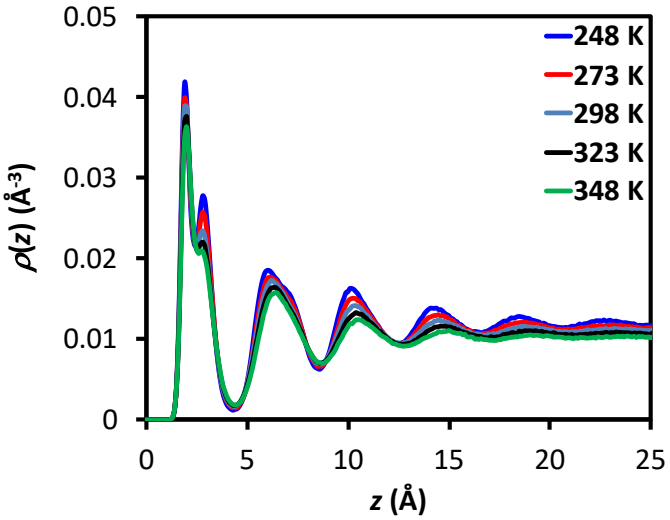


**Figure 6.8** Center-of-mass density $\rho(z)$ of ACN as a function of distance from the interface for each temperature.

The temperature-dependent organization of the bilayer structure was also investigated. Density profiles with respect to the methyl carbon and nitrogen are shown in Figures 6.5 and 6.6, respectively. As in the case of the bulk liquid (Chapter 5), only a single replica was used here, but our results for the $T$ = 298 K case are essentially

identical to previous work,[5,6] again suggesting stabilization of structural properties. The peak in the methyl-carbon profile (Figure 6.5) out to $z$ = 4.35 Å represents the first bilayer, whereas the peak in the nitrogen profile (Figure 6.6) represents the first sublayer of the first bilayer. Density profiles with respect to the center-of-mass separation are shown in Figure 6.7. Remarkably, the thickness of the first bilayer is nearly invariant with temperature. The bilayer organization is robust, persisting up to the boiling point (353 K, experimentally). The scaling with changing temperature is described almost entirely by the change in density of the bulk liquid (Figure 6.8). With increasing temperature, the size of the first bilayer barely changes at all, as is also shown by the orientational profiles in Figure 6.9. The temperature-dependent changes in density are reflected in the charge density profiles (Figure 6.10) showing a surprisingly significant decrease in the charge density in the first sublayer with increasing temperature. This decrease can be attributed to the changing density of the liquid, as seen in the unnormalized density profiles in Figure 6.8. In Figure 6.8, the large negative values for the charge density at $z \sim 2.57$ Å correspond to the nitrogen atoms of the molecules in the first sublayer, wheareas the pronounced peak at $z \sim 3.37$ Å corresponds to the interdigitated second sublayer. At low electrolyte concentrations, cations are known to occupy the exterior of the surface bilayer,[2] which should correspond to the negative region at $z \sim 6.1$ Å. At higher electrolyte concentrations, cations are known to partition to the silica surface,[2] which is expected to be near the negative region at $z \sim 2.57$ Å.

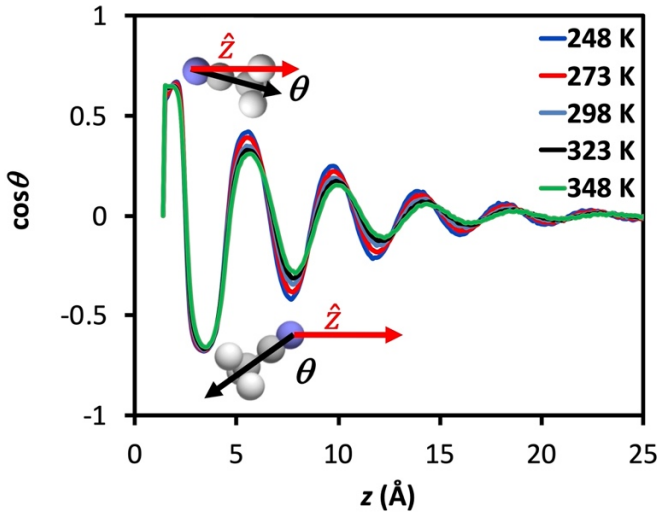


**Figure 6.9** Average orientation of ACN for each temperature as a function of the center-of-mass distance from the surface normal $\hat{\boldsymbol{z}}$. A $\cos\theta$ value of 0 indicates that the cyano groups tend to point toward the silica.

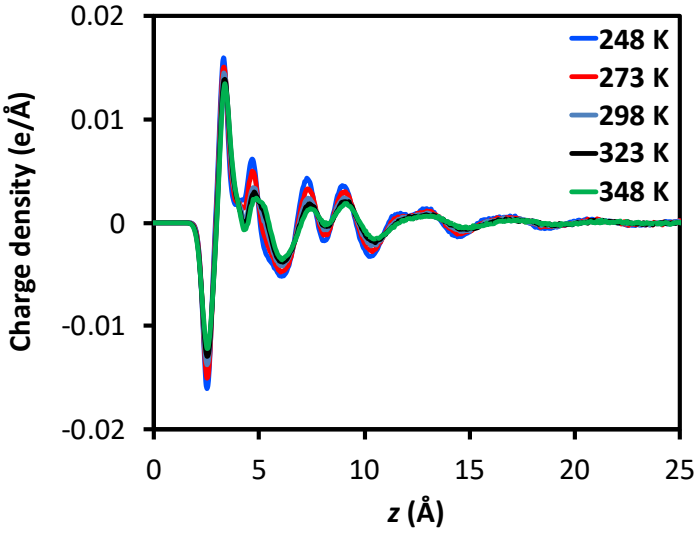


**Figure 6.10** Charge density of ACN for each temperature as a function of the distance from the interface.

### 6.3.2. Transport Properties

We also used nonequilibrium molecular dynamics (NEMD) to investigate transport phenomena in ACN confined in a slit-pore (Figure 6.1(D)). In NEMD of confined liquids, the collective dynamics are simulated by the Poiseuille

hydrodynamics flow due to an external force $f$.[18,19] The force mimics a chemical potential gradient, and the system responds to this perturbation with the resulting flux reaching a steady-state. In our simulations, we added a force in the *x* direction parallel to the surface. Figure 6.11 gives the velocity in the flow direction as a function of the chemical potential gradient. Note that the last three data points correspond to external forces ($f$ > 1.0 pN) that deviate from the linear regime because the thermal energy is higher in the flow direction. These data are excluded from the rest of the analysis as unphysical. The velocity profile as a function of distance from the center of the pore is given in Figure 6.12. This distinctive parabolic profile is characteristic of Poiseuille flow, with the maximum velocity in the center of the pore. The negative slip length beyond ~2 nm fits well to the Poiseuille profile. In a slit geometry, the Poiseuille flow is

$$v_x(x) = \frac{\Delta P D_P^2}{8L\eta}\left[1 - \left(\frac{2x}{D_P}\right)^2\right], \tag{6.4}$$

where $D_P$ is the pore diameter, $L$ is the length, $P$ is the pressure, and $\eta$ is the viscosity of the liquid. Eq. (6.4) was used to fit the parabolic flow profiles, and the driving force $f$ can be converted into a pressure gradient via the Gibbs-Duhem relation, i.e., $\frac{\Delta P}{L} = f\rho$. From Eq. (6.4), we extracted a viscosity value of 0.307 centipoise, in good agreement with experimental values (see Table 6.1). We can also extract information from the Poiseuille flow about the ACN bilayer. From the density profile in Figure 6.10, the first bilayer is ~ 2.0-2.8 Å, where the velocity is small due to the strong wall/fluid interactions.

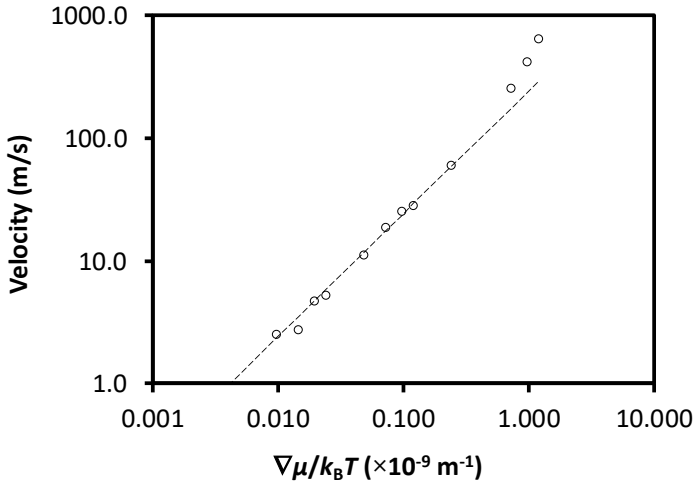


**Figure 6.11** Velocity for ACN in the flow direction as a function of the chemical potential gradient for the NEMD simulations.

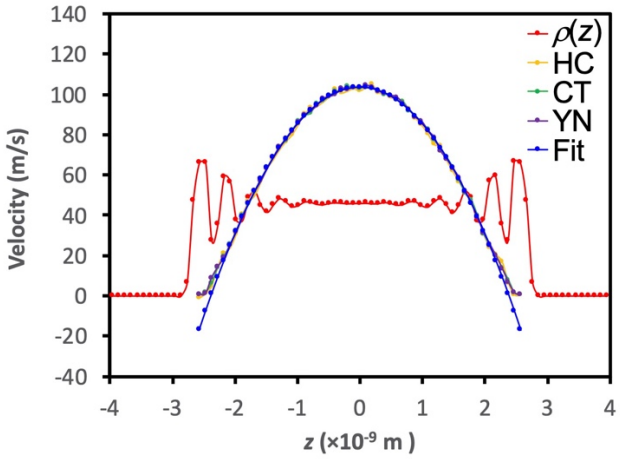


**Figure 6.12** Velocity for ACN confined in a slit-pore geometry. The *x*-component of the velocities with respect to different atomic sites are given, along with the density with respect to HC for comparison.

To explore the impact of flow on local orientation, we calculated the azimuthal angle $\phi$ of the in-plane projection of the molecules. The resulting histograms are shown in Figure 6.13, corresponding to flow from 180˚ to 0˚. The marked threefold symmetry of the polar histograms is due to the underlying symmetry of the silica substrate. To remove this effect, we normalized these data to the case where there is no flow ($f = 0.0$ pN). As the flow increases, the molecules tend to align more strongly along the flow

direction. For both external forces ($f$ = 0.5 and 1.0 pN), the alignment of the ACN molecules in the direction of flow is greater in the second sublayer than in the first, though there is some alignment in both sublayers (Table 6.2). Also, as expected, the alignment is greater with increasing external force. Preliminary analysis of the orientational profiles as a function of flow (not shown) also shows the effects of the external force, though the effects are subtle. The average value of the angle $\theta$, as defined in Figure 6.9, does not change significantly, which indicates that the azimuthal projections of the molecules point in the direction of flow, although their magnitude does not change.

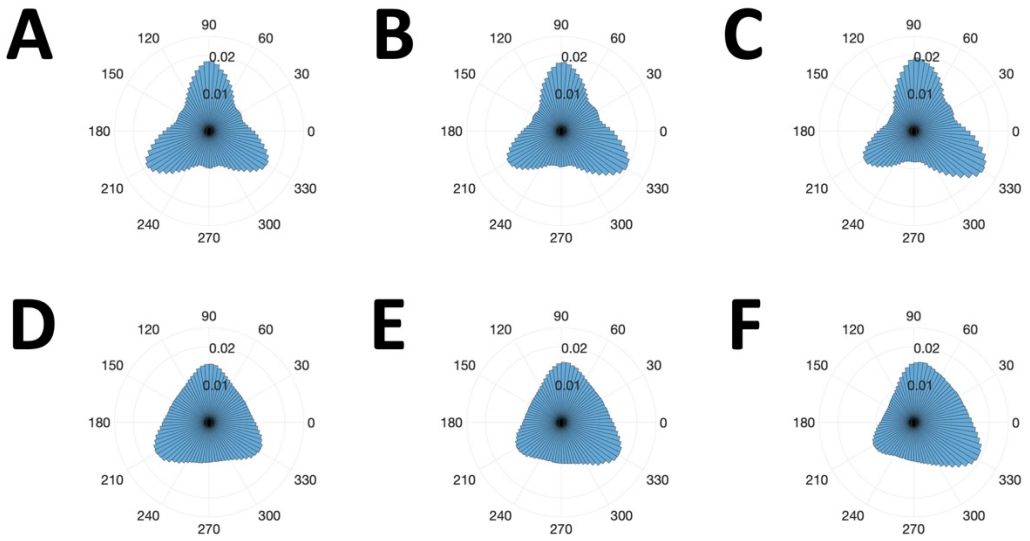


**Figure 6.13** Polar histograms of the angle $\boldsymbol{\phi}$, as defined in the text, for the first sublayer with (A) $f$ = 0.0 pN, (B) $f$ = 0.5 pN, and (C) f $f$ = 1.0 pN. The polar histograms for the second sublayer are given for (D) $f$ = 0.0 pN, (E) $f$ = 0.5 pN, and (F) $f$ = 1.0 pN.

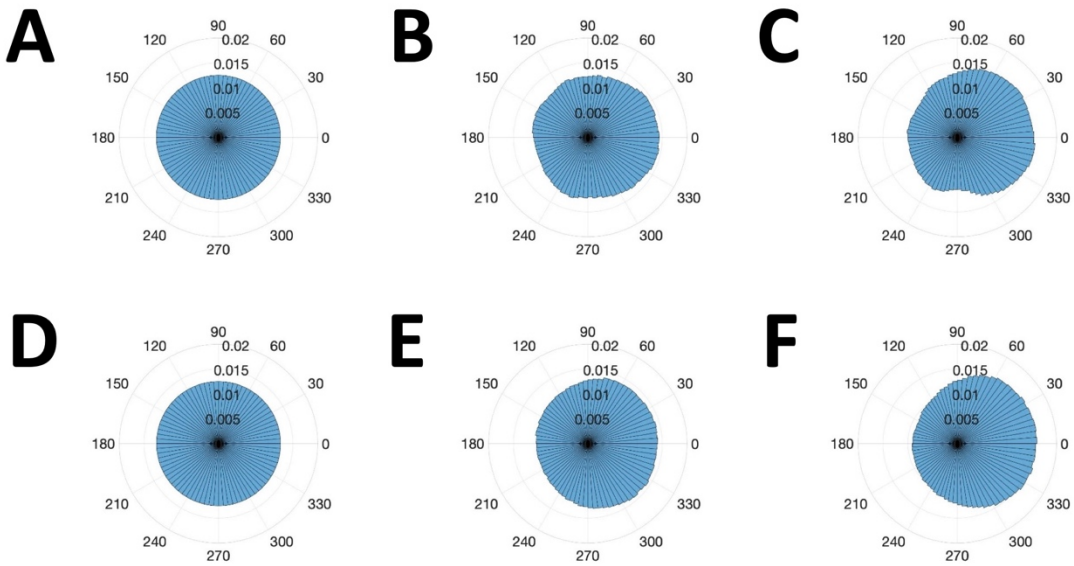


**Figure 6.14** The same polar histograms as in Figure 6.11, except normalized to the $f = 0.0$ pN results.

**Table 6.10** Alignment in the direction of flow for ACN molecules in each sublayer, normalized to the orientation of the molecules in the absence of any external force.

| External force (pN) | Sublayer | P(0˚)/P(180˚) |
|---|---|---|
| 0.5 | 1 | 1.3 |
| 0.5 | 2 | 1.5 |
| 1.0 | 1 | 1.4 |
| 1.0 | 2 | 1.8 |

## 6.4 *Conclusions*

We have presented our preliminary results on the effects of temperature and hydrodynamic flow on perturbing the bilayer that forms in acetonitrile at liquid/silica interfaces. Our structural results reveal the remarkable stability of the bilayer with temperature, suggesting temperature can be used as a variable for ion-selective separations involving acetonitrile as a solvent. For ion-current experiments that rely on

flow, our hydrodynamics results will be useful to determine where the flow boundary may lie. Future work will examine the effect of ions on Poiseuille flow and registry effects on flow with decreasing pore size. The surface that we used here was flat, and the interfacial organization of ACN in confinement in single-digit nanopores is expected to exhibit resonances at certain pore diameters, raising questions about ion mobility in such systems.

## 6.5 *References*


1. Berne, B. J.; Fourkas, J. T.; Walker, R. A.; Weeks, J. D. Nitriles at Silica Interfaces Resemble Supported Lipid Bilayers. *Acc. Chem. Res.* **2016**, *49*, 1605–1613.
2. Souna, A. J. *The Liquid Acetonitrile/Silica Interface: A Model System for Reinterpreting the Vibrational Sum-Frequency Generation (VSFG) Spectra of Liquid/Solid Interfaces.* Ph.D. Thesis, University of Maryland, 2018.
3. Nikitin, A. M.; Lyubartsev, A. P. New Six-Site Acetonitrile Model for Simulations of Liquid Acetonitrile and Its Aqueous Mixtures. *J. Comput. Chem.* **2007**, *28*, 2020−2026.
4. Lee, S. H.; Rossky, P. J. A Comparison of the Structure and Dynamics of Liquid Water at Hydrophobic and Hydrophilic Surfaces – a Molecular Dynamics Simulation Study. *J. Chem. Phys.* **1994**, *100*, 3334–3345.
5. Hu, Z.; Weeks, J. D. Acetonitrile at Silica Surfaces and at Its Liquid-Vapor Interface: Structural Correlations and Collective Dynamics. *J. Phys. Chem. C* **2010**, *114*, 10202–10211.

6. Motevaselian, M. H.; Aluru, N. R. Unpublished.
7. Plimpton, S. Fast Parallel Algorithms for Short-Range Molecular Dynamics. *J. Comput. Phys.* **1995**, *117*, 1−19.
8. Martínez, L.; Andrade, R.; Birgin, E. G.; Martínez, J. M. PACKMOL: A Package for Building Initial Configurations for Molecular Dynamics Simulations. *J. Comput. Chem.* **2009**, *30*, 2157−2164.
9. Frenkel, D.; Smit, B. *Understanding Molecular Simulation: From Algorithms to Applications*, 2nd ed.; Academic Press: London, 2002.
10. Jin, D.; Coasne, B. Molecular Simulation of the Phase Diagram of Methyl Hydrate: Free Energy Calculations, Direct Coexistence Method, and Hyperparallel Tempering. Langmuir **2017**, *33*, 11217−11230.
11. Putnam, W. E.; McEachern, D. M., Jr.; Kilpatrick, J. E. Entropy and Related Thermodynamic Properties of Acetonitrile (Methyl Cyanide). ***J. Chem. Phys.*** **1965**, *42*, 749−755.
12. Cui, S. T.; Cummings, P. T.; Cochran, H. D. The Calculation of the Viscosity from the Autocorrelation Function using Molecular and Atomic Stress Tensors. *Mol. Phys.* **1996**, *88*, 1657−1664.
13. Kinart, C. M.; Kinart, W. J.; Kolasinski, A.; Cwiklinska, A. Physicochemical Properties of Acetonitrile-butan-1-ol and Acetonitrile-butan-2-ol Mixtures. *Phys. Chem. Liq.* **2000**, *38*, 583−597.
14. Dojčansky, J.; Heinrich, J. Saturated Vapor Pressure of Acetonitrile. *Chem. Zvesti* **1974**, *28*, 157−159.

15. Francesconi, A. Z.; Franck, E. U.; Lentz, H. Die *PVT*-Daten des Acetonitrils bis 450 ˚C und 2500 bar. *Ber. Bunsenges. Phys. Chem.* **1975**, *79*, 897−901.
16. Putnam, W. E.; McEachern, D. M., Jr.; Kilpatrick, J. E. Entropy and Related Thermodynamic Properties of Acetonitrile (Methyl Cyanide). ***J. Chem. Phys.*** **1965**, *42*, 749−755.
17. Wohlfarth, C. *Viscosity of Pure Organic Liquids and Binary Liquid Mixtures*; Springer-Verlag Berlin, 2017.
18. Siboulet, B.; Coasne, B.; Dufreche, J. F.; Turq, P. Hydrophobic Transition in Porous Amorphous Silica. *J. Phys. Chem. B* **2011**, *115*, 7881−7886.
19. Arya, G.; Chang, H-C.; Maginn, E. J. A Critical Comparison of Equilibrium, Non-Equilibrium and Boundary-Driven Molecular Dynamics Techniques for Studying Transport in Microporous Materials. *J. Chem. Phys.* **2001**, *115*, 8112−8124.

# Chapter 7: Conclusions

## 7.1 *Conclusions and Future Work*

### 7.1.1. Small-Molecule Liquids

Knowledge of the structure and dynamics of small-molecule liquids is essential in countless applications. Molecular simulations give time-dependent, atomic-level insight into these phenomena, but these simulations are based on models of varying complexity and applicability. I demonstrate in this thesis how resolving both angular and radial information simultaneously via molecular simulation can reveal sensitive details about liquid structure that cannot be accessed experimentally. We cannot glean from our data whether our model faithfully reproduces the true local structure of the liquid, as liquid structure is mathematically ill-defined. However, the ability of the model used here to reproduce the angularly resolved radial distribution function obtained using the reverse Monte Carlo method[1] is promising, as is the ability of the model to reproduce structural motifs seen in clusters[2] and crystals.[3] A new generation of X-ray scattering techniques[4-6] may be able to be used to provide more stringent tests of force fields. In ongoing and future work, applying the two-dimensional angularly resolved radial distribution functions used in this thesis to liquid water may also prove insightful. In models of liquid water, it has been recognized[7,8] that characterizing the structure of the bulk liquid requires the use of multiple order parameters, multidimensional orientational pair correlation functions, and more complex triplet pair correlation functions. Although the dominant structural motif in water consists of

tetrahedral arrangements of neighboring water molecules, it may be fruitful to extend the method of angularly resolved radial distribution functions, which relies on pairwise information, to study, for instance, the hydrogen-bond angle distribution in water.[9] Extending these results to different force fields might prove insightful.

Understanding molecular organization, intermolecular interactions, and dynamics at liquid/solid interfaces also has great practical importance for emerging technologies. Molecular simulations have allowed us to learn surprising new details about the bilayer that forms in acetonitrile at the liquid/silica interface. I demonstrate in this thesis how molecular simulations can be used to probe changes in the organization and transport properties of the bilayer. This information is not easily accessible via experiment. In future work, I will study registry effects in confined acetonitrile. It would also be interesting to explore the effects of ion mobility on the transport properties of confined acetonitrile. These simulations would be of direct relevance to ion current experiments and recent research that shows that the distribution of ions at the bilayer is governed by the interfacial organization of acetonitrile.[10] Another interesting direction for future research would be to study the interfacial behavior of propylene carbonate, which has a gas-phase dipole moment of 4.98 D.[11] There is evidence for the formation of a bilayer structure in nitriles with larger alkyl groups than acetonitrile, such as propionitrile (ethyl cyanide).[12,13] There is also some preliminary evidence (Aluru group) for the formation of a bilayer structure in propylene carbonate. It would be interesting to extend the methodology that we developed in this thesis to study propylene carbonate, as well as to derive orientational time correlation

functions for future vibrational sum-frequency generation spectroscopy studies that could be done analogous to previous work on acetonitrile.[14]

In parallel with the work presented in this thesis, I have also performed extensive molecular simulations of acetonitrile at amorphous silica interfaces and confined in cylindrical silica nanopores. These simulations used the same force fields for acetonitrile and silica that I described in this thesis. My results showed a surprising lack of a bilayer structure in these ostensibly more realistic systems, which suggests that optimizing substrate geometry and the liquid/solid interaction between the force fields are not trivial tasks. In future work, it would be interesting to investigate these effects more systematically, which could prove useful in reproducing the vast experimental evidence for the bilayer structure and studying it systematically *in silico*.

### 7.1.2. Nonlinear Optical Spectroscopy

The data analysis protocol presented in this thesis has been used to model a new spectroscopic method, 2-beam action spectroscopy, enabling for the simultaneous determination of the effects of two orders of absorption. These results are important to characterize processes involving nonlinear absorption, including multiphoton absorption polymerization of nanostructures.[15] In future work, it would be desirable to develop a theory to disentangle the effects of noncumulative observables that complicate experimental efforts, and, ultimately, disentangle the simultaneous effects of three orders of absorption.

## 7.2 *References*


1. Pothoczki, S.; Pusztai, L. Intermolecular Orientations in Liquid Acetonitrile: New Insights Based on Diffraction Measurements and All-Atom Simulations. *J. Mol. Liq.* **2017**, *225*, 160−166.
2. Behrens, M.; Fröchtenicht, R.; Hartmann, M.; Siebers, J.-G.; Buck, U.; Hagemeister, F. C. Vibrational Spectroscopy of Methanol and Acetonitrile Clusters in Cold Helium Droplets. *J. Chem. Phys.* **1999**, *111*, 2436−2443.
3. Enjalbert, R.; Galy, J. $CH_3CN$: X-ray Structural Investigation of a Unique Single Crystal. $\beta \rightarrow \alpha$ Phase Transition and Crystal Structure. *Acta Crystallogr. B* **2002**, *58*, 1005−1010.
4. Sellberg, J. A.; Huang, C.; McQueen, T. A.; Loh, N. D.; Laksmono, H.; Schlesinger, D.; Sierra, R. G.; Nordlund, D.; Hampton, C. Y.; Starodub, D.; DePonte, D. P.; Beye, M.; Chen, C.; Martin, A. V.; Barty, A.; Wikfeldt, K. T.; Weiss, T. M.; Caronna, C.; Feldkamp, J.; Skinner, L. B.; Seibert, M. M.; Messerschmidt, M.; Williams, G. J.; Boutet, S.; Pettersson, L. G. M.; Bogan, M. J.; Nilsson, A. Ultrafast X-ray Probing of Water Structure Below the Homogeneous Ice Nucleation Temperature. *Nature* **2014**, *510*, 381−384.
5. Nilsson, A.; Schreck, S.; Perakis, F.; Pettersson, L. G. M. Probing Water with X-ray Lasers. *Adv. Phys. X* **2016**, *1*, 226−245.
6. Smith, J. W.; Saykally, R. J. Soft X-ray Absorption Spectroscopy of Liquids and Solutions. *Chem. Rev.* **2017**, *117*, 13909−13934.
7. Duboué-Dijon, E.; Laage, D. Characterization of the Local Structure in Liquid Water by Various Order Parameters. *J. Phys. Chem. B* **2015**, *119*, 8406−8418.

8. Soper, A. K. The Structure of Water and Aqueous Systems. *Exp. Methods Phys. Sci.* **2017**, *49*, 135−211.
9. Sharp, K. A.; Vanderkooi, J. M. Water in the Half Shell: Structure of Water, Focusing on Angular Structure and Solvation. *Acc. Chem. Res.* **2010**, *43*, 231−239.
10. Souna, A. J. *The Liquid Acetonitrile/Silica Interface: A Model System for Reinterpreting the Vibrational Sum-Frequency Generation (VSFG) Spectra of Liquid/Solid Interfaces.* Ph.D. Thesis, University of Maryland, 2018.
11. Jedrzejowska, A.; Wojnarowska, Z.; Adrjanowicz, K.; Ngai, K. L.; Paulch, M. Toward a Better Understanding of Dielectric Responses of van der Waals Liquids: The Role of Chemical Structures. *J. Chem. Phys.* **2017**, *146*, 094512.
12. Liu, S.; Hu, Z.; Weeks, J. D.; Fourkas, J. T. Structure of Liquid Propionitrile at Interfaces. 1. Molecular Dynamics Simulations. *J. Phys. Chem. C* **2012**, *116*, 4012−4018.
13. Ding, F.; Zhong, Q.; Manfred, K.; He, X.; Bender, J. S.; Brindza, M. R.; Walker, R. A.; Fourkas, J. T. Structure of Liquid Propionitrile at Interfaces. 2. Experiment. *J. Phys. Chem. C* **2012**, *116*, 4019−4025.
14. Liu, S.; Fourkas, J. T. Orientational Time Correlation Functions for Vibrational Sum-Frequency Generation. 1. Acetonitrile. *J. Phys. Chem. A* **2013**, *117*, 5853−5864.
15. Tomova, Z.; Liaros, N.; Gutierrez Razo, S. A.; Wolf, S. M.; Fourkas, J. T. In situ Measurement of the Effective Nonlinear Absorption Order in Multiphoton Photoresists. *Laser Photon. Rev.* **2016**, *10*, 849−854.

# Appendix A: LAMMPS Input File for Simulations of Acetonitrile at Silica Interfaces in a Slab Geometry

This input file was written for LAMMPS to do the simulations of acetonitrile at the liquid/silica interface as described in Chapter 6.

```
variable temperature equal 298.00 # in K

variable HCtype  equal  1
variable CTtype  equal  2
variable YCtype  equal  3
variable YNtype  equal  4
variable Hstype equal 5 #H
variable Ostype equal 6 #silanol O
variable Otype equal 7 #O
variable Sistype equal 8 #silanol Si
variable Sitype equal 9 #Si
variable Ctype equal 10 #hydrophobic wall

# LJ parameters are from Rossky's 1994 JCP paper
# Note the unit conversion from kJ/mol to kcal/mol

variable HCeps  equal 0.01570 # in kcal/mol
variable HCsig  equal 2.649532788 # in Angstroms
variable CTeps  equal 0.10940
variable CTsig  equal 3.399669508
variable YCeps  equal 0.13410
variable YCsig  equal 3.545776898
variable YNeps  equal 0.13310
variable YNsig  equal 3.011237667
variable Hseps equal 0.0
variable Hssig equal 0.0
variable Oseps equal 0.15504
variable Ossig equal 3.15400
variable Oeps equal 0.15504
variable Osig equal 3.15400
```

```
variable Siseps equal 0.12753
variable Sissig equal 3.79500
variable Sieps equal 0.12753
variable Sisig equal 3.79500
variable Ceps equal 0.066
variable Csig equal 2.53355

variable timestep equal 1.0000 # in fs
variable dumptime equal 1000 # output quantities every 1000 time steps
variable thermotime equal 1000  # output thermo quantities every 1000 time steps

processors      * * *

units          real

boundary       p p f # fixed boundaries along z

atom_style     full
bond_style     harmonic
angle_style    harmonic
special_bonds   lj 0 0 0.5 coul 0 0 0.83

pair_style hybrid lj/cut/coul/long 14.0 lj/cut 14.0
pair_modify pair lj/cut shift yes # for the repulsive wall
kspace_style pppm 1.0e-5
kspace_modify slab 3.0

read_data data_ACN_silica.txt
neighbor       2.0 bin

pair_coeff ${HCtype}   ${HCtype}   lj/cut/coul/long   ${HCeps}  ${HCsig}
pair_coeff ${CTtype}   ${CTtype}   lj/cut/coul/long   ${CTeps}  ${CTsig}
pair_coeff ${YCtype}   ${YCtype}   lj/cut/coul/long   ${YCeps}  ${YCsig}
pair_coeff ${YNtype}   ${YNtype}   lj/cut/coul/long   ${YNeps}  ${YNsig}
pair_coeff ${Hstype}   ${Hstype}   lj/cut/coul/long   ${Hseps}  ${Hssig}
pair_coeff ${Ostype}   ${Ostype}   lj/cut/coul/long   ${Oseps}  ${Ossig}
pair_coeff ${Otype}    ${Otype}    lj/cut/coul/long   ${Oeps}   ${Osig}
pair_coeff ${Sistype}  ${Sistype}  lj/cut/coul/long   ${Siseps} ${Sissig}
pair_coeff ${Sitype}   ${Sitype}   lj/cut/coul/long   ${Sieps}  ${Sisig}

pair_coeff * ${Ctype} lj/cut ${Ceps} ${Csig} 2.8438137 # Rmin = 2**(1/6)*Csig

pair_modify     mix arithmetic

bond_coeff  1  100  1.00   # Si(O-H) bond, constant is a random number
angle_coeff 1  100  109.27 # Si-O-H angle
```

```
bond_coeff  2  340  1.09  # H-C   bond
bond_coeff  3  400  1.458 # C-C   bond
bond_coeff  4  600  1.157 # C-N   bond
angle_coeff 2  35  109.5 # H-C-H angle
angle_coeff 3  35  110 # H-C-C angle
angle_coeff 4  80  180 # C-C-N angle

group  sio2  type ${Ostype} ${Otype} ${Sistype} ${Sitype} ${Ctype}
group  fluid  type ${Hstype} ${HCtype} ${CTtype} ${YCtype} ${YNtype}

neigh_modify delay 0 every 1 check yes

timestep ${timestep}

fix         3 fluid nvt temp ${temperature} ${temperature} 30.0 # Tdamp = 30.0 fs
fix         2 sio2   setforce 0.0 0.0 0.0
fix 1  all shake 0.0001 20 0 b 1

##velocity        fluid create ${temperature} 525232

compute temp_pres all temp
compute Pres all pressure temp_pres

dump            dmp all custom ${dumptime} dump.lammpstrj id type x y z vx vy vz
dump_modify     dmp flush yes sort id format "%d %d %.6f %.6f %.6f %.6f %.6f
%.6f"

thermo          ${thermotime}
thermo_style custom step temp epair emol ecoul evdwl c_Pres c_Pres[1] c_Pres[2]
c_Pres[3] c_Pres[4] c_Pres[5] c_Pres[6]
thermo_modify           flush yes

##minimize 1.0e-6 1.0e-8 1000 100000 # energy minimization
run 40000000 # run simulation for 40 ns
write_data data.end.txt
```

# Appendix B: LAMMPS Input File for Simulations of Acetonitrile at Silica Interfaces in a Slit-Pore Geometry

This input file was written for LAMMPS to do the nonequilibrium molecular dynamics simulations of acetonitrile confined between two silica walls as described in Chapter 6.

```
variable temperature equal 298.00 # in K
variable        F               index  1.0 # pN


variable HCtype  equal  1
variable CTtype  equal  2
variable YCtype  equal  3
variable YNtype  equal  4
variable Hstype equal 5 #H
variable Ostype equal 6 #silanol O
variable Otype equal 7 #O
variable Sistype equal 8 #silanol Si
variable Sitype equal 9 #Si

# LJ parameters are from Rossky's 1994 JCP paper
# Note the unit conversion from kJ/mol to kcal/mol

variable HCeps  equal 0.01570 # in kcal/mol
variable HCsig  equal 2.649532788 # in Angstroms
variable CTeps  equal 0.10940
variable CTsig  equal 3.399669508
variable YCeps  equal 0.13410
variable YCsig  equal 3.545776898
variable YNeps  equal 0.13310
variable YNsig  equal 3.011237667
variable Hseps equal 0.0
variable Hssig equal 0.0
variable Oseps equal 0.15504
```

```
variable Ossig equal 3.15400
variable Oeps equal 0.15504
variable Osig equal 3.15400
variable Siseps equal 0.12753
variable Sissig equal 3.79500
variable Sieps equal 0.12753
variable Sisig equal 3.79500
##variable Ceps equal 0.066
##variable Csig equal 2.53355

variable timestep equal 1.0000 # in fs
variable dumptime equal 50 # output quantities every 1000 time steps
variable thermotime equal 100  # output thermo quantities every 1000 time steps

processors       * * *

units          real

boundary       p p p

atom_style      full
bond_style      harmonic
angle_style     harmonic
special_bonds   lj 0 0 0.5 coul 0 0 0.83

pair_style      lj/cut/coul/long 14.0 14.0
kspace_style    ewald 1.0e-5

read_data data_ACN_silica.txt
neighbor        2.0 bin

pair_coeff ${HCtype}   ${HCtype}   ${HCeps}  ${HCsig}
pair_coeff ${CTtype}   ${CTtype}   ${CTeps}  ${CTsig}
pair_coeff ${YCtype}   ${YCtype}   ${YCeps}  ${YCsig}
pair_coeff ${YNtype}   ${YNtype}   ${YNeps}  ${YNsig}
pair_coeff ${Hstype}   ${Hstype}   ${Hseps}  ${Hssig}
pair_coeff ${Ostype}   ${Ostype}   ${Oseps}  ${Ossig}
pair_coeff ${Otype}    ${Otype}    ${Oeps}   ${Osig}
pair_coeff ${Sistype}  ${Sistype}  ${Siseps} ${Sissig}
pair_coeff ${Sitype}   ${Sitype}   ${Sieps}  ${Sisig}

pair_modify     mix arithmetic

bond_coeff  1  100  1.00   # Si(O-H) bond, constant is a random number
angle_coeff 1  100  109.27 # Si-O-H angle
```

```
bond_coeff  2  340  1.09  # H-C   bond
bond_coeff  3  400  1.458 # C-C   bond
bond_coeff  4  600  1.157 # C-N   bond
angle_coeff 2  35  109.5 # H-C-H angle
angle_coeff 3  35  110 # H-C-C angle
angle_coeff 4  80  180 # C-C-N angle

group  sio2  type ${Ostype} ${Otype} ${Sistype} ${Sitype}
group  fluid  type ${Hstype} ${HCtype} ${CTtype} ${YCtype} ${YNtype}
group  fluid_YC type ${YCtype}
compute acntemp fluid temp/partial 0 1 1

neigh_modify delay 0 every 1 check yes
timestep ${timestep}

## comment out fixes 1 and 3 if doing an energy minimization
fix         2 sio2   setforce 0.0 0.0 0.0
fix 1  all shake 0.0001 20 0 b 1
fix         3 fluid nvt temp ${temperature} ${temperature} 30.0 # Tdamp = 30.0 fs
fix_modify      3 temp acntemp
# Apply the driving force
variable forcefac equal 0.01439 # pN in kcal/mol/A
variable extforce equal $(v_F*v_forcefac)
fix pressure fluid_YC addforce ${extforce} 0 0


dump            dmp all custom ${dumptime} dump.lammpstrj id type x y z vx vy vz
dump_modify     dmp flush yes sort id format "%d %d %.6f %.6f %.6f %.6f %.6f
%.6f"

thermo          ${thermotime}
thermo_style custom step temp epair emol ecoul evdwl
thermo_modify           flush yes

##minimize 1.0e-6 1.0e-8 1000 100000 # energy minimization
run 3000000 # run simulation for 3 ns
write_data data.end.txt
```

# Bibliography


1. Bender, J. S.; Cohen, S. R.; He, X.; Fourkas, J. T.; Coasne, B. Toward in Situ Measurement of the Density of Liquid Benzene Using Optical Kerr Effect Spectroscopy. *J. Phys. Chem. B* **2016**, *120*, 9103−9114.
2. Liaros, N.; Cohen, S. R.; Fourkas, J. T. Determination of the Contributions of Two Simultaneous Absorption Orders Using 2-Beam Action Spectroscopy. Opt. Express 2018, 26, 9492−9501.
3. Cohen, S. R.; Fourkas, J. T. Extracting Information on Linear and Nonlinear Absorption from Two-Beam Action Spectroscopy Data. *J. Phys. Chem. A* **2019**, *123*, 7314−7322.